FLOW OR BLOW?

UNDERSTANDING MAGMA FLOW IN CONDUITS DURING VESICULATION

by

S. JACKSON OAKEY

(Under the Direction of Mattia Pistone)

ABSTRACT

The ability of silicic magma to erupt explosively depends on the retention of exsolved volatiles in the magma prior to eruption. If volatiles escape before an eruption, effusive lava flows are likely to occur; if gas is retained in magma and helps increase its internal pressurization, then magma might be fated to erupt explosively. Lipari Island, off the northern coast of Sicily, has been characterized by explosive-effusive events occurring in the same eruptive cycle, such as the explosive phase of Monte Pilato followed by the effusive lava flow of Rocche Rosse ~450 years later. Using glassy obsidian and spherulite-bearing obsidian samples collected from the deposits of the Rocche Rosse unit, this study tested the influence of minor changes in H_2O concentration in the style of vesiculation and flow of material in conduits at temperatures relevant to magmatic conditions. This study presents a nano- and micro-scale analysis of the experimental products undergoing vesiculation at 950-1150 °C and atmospheric pressure, along with thermodynamic estimations of crystallization and associated potential chemical changes contributing to differing volcanic textures in these high-viscosity systems at equivalent temperatures. Results show vesiculation primarily occurred at the microscale, and plug flow dominated ascent in conduits.

INDEX WORDS: Lipari Island, Magma, Rheology, Degassing, Outgassing, Obsidian, Volcanology

FLOW OR BLOW?

UNDERSTANDING MAGMA FLOW IN CONDUITS DURING VESICULATION

by

S. JACKSON OAKEY

B.S., Middle Tennessee State University, 2021

A Thesis Submitted to the Graduate Faculty of The University of Georgia in Partial Fulfillment of the Requirements for the Degree

MASTER OF SCIENCE

ATHENS, GEORGIA

2024

FLOW OR BLOW?

UNDERSTANDING MAGMA FLOW IN CONDUITS DURING VESICULATION

by

S. JACKSON OAKEY

Major Professor:	Mattia Pistone
Committee:	Charlotte Garing
	Alan Whittington

Electronic Version Approved:

Ron Walcott
Vice Provost for Graduate Education and Dean of the Graduate School
The University of Georgia
December 2024

ACKNOWLEDGEMENTS

Retrospect is a funny thing when you acknowledge it before it happens. Not long ago, I remember thinking, “I don’t know how I’m going to do this, and when it’s done, I won’t know how I did it.” Well, it’s done now, and while I don’t have the slightest clue how I did it. I do know I wouldn’t have been able to reach the finish line without the help of a long list of people.

Mattia Pistone, Charlotte Garing, and Alan Whittington have all done a wonderful job guiding me. Thank you for letting me learn from you and being patient with me. Special thanks are deserved to Alan Whittington for letting me travel and work with him in his lab so I could complete almost all my experiments.

Thank you to Sigma Xi, GSA, and the UGA Department of Geology for providing funding for this project. Thank you to my lab mates Carly Daniel and Kaitlyn Hulsey. You guys drive me crazy most of the time, but being crazy is more fun anyway. Thank you to the rest of the graduate students at UGA. I wouldn’t forgive myself if I didn’t thank Rob Hawman for being the most genuine person around and always supporting students. Thank you to my 8th-grade science teacher, Bryan Schultz. I genuinely don’t believe I would have ended up here without you. Thank you to Warner Cribb for being a constant positive influence during undergrad and encouraging me to push myself.

I would also like to thank people I have met in Georgia outside of the academic setting. Thank you to all the Muay Thai folks at Megalodon Gym and my classical guitar teacher, James Terell. The greatest thanks I can give goes to my mother. Who found a way to give me everything even though she was given so little.

TABLE OF CONTENTS

Page

LIST OF TABLES

Page

LIST OF FIGURES

Page

CHAPTER 1

INTRODUCTION

Volcanoes help build our planet, enrich cultural heritages, provide valuable ores for mining, generate fertile soil for crops, and add new land, constructing continental landmasses above sea level. However, volcanoes also act as hazardous systems with high-risk for populations cohabitating within the range of their eruptive activity. An estimated ~1.1 billion people live within 100 km of a volcano, with an estimated 278,368 fatalities between 1500 BCE and 2017 CE (Brown et al., 2017). Recognizing the signs of an eruption at the surface before one occurs is critical to ensuring the safety of local populations. One of the issues with predicting volcanic hazards is knowing what style of eruption (i.e., explosive or effusive) will occur. Explosive eruptions pose a more significant threat than their effusive counterparts. Regional variation among volcanoes creates unique geographical hazards. Volcanic islands capable of explosive eruptions present their own issues as residents may have to evacuate via boat, for example. Income from tourism would also be lost as the island would be considered unsafe. Roads, buildings, and ports would have to be rebuilt or repaired before residential life and tourism could return to normal, creating spending without generating income. Knowing when a volcano, capable of both eruption styles, will erupt explosively, effusively, or through a hybrid activity during the same eruption event is one of the major challenges present-day volcanology faces. Even though volcanoes near many population centers are readily monitored, it is challenging to decipher subsurface processes that indicate whether an eruption is imminent and what type of eruption may occur.

A large control on eruption style is the subsurface dynamics of magma. Studying transport mechanics and rheology is essential to understand the subsurface dynamics of magma. Viscosity represents the material's internal resistance to flow under stress; it is a crucial physical

property controlling magma transport within the Earth's interior and its eruption at the surface. Magma viscosity is controlled by the modal proportion of minerals, gas bubbles, and silicate melt that capture the liquid, solid, and gas state of matter in a multiphase magma (Petford, 2009; Pistone et al., 2012; 2013). The rheology of a magma largely depends on volatiles and crystals suspended in the liquid melt. The generation of explosive eruptions depends on magma's ability to retain exsolved volatiles, forming gas bubbles during unrest preceding the eruption. Between 0 and 1 wt.%, H_2O concentration causes extreme nonlinear variations in viscosity at relatively low temperatures relevant to silicic systems (Hess and Dingwell, 1996). If viscosity is too low due to higher concentrations of volatiles in the melt, then gas bubbles may not be retained in the melt, inhibiting the generation of explosive eruptions. Upon cooling and/or decompression, silicate melts in magmas can experience crystallization. Such a process is initiated at nanoscale with the formation of nanocrystals or nanolites (i.e., crystals of nanometer size; Sharp et al., 1996) and can favor an increase of viscosity up to two orders of magnitude at crystal volume fractions as low as 0.10, as a consequence of the modification of the melt composition, the degree of melt polymerization, and the onset of strong particle-particle interactions occurring at nanoscale (Di Genova et al., 2020). When minerals grow to sizes relevant to microlites (crystals of microscale size suspended in the melt populating the glass groundmass of volcanic rocks) and phenocrysts (minerals of large size ranging from hundreds of microns to several millimeters contributing to a porphyritic texture in volcanic rocks), magmas become crystal-bearing suspensions in which the modal proportion of minerals dictates the non-linear variation of magma viscosity. Over the last four decades, numerous studies from field, experimental, and computational experiments have been conducted to quantify the rheology of crystal-bearing magmas (e.g., Caricchi et al., 2007; Costa et al., 2009; Frontoni et al., 2022).

To date, very few studies have explored the rheological complexity of multiphase magmas containing simultaneously minerals, gas bubbles, and melt in different modal proportions (e.g., Avard and Whittington, 2012; Vona et al., 2013; 2017; Coats et al., 2018). For instance, in the experimental study led by Pistone et al. (2012; 2013) exploring magma rheology in a wide range of crystallinity (0.24 to 0.65) and limited gas porosity (0.09 to 0.12), the addition of relatively small bubble volume fractions to particle-bearing suspensions significantly decreases magma viscosity. This decrease in magma viscosity ranges from less than one order of magnitude at the crystal volume fraction of 0.24 to four orders of magnitude at the crystallinity of 0.65 (Pistone et al., 2013). This result demonstrates the importance of the interactions between melt, crystals, and gas bubbles playing a pivotal role in controlling magma viscosity and defining non-Newtonian behaviors during magma flow: i) at high crystallinity (0.55–0.65) bubbles favor shear localization, and ii) at low crystallinity (0.24–0.44) deformation leads to outgassing (i.e., escape of exsolved gas in the magma). This duality of magma rheology can significantly affect magma flow dynamics and the consequent transition between explosive and effusive eruption styles at active silicic volcanoes. Another critical factor in the retention of volatile forming gas bubbles is the interaction between magma and the host rock. Permeable pathways are created when host rocks fracture, allowing volatiles to escape the magma (e.g., Benson et al., 2012; Heap et al., 2014; 2015). If magma fractures, then links between the center of the conduit and periphery allow for the migration of exsolved gas into host rock that would otherwise not occur (Cabrera et al., 2015; Eichelberger, 1995; Lavallée et al., 2013). Porosity and permeability of host rocks thus influence the volatile loss from magmas.

Here, the main questions to address are as follows: how can gas bubbles control magma transport while approaching the surface during flow in a volcanic conduit? How does the competition between gas retention and outgassing evolve during magma flow in a conduit? How does the largest variation in viscosity occurring between 0 and 1 wt.% H_2O control the intensity of explosive eruptions? What are the mechanisms controlling the explosive-effusive activity at silicic volcanoes? To answer these questions, it is imperative to conduct novel experiments that can monitor or capture the physical behavior of magma during flow in conduits and quantify the role of vesiculation and magma's ability to retain or expel gas before the imminent eruption. In this study, I consider the well-known case of explosive-effusive volcanism of Lipari Island (Italy) to possibly apply the experimental constraints and contribute to understanding the physics of gas accumulation efficiency in silica-rich magmas before an eruption. Trapped volatiles increase pressure within the magma at depth, increasing eruption intensities. If crystallinity is large (> 70% minerals on the volatile-free basis), then magma tends to act as a rheologically immobile mush that may fracture with increasing gas pressurization and/or never reach the surface (Pistone et al., 2013; 2017). Production of effusive lava flows occurs if volatiles escape the initial magma at low to moderate crystallinity (< 50% minerals) with a melt that does not trap exsolved gas efficiently (Belien et al., 2011). This study aims to distinguish the mechanisms that cause gas retention versus removal in silica-rich magma by simulating magma ascent through host rocks by magma vesiculation. Additionally, this study tests the hypothesis that minimal concentration increases in H_2O between 0 and 1 wt.% may hamper high-intensity explosive eruptions or even inhibit explosive activity. Using obsidians from the Aeolian Island of Lipari, two types of magma analogs are experimentally simulated. Glass obsidian acts as a volatile poor (0.34 wt.%) sample,

and spherulite-bearing obsidian acts as a volatile concentrated (0.46 wt.%) sample under atmospheric conditions. Simulated magma also needs analogous host rocks to best replicate the historical volcanic activity in Lipari Island. For this purpose, Elberton Granite (intact) and Tate Marble (fractured) are used as analogs for country rocks. Granite provides an intact low porosity and permeability host rock where volatiles cannot escape. Marble is structurally weaker than granite when exposed to silicic magma temperatures. At temperatures exceeding 400 °C, marble is prone to fracture due to thermal stress (Guo et al., 2020), creating permeable pathways for volatile loss. Based on the identified xenoliths found in Lipari (Honnorez and Keller, 1968) and xenoliths collected by diving and dredging in the area between Panarea and Lipari (Calanchi et al., 2002), granite and carbonate rocks are likely host materials for Lipari magmas before their eruptions.

The geologic background is provided in Chapter 2. Chapter 3 details the methods used in this study. Chapter 4 shows the results of the experiments. Chapter 5 provides the discussion, and Chapter 6 lists the conclusions and describes future work.

CHAPTER 2

GEOLOGIC BACKGROUND

It is vital to understand the volcanic processes leading to effusive and explosive activity, which is the main target for the experimental work in this study. Another important context is the geologic history of where obsidian samples were collected on Lipari Island.

2.1 Explosive Eruptions

The hazardous potential of volcanic eruptions on a population largely depends on whether an eruption is explosive or effusive. Explosive eruptions (Volcanic Explosivity Index ≥ 2) have the potential to generate ash columns that reach the stratosphere, disrupting air traffic and modifying global climate (Cashman and Scheu, 2015). The greatest immediate threat from explosive eruptions is pyroclastic density currents (PDCs). After generating an ash column, pyroclasts and gas heat the surrounding air. Eventually, the buoyancy of ejected material will no longer be sufficient to sustain the column, which then collapses and triggers the generation of PDCs capable of traveling up to tens of kilometers at speeds between 100 and 600 m/s (Sparks and Wilson, 1976). On the other hand, effusive eruptions are significantly less hazardous in comparison but can be far-reaching and long-lived (Carr et al., 2020), damaging property and emitting toxic gases. Silicic magma eruptions can have explosive and effusive stages associated with a single eruption event. Explosive eruptions are determined by the level of gas accumulation and extent of magma fragmentation. Fragmentation is the breakup of molten rock into individual pieces or fragments (Gonnerman, 2015). Fragmentation can occur by rapid acceleration inducing high rates of magma deformation and decompression-induced degassing, which exerts a high stress and/or strain on the residual silicic melt and favors its potential rupture (Gonnerman,

2015). As the magma ascends and experiences less pressure, volatile saturation is reached in magma, with consequent degassing resulting in bubble growth. The build-up of volatile over-pressure causes magma to ascend from gas expansion, releasing energy into the magma (Parfitt and Wilson, 2008). Such a vesiculation causes a runaway acceleration of magma ascent due to its buoyancy increase (Cashman and Scheu, 2015) along with possible decrease in viscosity (Bagdassarov and Dingwell, 1992). Volatile concentration in melt increases with increasing depth or pressure; as magma ascends, the total reduction in gas phase pressure or decompression during ascent make bubbles nucleate and grow (Sparks, 1978; Parfitt and Wilson, 2008) and favor the internal pressurization of the gas-charged magma (Sparks, 1997). In the case of rapid decompression following removal of a rock plug or lava dome collapse at the top of a volcanic conduit, the release of the internal magma pressurization induced by trapped gas bubbles may be near-instantaneous. Under these conditions, magma responds in a brittle manner, and the associated bubble nucleation and coalescence are of minor importance because of the short timescale (Cashman and Scheu, 2015). Also, magma ascent rate controls whether explosive eruptions are steady or transient. In steady explosive eruptions, gas and magma are supplied to the vent at a sustained rate. Bubbles do not coalesce and remain joined with the magma (Parfitt and Wilson, 2008). Transient eruptions are explosions lasting seconds to minutes. In transient eruptions, magma ascent speed is slow, allowing bubbles to coalesce and rise through the magma, building pressure. Once a plug is encountered, pressure will build until the plug bursts, causing an eruption (Parfitt and Wilson, 2008). Viscosity also plays a crucial role in bubble coalescence. Low melt viscosity allows for efficient movement of bubbles and potential gas coalescence (Heap et al., 2014). Overall, the interplay of coalescence, ascent rate, and viscosity determines the eruption style.

2.2 Effusive Eruptions

In silicic magmas, effusive activity may be likely if exsolved volatiles are readily removed from a magma before its eruption. Felsic magmatic systems are often considered closed systems due to the infrequency of eruptions exposing magma to the atmosphere (Bonechi et al., 2024). However, the system becomes open if gas can escape through country-rock walls (Fink and Anderson, 2000) or through a magma permeable to gas flow (Yoshimura and Nakamura, 2008). Open system degassing controls if an effusive eruption occurs in silicic magmas (Okumura et al., 2010). During degassing, magma shear deformation along conduit walls enhances brittle fractures in the magma, providing pathways for outgassing through country rock. Permeability is also an essential control on outgassing, as the more permeable a magma is, the easier it is for gas to flow. The permeability of silicic magma begins to increase at exsolved gas modal proportion of ~30% (Okumura et al., 2009).

More recently, sintering has been proposed as a prominent influence on the shift from explosive to effusive eruptions (Wadsworth et al., 2020). However, this model is widely debated. In magma sintering, tephra is sintered along conduit walls during explosive eruptions. Over time, the dense sintered material clogs enough of the conduit to shift to an effusive eruption. The advancing lava flow is fed by continued sintering from suppressed fragmentation. Fractures in this model occur in the sintered plug from shearing (Wadsworth et al., 2020). Silicic lavas can create a type of lava dome called coulees or cooled mounds of viscous magma extruded from a volcanic vent (Fink and Anderson, 2000). Typical lava dome collapses result in pyroclastic flows/surges and rockfall avalanches. For example, Unzen volcano on the island of Kyushu, Japan, had five years of dome growth from 1990 to 1995. In 1991, a gravitational dome collapse occurred, creating a pyroclastic flow that resulted in 43 fatalities (Lavallée et al., 2022, and references therein). If a lava dome is dense enough during extrusion (Fink and Anderson, 2000), obsidian flows, such

as Rocche Rosse on Lipari Island, may be generated. Coulees can be up to 400 m thick with total volumes of over 10s km^3 (de Silva et al., 1994). Upper surfaces are domed, usually circular or oval in shape, and have compositions that are dacitic to rhyolitic (Calder et al., 2015). Other examples of obsidian flows formed from coulees include the Big Obsidian Flow in Oregon and Obsidian Dome in California in the USA. Lava dome formation is associated with explosive and effusive eruption sequences. Before the explosive June 15th, 1991, caldera-forming eruption of Mt. Pinatubo, a lava dome extrusion on June 8th, 1991, allowed volcanologists to analyze magma composition. Composition and the information that a conduit was open for a following eruption helped provide accurate warnings, reducing casualties (Fink and Anderson, 2000). In contrast, in May 2008, an explosive eruption occurred at Mt. Chaitén in Chile. This eruption destroyed a pre-existing lava dome, and a week after explosive activity, a new lava dome was formed (Castro and Dingwell, 2008). Because Rhyolitic lava flows are rare, observations of active rhyolitic are extremely limited, and flows did not exist until Chaitén and Cordon Caulle eruptions in 2008 and 2011-2012 (Trafton and Giachetti, 2022). As a result, most observations are limited to already emplaced flows. Some of the most well-studied domes are in California and Oregon. Big Obsidian Flow in Newberry, Oregon, was generated from the final stage of an initially explosive eruption in 640 CE (Trafton and Giachetti, 2022). Little Glass Mountain formed under a similar eruptive sequence but is covered by a layer of pumice with sparse obsidian outcrops (Fink, 1983). Obsidian Dome in the Mono-Inyo Craters formed from a phreatic eruption transitioning into explosive eruptions and ended with the passive effusion of lava (Fink, 1985). Mayor Island in New Zealand also displays an ancient 8 ka rhyolitic lava flow. In contrast to other flows mentioned, in this flow, obsidian is only 1-5 m thick and is primarily constituted of lapilli (Stevenson et al.,

1993). Compared to these lava flows, Rocche Rosse is ideal for studying the retention and release of volatiles in the conduit. Unlike Little Glass Mountain, Obsidian Dome, and Mayor Island, the flow occurred hundreds of years after the initial explosive eruption (Pistolesi et al., 2021), making magma sintering an unlikely explanation compared to outgassing in the conduit. Sintering models have been applied to eruption-style transitions on time scales of days to months. The 640 CE Big Obsidian Flow eruption began as Subplinian with a sustained plume and later shifted to Vulcanian blasts. The final stages of the eruption were restricted to an obsidian flow with potential hybrid activity. No distinction is made in the time between the onset of the Subplinian activity and its final effusion (Trafton and Giachetti, 2022). Observations from the 2011-2012 explosive to effusive eruption at Cordon Caulle, Chile, have a similar deposition sequence to what has been proposed for Big Obsidian Flow. Two months after seismic activity, Plinian activity occurred for two days. The following 7-9 days were characterized by the development of a pyroclastic column oscillating from frequent explosions to effusive activity (Castro et al., 2013). Other benefits of Rocche Rosse include the amount of flow exposed to the surface. Most of the flow is accessible, except for areas of challenging topographies and brush coverage. The Rocche Rosse lava deposit is geologically juvenile, which contributes to clearly appreciating the field textures, which help reconstruct the emplacement dynamics of this obsidian flow.

2.3 Aeolian Archipelago Volcanism

The Aeolian archipelago (Fig. 1) is located ~30 km off the northern coast of Sicily in the southern Tyrrhenian Sea. The other six islands include Alicudi, Filicudi, Panarea, Salina, Stromboli, and Vulcano. All seven islands are volcanic and result from the complex collision between the African and Eurasian plates (Ventura, 2013). Aeolian magmatism is thought to be fueled by

the subduction of a detached slab from the African plate and the thermal uplift caused by the intruding asthenosphere in the lithospheric crust (Esperanca et al., 1992). Aeolian magma compositions are calc-alkaline to K-alkaline. The volcanic centers of the islands produced mafic products up until the last 50 ka. In the central islands, Lipari, Vulcano, and Salina, rhyolitic products are common in the Holocene activity (Davi et al., 2010). Two distinct types of volcanic eruptions are named after Aeolian islands. Strombolian eruptions are named after the Island of Stromboli and are characterized by short-duration explosions with high-velocity curved ballistic trajectories. Eruptions are driven by large gas bubbles bringing up and ejecting magma as the gas bubble bursts (Blackburn et al., 1976; Parfitt and Wilson, 2008). Vulcanian-style eruptions are named after Vulcano and are similar to Strombolian eruptions in that the time scales of the eruptions are often brief, lasting only seconds to minutes. However, Vulcanian eruptions are more violent, ejecting blocks up to tens of meters wide and thick. Ash plumes can be up to 20 km high and are unstable enough to collapse, creating pyroclastic density currents (Parfitt and Wilson, 2008). These two eruptive styles have not been documented in Lipari Island, where lava flows from effusive activity and fallout deposits and pyroclastic flows from high-intensity eruptions (including sub-Plinian to Plinian activity) have been studied.

2.4 Lipari Island Eruptive History

Volcanic activity on Lipari dates to 220 ka and was initially divided into four main periods (Pichler, 1976;1980). These four periods have since been divided into ten cycles (Fig. 2). These cycles start with explosive eruptions and end with effusive activity. Each cycle is divided by geochronological gaps, unconformities, and geochemical composition changes (De Rosa et al., 1985; Crisci et al., 1991). Pichler (1976;1980)'s first period is cycle I, the second period in-

cludes cycles II-VI, the third period consists of cycles VII-IX, and the fourth period is represented by cycle X (Fig. 2). The first period consists of volcanics with submarine origin and andesitic composition beginning between 223 and 188 ka. Deposits include submarine dikes, volcanic breccia, and pillow lavas. Magma sources came from an N-S trending fissure, with most first-period deposits covered by second through fourth-period products. The second period began 60-120 ka. Deposits from this period occurred in the central part of the island and formed the stratovolcanoes of Monte San Angelo and Costa d'Agosto. The second period is divided into three substages, all building the central part of the island. The first substage occurred over ~30 ka with effusive activity focused at Costa d'Agosto and explosive activity at Monte San Angelo. Five layers of paleosols occur during this substage, showing volcanic inactivity over thousands of years at each layer. The second and third substage is limited to Monte San Angelo. Rhyodacitic lava flows dominate the second substage, and explosive rhyodacitic eruptions categorize the third. A period of volcanic inactivity followed the next 20 ka. During inactivity, second-period deposits were reworked by rainwater. In road outcrops by the village of Varesana di Sopra, evidence of lahars is preserved in reworked second-period deposits with third-period pyroclastics covering them (Pichler, 1976;1980). Near the end of the second period, a volcanic-tectonic collapse occurred, and a submarine caldera was formed extending from present-day southern Lipari to northern Vulcano. The third period started ~25 ka and ended ~13 ka. This period constructed the southern part of Lipari and formed Monte Guardia and Giardina. The fourth period occurred after ~3-5 ka of inactivity, beginning ~10 ka. Fourth-period deposits shifted to the northeastern position of present-day Lipari. Third and fourth-period geochemical compositions are alkali feldspar rhyolites (Pichler, 1976;1980). Over the last 1500 years, four eruptions have occurred on Lipari Island: two pyroclastic successions composing Monte Pilato and Lami and the two lava

flow activities of Rocche Rosse and Forgia Vecchia. Radiocarbon (^{14}C) and paleomagnetic dating of the four eruptions place Mt. Pilato between CE 675 and 880, Rocche Rosse between CE 1243 and 1304, Forgia Vecchia between CE 1160 and 1306, and Lami between CE 1253 and 1316 (Fig. 3) (Pistolesi et al., 2021). Monte Pilato and Rocche Rosse eruptions construct the Monte Pilato edifice and are part of the same eruptive sequence. Monte Pilato erupted explosively, producing pumice deposits, and Rocche Rosse erupted effusively, resulting in an obsidian-forming lava flow (Bullock et al., 2018; Pistolesi et al., 2021). The bulk rock chemistry for both eruptions is largely identical, aside from volatile concentrations decreasing from 0.9 to ~0.2 wt.% H_2O (Davì et al., 2010; Shields et al., 2016).

2.5 Elberton Granite

During fieldwork on Lipari, xenoliths of granite, gneiss, and hornfels (Honnorez and Keller, 1968) of a size large enough to be used for the experimental work were not found. Instead, Elberton granite, a fine to medium-grained rock, was selected. Located in Elberton, Georgia, the Elberton pluton was emplaced around 350-320 Ma (Stormer, 1980; Whitney et al., 1980) and is an I- to S-type granite covering an area of approximately 500 km^2. Accessory minerals of titanite (sphene) and green biotite are found in the I-type granite, whereas an oversaturation of silica is typical in the S-type granite of the Elberton batholith (Wenner, 1980). The average mineral modal proportion across both I- and S-type granites in this pluton consists of ~30% quartz, 30-35% oligoclase, 30-35% microcline, and 4-7% biotite, devoid of metamorphic modification and deformation (Stormer, 1980). Elberton granite is ideal for conduit experiments because it contains a similar concentration of silica, alumina, and alkali as Rocche Rosse obsidians (Table 1). With such a similar concentration in the most abundant major elements, a low level of contami-

nation via chemical diffusion between foaming obsidian and granite host during high-temperature experiments is expected. Magmas that fed Monte Pilato and Rocche Rosse eruptions are rhyolitic in composition. Granite provides an excellent experimental country rock analog for the extruded magmas of rhyolitic compositions from Lipari. The highly homogeneous texture and chemistry of Elberton granite also make experiments easily reproducible. Each core cut and drilled from the granite does not contain significant modal mineralogy variations that could affect the outcomes of the heating experiments.

2.6 Tate Marble

Tate Marble is in northeastern Georgia and part of the Murphy Marble Belt. The Marble is coarse-grained and high in calcium (Costello et al., 2002). Accessory amphiboles are also present and are likely from basaltic or andesitic ashfall into the water where the calcareous sedimentary protolith was generated (Higgins, 2002). Marble was selected as the second material to use as a country rock for the high-temperature conduit experiments due to its structural strength, chemical contrasts with Elberton granite, and the abundance of carbonate rocks surrounding magma reservoirs in the Tyrrhenian Sea basement (Calanchi et al., 2002). Marble is weaker than granite, which provides a higher likelihood of developing fractures during heating experiments. Fractures in the jacket walls would provide a pathway for coalesced bubbles to outgas from the magma into the surrounding rock, encouraging the generation of effusive eruptions. If magma interacts with a carbonate-bearing rock, such as a marble or limestone, carbon (in the form of CO_2) and calcium from the country rock can assimilate into magma at contact boundaries (Del Moro et al., 2001), exchanging mass and increasing volatile supply in the magma and encouraging the generation of explosive eruptions. Lipari Island magma being stored and transported in

an oceanic environment makes it likely for magma to have interacted with carbonate rocks during ascent. Tate marble provides an experimental analog for these carbonate rocks.

2.7 Spherulites

In silicic glasses, spherulites contain radiating feldspar, cristobalite, and quartz, defined by their spherical shape with maximum diameters rarely above a few centimeters (Smith et al., 2001). The exact mechanisms of spherulite formation timescales, temperatures, and growth conditions are still open questions (Watkins et al., 2009; Bullock et al., 2017). However, spherulites can grow above and below the glass transition temperature (T_g). Above T_g, spherulites crystallize in undercooled melt. Below the T_g, formation occurs after emplacement by hydration. In both instances, spherulites nucleate on a crystal or vapor bubble (Clay et al., 2013; Seaman et al., 2009). Different textures of Rocche Rosse spherulites are used to identify types of spherulite-forming processes. Clay et al. (2013) propose that Rocche Rosse obsidian spherulites begin to form under high-temperature crystallization and continue post-emplacement while temperature is reduced. At magmatic temperatures (>790-825 °C), crystallization of sanidine and cristobalite (anhydrous phases) causes accumulation of H_2O in the melt on the immediate outside of the newly formed spherulite. Spherulite textures during this phase are small and radial (Bullock et al., 2017). Between 800 and 300 °C, spherulites further crystallize and grow to combine into aggregates of several millimeters in size in low-shear regions (Clay et al., 2013). Intensive deformation can occur during downslope transport of the lava flow. Emplacement deformation creates large-scale folding where dense crystalline bands of spherulites can form. Low-temperature nucleation growth occurs (<650 °C) where nucleation becomes preferred over crystal growth. Preserved spherulite geometry in Rocche Rosse obsidian varies depending on formation temperature and deformation induced by the original lava flow and emplacement (Fig. 4.) (Bullock et al., 2017).

CHAPTER 3

MATERIALS AND METHODS

Materials and methods for experiments need to be characterized. Here, collected samples from the Rocche Rosse lava flow are described. Helium pycnometry, viscometry, STEM/SEM, and conduit experiments are explained with concepts and parameters.

3.1 Rocche Rosse Samples

Obsidians and pumices from Lipari Island were collected at 11 different sites during the field campaign of June 2023. Stop-1 and Stop-11 are the sampling sites within the fall-out pumice deposits of Monte Pilato. Specifically, Stop-1 represents the upper sequence of the eruption event, and Stop-11 represents the lower sequence, ~9 m above sea level along the edge of the Porticello quarry. Stops 2-10 form a vertical transect of the Rocche Rosse lava flow deposit and follow the center of the flow, increasing in elevation from 96 to 161 m. The middle of the lava flow was selected for sample collection to avoid any physical and chemical alteration induced by external water on the shoreline during the emplacement of the lava flow. The designation of obsidian samples follows the classification of Rocche Rosse obsidians set by Shields et al. (2016), with additional descriptions of spherulite concentrations for glass obsidians. Obsidians are generally vesicle-poor and appear banded with localized, highly elongated vesicular bands associated with deformation during lava flow. Frothy and glass obsidian with frothy material is found in fold hinges and vesicles included with glass. Pumiceous lava is highly vesicular with portions of obsidian bands, and shear-banded lava has low to medium vesicularity with brittle-ductile textures, obsidian bands, and shear bands. Only samples with potential experimental use or unique features such as lithics or banding were assigned labels. Glass obsidians, either spherulite rich or free of spherulites, were the primary targets when gathering samples. Samples 02-RR03, 03-

RR03, 05-RR05, 06-RR05, 08-RR07, 09-RR06, 10-RR08, 12-RR08 and 13-RR10 are glass obsidians. All samples host some amount of spherulites, but samples 05-RR05 and 09-RR06 are considered spherulite-bearing (Fig. 5 and 6).

3.2 Helium Pycnometry and Porosity

Helium gas pycnometry is a method for estimating the skeletal volume of solid grains in a porous material. A helium gas pycnometer consists of the sample chamber and the expansion chamber. At first, the sample chamber is filled with helium gas, filling all the space not occupied by the sample, and the chamber's pressure is recorded. Then, helium is allowed into the expansion chamber, and pressure is re-recorded. The pressure drop between the sample chamber (10-350 cm^3) and the expansion chamber is used to calculate the skeletal volume of the sample:

$$Vs = Vc + \frac{Vr}{\frac{P1}{P2} - 1}$$

Where V_s is the sample volume, V_c is the empty sample chamber volume, Vr is the reference chamber volume, P_1 is the sample chamber pressure, and P_2 is the reference chamber pressure. Connected porosity can be estimated by acquiring a sample's bulk, framework, and skeletal volumes. Bulk volume is the geometrical volume and includes all porosity, framework volume consists of the total solid volume with isolated pores, and skeletal volume excludes all pore space (Webb, 2001). Bulk volume (volume of solid grains and pores) is calculated by using the geometrical areas of the sample. Connected porosity is calculated by:

$$\varepsilon = \frac{Vb - Vs}{Vb_{\ connectd}}$$

Where ε is connected porosity, $V_{b\ \text{connected}}$ is bulk volume, and V_s is skeletal volume.

Total porosity of a material can be estimated by using bulk density (measured from a scale to the third decimal) and the true density recorded from pycnometry:

$$\varepsilon = 1 - \frac{\rho b}{\rho d}$$

Where ε is the total porosity, ρ_b is bulk density, and ρ_d is true density. Before obsidian cores were heated in conduit experiments, the densities and volumes of each core were determined via helium pycnometry and measuring their mass and geometrical volume. An Anton Paar Ultrapyc 3000 was used for the 12 obsidian cores, as well as powder pycnometry on spherulite-bearing and glass powder. For calibration and experiments, a 50 cm^3 medium cell was used with 15 measuring cycles. Two calibration cycles were run, with the first cycle calibrated using a small sphere ~7.10 cm^3 in volume and the second cycle using two microspheres totaling ~2.14 mm^3 in volume. To estimate variance, the mass of each sphere was entered to equal the volume. Volume variances for the first and second calibration were 0.045% and 0.099%, respectively. In both cases, volume was underestimated, resulting in an overestimated density. The density measurement margin of error for the medium and microspheres were ±7 kg/m^3 and ±25 kg/m^3, respectively.

Cores were needed for conduit experiments and were not powdered for pycnometry after heating experiments to preserve the microstructural information to be inspected in subsequent analytical investigations. For powder pycnometry, obsidian was powdered from the same samples from which the cores were drilled. To ensure that selected granite and marble would remain intact during heating experiments, parallelepipeds were cut and analyzed for density, volume, mass, and structural changes that would occur. Granite and marble samples were heated at 900 °C for 3 hours, with each sample undergoing pycnometric analysis before and after heating.

3.3 Calorimetry

Calorimetry is a thermal analysis technique used to obtain thermal changes of a material throughout heating and cooling. The two most used techniques are differential thermal scanning calorimetry (DSC) and differential thermal analysis (DTA) (Laye, 2002). In both cases, the sample is heated, and temperature is monitored by two thermocouples surrounding a platinum crucible and the sample therein (Bouhifd et al., 2012). The primary difference between DSC and DTA is how signals from each method are received. DSC records heat flow from the sample as the sample is experiencing a change in heat. DTA monitors the temperature difference between a previously heated reference and the sample (Laye, 2002). Calorimetry data consists of curves that correlate the measured heat capacity (C) with the temperature measured by the calorimeter. The specific heat capacity is the amount of thermal energy absorbed by one gram of obsidian material needed to increase its temperature and is reported in J/g˙K. The increase and decrease of heat capacity are correlated to endothermic and exothermic processes and can be ascribed to the enthalpy of reaction. The calorimetric measurements were used to determine the glass transition temperature (T_g) of the obsidian glasses (with spherulites and without them). For Lipari Island obsidians used in this study, DSC was used with the sapphire method, which consists of four steps. The first step uses an empty crucible to make corrections for factors that can cause fluctuations in calorimetry scans from laboratory to laboratory. The second step calibrates the instrument with sapphire from the correction scan. The third step measures the heat capacity of the sample against the correction scan. Finally, the fourth step reheats the sample and calculates the heat capacity of the remelted glass (Johnson, 2024; Halverson et al., 2024).

Using glass chips at ambient pressure between room temperature and 100 °C above the T_g, a Netzsch DSC 404 F1 Pegasus Differential Scanning Calorimeter (University of Texas in San Antonio) was used. For calibration and experimental runs, heating was up to 1300 °C at 30 °C/min while maintaining 30 ml/min Ar gas flow for an inert atmosphere. Before obsidian samples were heated, two baselines were run with an empty-covered platinum crucible (~161 mg) and two with a sapphire disc (~64 mg) in the crucible. Samples were heated twice. The first heating was done with sample powders, and the second heating was a reheating of glasses formed from heating the initial obsidian powders. Heat capacity data was downsampled at every 1 °C increment and recorded using the Proteus software. Glass transition temperatures were calculated by the software after manually selecting the onset of the first heat capacity peak of sample glass and the middle of the trough measuring the heat capacity of the sample liquid. Glass temperature transition captures a range of temperature where the user identifies the peak onset and trough.

3.4 Viscometry

Viscosity as a ratio of stress and strain rate represents the most important parameter to quantify the transport and emplacement of magmas (Giordano et al., 2008). Experimental methods to measure viscosity involve a wide range of viscometer instruments depending on the viscosity and geometry of the analyzed material. Modern approaches, such as parallel plate viscometry, heat a material and compress it with a set weight to measure the ratio of stress and strain rate and, thus, viscosity. This approach is commonly used in measuring the high-viscosity materials with viscosity ranges between ~10^8 and ~10^{14} Pa·s, typical for andesitic to rhyolitic magmas at < 1000 °C (Whittington et al., 2009).

The viscosity of Lipari Island obsidians was measured using a Theta Industries Rheotronic III 1000C Parallel Plate Viscometer (University of Texas in San Antonio), which consists of two cylindrical silica glass plates with a sample inserted between, with the weight (placed above the top plate) exerting the stress onto the top surface of the cylindrical sample. For parallel plate viscosity experiments, samples 13-RR10 (Fig. 7b) and 09-RR06 were chosen for core drilling with 09-RR06 (spherulite-bearing) and 13-RR10 (spherulite free). Sample 09-RR06 was selected over 06-RR05 due to a lack of other unique textures and features aside from spherulites. Sample 13-RR10 was selected because of the lack of pumice clasts and spherulites, making the 13-RR10 the glassiest obsidian collected from the suite of rocks collected from Rocche Rosse in Lipari Island. Each cylindrical sample's top and bottom surfaces were polished to ensure parallel surfaces and perfect initial contact with the platinum foils positioned between the sample and the silica glass plates used during experiments. Using a diamond core drill bit, two cylindrical samples were cored: one glass core (~6.5 mm in diameter and ~17.35 mm in length) and one spherulite-bearing core (~11.3 mm in diameter and ~18.94 mm in length). Different diameters were used for each core due to a malfunction with the larger diameter drill bit. The difference in diameter produces a minimal shift in applied stress between the two sample diameters during experiments: 0.3 MPa for smaller diameter cores (6.5 mm) and 0.1 MPa for larger diameter cores (11.3 mm). The viscosity of each sample was measured at different temperatures between 750 and 970 °C above T_g, with a constant uniaxial load of 1000 g. Using a K-type thermocouple, temperature was measured and held within ±0.1 °C along each viscosity measurement. Viscosity is calculated from the longitudinal strain rate measured via viscometer, instantaneous area (area of the object at a specific time), and known load applied onto the cylindrical sample (Gent, 1960).

3.5 Viscosity Estimations Using Empirical Models

Viscosity was measured using parallel plate viscometry and by fitting parallel plate measurements to empirical models. Several models exist for estimating the viscosity of rhyolitic magmas by considering magma properties such as the chemical composition of the silicate melt and its volatile (mainly H_2O) concentration, temperature, and confining pressure (Giordano et al., 2008; Hui and Zhang, 2007, Romine and Whittington, 2015). However, for magma flow in volcanic conduits located at shallow pressure (< 300 MPa or < 13 km depth based on Lipari obsidian density of ca. 2350 kg/m^3; La Monica et al., 2019) where constant composition and temperature occur, simpler models are preferred (Romine and Whittington, 2015), such as the Arrhenius model:

$$\log \eta = A + \frac{B}{T}$$

Where η is viscosity in Pa·s, A is the log η (Pa·s) intercept at infinite temperature (x-axis of 0), B is the activation energy associated with viscous flow in J/mol^{-1}·K, and T is temperature in K (Bottinga and Weill, 1972). Arrhenius equations describe the dependence of melt viscosity on temperature. More recently, the relationship between temperature and viscosity is more accurately described as non-Arrhennian. This is because Arrhenius models are unsuccessful when applied to temperatures approaching the glass transition, when depending on water concentration (Giordano et al., 2008), which causes viscosity to increase sharply by several orders of magnitude at <1wt.% (Hess and Dingwell, 1996), and because model curvatures having large amounts of variation depending on the chemical composition of the melt. The less SiO_2 in the system, the weaker the Arrhenius relationship is (Dingwell, 1993). The Arrhenius equation is then replaced by the non-Arhennian Vogel- Fulcher-Tammann (VFT) equation (Vogel, 1921; Fulcher, 1925; Tammann, 1926; Hess and Dingwell, 1996; Russell et al., 2022):

$$\log \eta = A + \frac{B}{T - C}$$

This empirical approach adds the new variable *C* to describe a constant temperature (K) where viscosity goes to infinity. Currently, the most appropriate viscosity model for fitting the viscosity data of Lipari Island obsidians is the one proposed by Romine and Whittington (2015) that best quantifies the viscosity of rhyolites from Lipari Island (72.08 wt.% SiO_2) with low water concentrations (0.01 and 1.2 wt.% H_2O):

$$\log \eta = -4.40 + \frac{11609 - 1248 \ln(w + 0.17)}{T - (140.1 - 62.3 \ln(w + 0.17))}$$

$$- P\left(0.0082 + 0.000051w - \frac{0.95}{T}\right)$$

Where η is viscosity in Pa·s, *w* is wt.% water content, *P* is pressure in MPa, and *T* is temperature in K. By using a parallel plate viscometer and the VFT equation, the viscosities for spherulite-bearing and glass obsidians are best estimated. Water contents of selected samples were unknown and not measured, so the model of Romine and Whittington (2015) was not used to estimate viscosity. However, by using the above equation suggested by Romine and Whittington (2015), water concentration can be estimated from VFT viscosities at specific *T* using Excel solver. Excel Solver finds the value of an objective cell (set equation) by changing variables with limits set by the user. For VFT and Arrhenius models, the equation for each model is set as the objective cell, and A, B, and C are the variables. B is set to be equal to or greater than zero.

3.6 STEM and SEM

Scanning transmission electron microscopes (STEM) allow for nanometer-resolution images of biological and inorganic materials. STEM is a variation of a transmission electron

microscope (TEM). The Inner components of TEM are divided into the field emission source, the condenser lens, the objective lens, and the projector lens. The field emission source generates an electron beam from a tungsten needle where negatively charged electrons are attracted to the positive electrical currents output by metal rings. The voltage of each metal ring increases by tens of thousands to accelerate the electron beam until the speed is greater than half of the speed of light (Williams and Carter, 2009). The reason for this speed is so electrons can pass through the specimen and shorten the wavelength of the electrons to achieve higher resolutions. The condenser lens bends and narrows the electron beam by creating a magnetic field with copper encased in soft iron tubing (Williams and Carter, 2009). After sufficiently condensing electrons, the beam passes through the sample in the objective lens, where the beam is magnified. As the beam passes through the sample, electrons are scattered by the different elements and densities of the materials, leaving an imprinted image. While the afterimage is traveling through the projector lens, the beam is demagnified and reflected off a screen where the image of the specimen can be viewed by a camera (Egerton, 2016).

A scanning electron microscope (SEM) works similarly to the TEM, but the electron beam is further focused to scan across the sample where backscattered electrons provide topographic details of the specimen surface. Backscattered electrons are electrons produced by the electron beam as electrons contact the sample atom's nuclei. Due to the force electrons feel from positive charges, the trajectory of the electrons changes course. X-rays are also backscattered and analyzed with Energy Dispersive X-ray Spectroscopy (EDS) to give chemical compositions for elemental analysis. STEM combines TEM and SEM by scanning the specimen the same way as SEM while also providing images by transmitted electrons passed through the specimen. This allows the inner structure to be viewed at a higher resolution and chemical

analysis to be done simultaneously. Topography of bulk samples can also be viewed at a higher resolution than SEM, as electron scattering is reduced as the beam penetrates the specimen (Egerton, 2016).

For Lipari obsidians, a heating stage was used to simulate the vesiculation of bulk obsidian powder in situ above T_g. EDS was also used to record bulk chemical changes and evaluate mineral formations after heating. Textural and chemical analysis of spherulite-bearing and glass obsidians at temperatures from 500 to 1000 °C were conducted using a Hitachi SU9000EA STEM (Georgia Electron Microscopy) using 30.0 kV beam voltage. Images were taken utilizing backscattered electron images and EDS equipped on the STEM. A Hitachi SU-3900 Cryo SEM with a 20.0 kV beam voltage was also used at the same facility. Samples 06-RR05 and 12-RR08 were selected for STEM heating experiments. Sample 06-RR05 represents spherulite-bearing obsidians, and sample 12-RR08 (Fig. 7a) represents spherulite-free obsidians. Preparation of obsidian samples first involved pulverizing and sieving powder through a NO. 270 53 μm sieve. Small shards were observed under light for glass obsidians to ensure no spherulites or microlites were present. Obsidian powder mixed with distilled water underwent sonification for ~20 minutes to separate smaller grains to the top of the solution. Following sonification, Kimtech® wipes were used to brush obsidian particles onto a Nordica TEM heating chip. After viewing the chip under a Leica DVM6 light microscope to ensure obsidian grains were correctly oriented on chip sites, the chip was then inserted into the STEM and left overnight under vacuum. Before heating, each site of potential interest was inspected to decide which locations would be best to observe in-situ sample vesiculation and associated nanostructural changes. Four sites were selected for each spherulite-bearing and glass obsidian experimental session. However, once 900 °C was reached in glass obsidian

powder, changes occurred far too rapidly to keep track of each site. As a result, Sites 1 and 3 exhibited the most notable features and were attentively observed up to 1000 °C. Sample temperatures were increased by 100 °C increments with an extra increment of 50 °C at 650 °C in glass obsidian for potential textural changes at nanoscale occuring at T_g. Map and point analyses via EDS were acquired after cooling to room temperature from each temperature above T_g (800-1000 °C) to record chemical changes associated to observed textural changes at nanoscale. After heating cores, RRG-01 and RRS-01 were selected for SEM. SE images were taken along the contact between the conduit and the jacket to capture deformation.

3.7 Conduit Experiments

For conduit experiments, ~12.70 mm diameter obsidian cores were drilled to ~24 mm in height. A total of 12 cores were drilled: 6 spherulite-bearing samples and 6 glass ones. For spherulite-bearing obsidian, cores were drilled perpendicular to foliation. Ten jackets of granite were drilled to the same dimensions so obsidian cores (Table 3 and Fig. 9) would fit as snugly as possible. The faces of each obsidian core were polished to ensure cores sit as flat as possible in each granite jacket. The weights of cores and jackets were measured individually, and the cores were inserted into jackets. The heights and diameters of each core were recorded with a digital micrometer. Granite jacket heights were measured using a Mitutoyo Absolute Digimatic Indicator. Reported measurements were averaged from five recordings of each dimension. Using an MTI Corporation KSL-1200X furnace (University of Texas in San Antonio), experimental temperatures ranged from 950 to 1150 °C at increments of 50 °C with a heating and cooling ramp of 10 °C/minute. Each experiment consisted of one spherulite-bearing and one glass obsidian core inserted into its own granite jacket. The final 1150 °C experiment also included a pair of unjacketed obsidian cores and a granite core. Each sample was

weighed after heating using preheated and post-heated weights for loss on ignition (LOI) estimations. Conduits were cut three times to view internal textures along the tops, middles, and margin contacts between the granites and obsidians. The first cut removed the top of the conduit, the second was a cut along the granite and obsidian contact margin, and the third cut was through the center of the obsidian core (Fig. 9). Due to the mix of spherulites, obsidian, granite, and pumice it would not be possible to polish well by hand. Samples were largely left unpolished to avoid damaging any of the features formed by heating. Samples RRG-01 and RRS-01 were inserted into an ion mill to polish for ~3 hours until abrasions did not affect the detail of SEM images. Collected obsidian from Rocche Rosse and pumice from Monte Pilato were also polished into thin sections.

CHAPTER 4

RESULTS

4.1 Monte Pilato Field Work

Observed field sites ranged from the top to the bottom of Mt. Pilato, along with the Rocche Rosse obsidian flow (Fig. 10). Site 1 (Fig. 11) is the highest accessed point of the Mt. Pilato depositional sequence. The true bottom of this outcrop is covered by debris resulting from erosion and not exposed. The first layer of this sequence is clast supported with pyroclasts (mainly pumices of lapilli size) with interdispersed basaltic xenoliths, rhyolitic lithics, obsidian, and pumice clasts. Grains are angular and range in size from ash to lapilli. Layers 2-9 shift from clast-supported to matrix-supported, and layer 10 contains lithics/xenoliths that are spread from the bottom to the top with no specific spatial distribution. Site 11 (Fig. 12) is the lowest accessed point of Mt. Pilato (~4 m elevation) and is on the northeastern edge of the Porticello quarry. The outcrop is tens of meters in height and is composed of matrix-supported pumice ash (Fig. 12b). Highly weathered obsidian is present at the base of the outcrop (Fig. 12c). The horizontal and vertical extent of this obsidian is not clear as there is limited exposure. While the contact between Mt. Pilato tephra sequence and Rocche Rosse lava deposit is not accessible, the contact is observable in specific locations. From site 12 (Fig. 13), the contact is observable from a street bridge ~150 m away and along the shoreline. This viewpoint is too far from the contact to discern any textural or compositional information aside from where the contact occurs. The Rocche Rosse lava deposit exhibits downslope directional shearing, while Mt. Pilato shows no flow deformation. View of the contact is limited by vegetation in this location.

4.2 Rocche Rosse Field Work

The field characteristics related to Rocche Rosse, obsidian flow deposit, are based on observations of the outcrops and representative hand specimens collected in stops 2-10. Various obsidian and pumice outcrops were documented (Fig. 14-16). Outcrops are located at sites 6-10, with samples collected at every site. Site 6 (Fig. 14a) is an eroded cross-section of obsidian, 5 m wide and 2.5 m tall. The Site 7 outcrop (Fig. 15a) is an extrusion of lava. As seen by the layering of the outcrop, the base shows vertical layering, and the top is horizontally emplaced. Site 8 outcrops have large cracks (Fig. 14b) and glass vesicle-bearing layers alternating with condensed layers (Fig. 14c). Site 9 (Fig. 15b) is another erosional remnant. This outcrop is entirely constructed of pumice with broken segments scattered on the ground surrounding the outcrop. Site 10 (Fig. 16a-b) outcroppings contain obsidians with the least number of spherulites found along the lava flow. Spherulites and pumices in these obsidians were almost absent from the collected samples. Sample 05-RR-05 (Fig. 5a) collected from site 5 is spherulite-bearing with tuffisite veins and displays a lithic. Spherulites are aligned as bands along tuffisite veins, and the lithic contains different rocks, including a compacted pumice, obsidian shards, and a single feldspar crystal (Fig. 5b). Sample 09-RR06 (Fig. 6) was collected from site 6 and used for spherulite-bearing cores in heating experiments. Sample 13-RR10 (Fig. 16b) is the glass sample collected and was used as a spherulite- and vesicle-free starting material for the conduit experiments. Other samples were collected along the lava flow but were not used for conduit or STEM experiments. These samples were too weathered or contained extensive amounts of frothy material that were not visible until cut open. Because of this, they were not ideal starting materials for the planned laboratory experiments. Thin sections (Fig. 17 and 18) show intact vesicles in obsidians

and deformed vesicles in pumices. In the obsidian thin section (Fig. 17 a/f), various minerals, including spherulites, are present (quartz, albite, and orthopyroxene).

4.3 Pycnometry

Total porosity from glass obsidian cores ranged from 4.03 to 5.16 % (Table 3). Total porosity for spherulite-bearing cores was lower, ranging from 2.14 to 2.81 %. True density averaged 2334 kg/m^3 and 2353 kg/m^3 for glass cores and spherulite cores, respectively. Spherulite-bearing sample powder's true density was lower (2391 kg/m^3) than the glass sample powder (2444 kg/m^3). Post-heated granite experienced an increase in bulk volume and connected porosity (9.53%), while mass and bulk/true density decreased. Data shows the total porosity is almost entirely connected porosity. With a higher than expected 5.81% total porosity before heating and 9.55% total porosity after heating. Skeletal volume recorded from the pycnometer remained almost unchanged. Isolated porosity was not measured for granite samples. Each sample was heated after the initial pycnometer runs, and without knowing initial isolated porosity, powdering heated samples would not have provided any information on how heating changed total porosity. Extra granite could have been powdered to acquire more porosity information, but each granite parallelepiped remained intact and was structurally sound enough for experiments paired with obsidian cores. When marble was heated, every sample fractured, breaking into multiple pieces. The inability of Tate Marble to remain intact disabled its use for jacket and obsidian core experiments, thereby leaving Elberton granite as the only remaining jacket material for the conduit experiments.

The Bulk volume for Elberton Granite heated to 900 °C and held for three hours increased from 0.80 to 0.83 cm^3. Density decreased from 2634 to 2627 kg/m^3. The increase in bulk

volume and decrease in density caused total porosity to increase from 5.80 to 9.53% after heating. The core remained structurally intact with no apparent deformation observable by eye.

4.4 Calorimetry

The change in heat capacity from the onset to the inflection point of the glass obsidian is 0.217 J/g˙K (Fig. 19) with the T_g onset of 685.8 °C and an endpoint of 798.7 °C. On reheat, the change in heat capacity decreases to 0.108 J/g˙K (Fig. 20) with a T_g onset increased to 693 °C and an endpoint of 794.8 °C. Spherulite-bearing obsidian has a lower T_g on initial heating and reheat. The spherulite-bearing samples change in heat capacity from the onset to the inflection point is 0.200 J/g˙K (Fig. 21) with the T_g onset temperature of 669.7 °C and an endpoint of 756.8 °C. On reheat, the change in heat capacity decreases to 0.175 J/g˙K (Fig. 22) with a T_g onset increase to 729.7 °C and an endpoint of 781.3 °C. Including the 161.37 mg platinum crucible, the glass sample's powder mass was 219.98 mg before heating and dropped to 219.68 mg after heating, resulting in a loss on ignition (LOI) of 0.30 ±0.01 mg, equivalent to a loss of 0.51±0.02 wt.%). The spherulite-bearing obsidian powder weighed 194.47 mg and dropped to 194.25 mg after heating, totaling a LOI of 0.22 ±0.01 mg, equivalent to ~0.664±0.03 wt.%).

4.5 Parallel Plate Viscometry

The VFT model was used for glass obsidian, and the Arrhenius model was used for the spherulite-bearing obsidian. Different model fits were used because of Excel solver calculating spherulite A and B model fits as equal values when temperature is set as ≥ 0 for VFT. The value is negative if the temperature is not set as ≥ 0. Initially, the spherulite-bearing sample is less viscous than its glass counterpart (Fig. 23), showing a difference of ~0.27-0.08 Pa·s for the two samples (Tables 3 and 4), with the gap diminishing as temperature increases. When extrapolating conduit experiment temperatures to model fits (Fig. 24), the spherulite-bearing sample becomes

more viscous than the glass sample at 1050 °C. Glass obsidian core height was compressed by 10.04 mm, with a pre-experimental height of 17.35 mm and a post-experimental height of 7.31 mm (Fig. 25). (Table 4). For the spherulite-bearing core, a total compression of 7.15 mm occurred, with a pre-experimental height of 18.94 mm and a post-experimental height of 11.79 mm (Fig. 25) (Table 5). Maximum temperatures recorded were 966 °C for glass obsidian and 969 °C for spherulite-bearing obsidian. The original viscosity measured by the parallel plate viscometer is reported in Fig. 26.

4.6 H_2O wt.% Estimation by a Viscosity Model

Using the model of Romaine and Whittington (2015), H_2O concentration in the melt was estimated throughout the vesiculation of both samples of glass obsidian and spherulite-bearing obsidian at each temperature explored experimentally. Water concentration in the glass obsidian decreased from 0.34 wt.% at 700 °C to 0.20 wt.% at 1300 °C (Table 6), whereas H_2O in the spherulite-bearing obsidian diminished from 0.46 to 0.20 wt.% in the same temperature range. The spherulite-bearing sample lost almost double (0.26 wt.%) the amount of H_2O as the glass sample (0.14 wt.%) when heated from 700 to 1300 °C. Both samples reached a similar residual concentration of H_2O in the melt (0.20 wt.%) at 1300 °C (Table 6).

4.7 Glass Powder STEM and SEM

Of the four areas selected for glass obsidian (Figs. 27-30), only areas one and three showed appreciable nanostructural changes during heating. Well below T_g, at 500 °C, area one showed pre-existing localized vesicles in the powder grain. Once 700 °C was reached, these vesicles expanded and connected (Fig. 27 and 28). These pores continued to expand as temperatures increased through 900 °C. Once 1000 °C was reached, the pores collapsed in area one, disinte-

grating the locations where they were present (Fig. 29). The rest of the grain in area one remained intact by comparison. Area three also contained these vesicles (Fig. 27) but were less widespread than in area one. Vesiculation occurred in area three along with nucleation and growth of quartz and plagioclase nanolites (Fig. 30). Noticeable viscous deformation of the obsidian powder in the area three also occurred. As two originally separate pieces of material conjoin at 900 °C (Fig. 30).

4.8 Spherulite-Bearing Powder STEM and SEM

Minimal activity occurred across all area of the spherulite-bearing powder. Vesicles formed at 700 °C (Fig. 31) and continued to generate and expand into 1000 °C. No noticeable mineral formations occurred, and bubbles that were seen in the glass powder were completely absent after the heating experiment. Unlike the glass powder, once 1000 °C was reached, all four areas were able to be easily monitored because of minimal textural changes at nanoscale. The only textural change observed along with vesicle generation is also seen in the glass powder, where different topographical textures in the melt become relatively uniform (Fig. 32). Observable changes with STEM at nanoscale are minimal in the whole temperature range (500-1000 °C) for spherulite-bearing powders.

4.9 Heating Experiments: RRG-01 and RRS-01

The original set temperatures for heating experiments were between 600 and 900 °C. However, after completing calorimetry and observing lackluster vesiculation during STEM experiments initial temperature was changed to 1100 °C to stimulate enhanced vesiculation within the experimental timescale (~3-4 hrs). Glass sample (RRG-01C) from 1100 °C produced a set of features present in all other heated cores (Fig. 33) with enough vesiculation to extrude material out of the granite jacket. The top half of the core contains lower quantities of glass material than

the bottom half of the core. Instead, the top half vesiculated enough to create pumice. Glass remains from the original obsidian and extends through the center and upwards into the pumiceous zone. Pumice vesicles in this zone are elongated. The extruded material from this core is ~23 mm tall, with sheared material as 10 mm of the total height (Fig. 34). No fragmentation or cracking of the granite and extruded sample is observed after the experiment. In the top portion of the extruded material, vesicles display no deformation whereas the vesicles located in the lower portion of the material extruded just above the granite conduit show elongation similar to the vesicles of the material within the granite jacket. A few fragments of granite margins are found within the foamed material. Textural characteristics along the margin of RRG-01 are similar to the textural features observed at the center of the core (Fig. 35). Along the bottom of the sample, the obsidian core filled the space left from imperfect drilling. The top of the obsidian core contains deformation around the jacket and core contact with vesicles transitioning from elongated to spherical in the center of the conduit (Fig. 36). Spherulite-bearing core RRS-01 was heated simultaneously with sample RRG-01. The entirety of this core became pumiceous, with the common occurrence of the core's periphery displaying shear elongated vesicles. In contrast, the center vesicles remain subcircular (Fig. 37). The remaining spherulites are translucent vesicle-free zones. The center plume of this sample is more irregular in shape than its glass counterpart, with the periphery extending further into the central section of the core on the left side. The eruption column from RRS-01 is ~36 mm tall, with the sheared area of the column making up 24 mm of the total height. Like RRG-01, the margin of RRS-01 reflects what occurs at the periphery of the center cut (Fig. 38). Because of deformation extending to the bottom of this sample the margin is homogeneous in texture. The top cut from RRS-01 shares the elongated vesicles around the obsidian-granite contact in RRG-01. However, the pumice is uniform in color along the edges at the center

of RRG-01, whereas RRS-01 is darker/glassier along the edges and lighter in color in the pumiceous center (Fig. 39). SEM-BSE imaging was also used to capture textural details of samples RRG-01 and RRS-01 at microscale (Fig. 40-41). BSE images show visible microlites on both samples and elongated and spherical vesicles. The contact between the periphery and center of the cores is visible, but not to the extent that would be more useful for interpreting the dynamics occurring during each heating experiment.

4.10 RRG-02 and RRS-02

After sufficient vesiculation was observed in both samples at 1100 °C, new cores were used, and the temperature was reduced by increments of 50 °C for each set of cores until vesiculation was minimal or non-existent in both glass and spherulite-bearing cores. Sample RRG-02 experienced an extreme drop in vesiculation at 1050 °C compared to RRG-01 at 1100 °C. The core remained almost completely glass, and limited sample extrusion was observed (Fig. 42). Sample RRS-02 is closer to representing RRG-01 than RRS-01. Contact between the sheared periphery and the vesiculating center generally shares the shape of RRG-01 (Fig. 43). Multiple features in RRS-02 are not observed in any other samples. Vesicles coalesced to form a millimeter-sized elongated bubble following the ascent of the peripheral portion of the sample while foaming. Spherulites located near this vesicle chain turned into orbicular structures, and a chain of spherulites appeared to prevent the periphery from reaching farther into the heated core. Vesicles below this change remained spherical. Another feature, also seen in additional spherulite samples, are elongated vesicles along the rims of spherulites. The margin cut of RRS-02 does not differ from what is observed along the center of the conduit (Fig. 44). A pair of spherulites generated pumice that intruded into the glass-rich layer preserved by the spherulite chain. This feature

also exists in the center view of the sample but is more pronounced along the margin. The top cut of RRS-02 is unchanged from the top of other samples (Fig. 45).

4.11 RRG-03 and RRS-03

At 1000 °C, RRG-03 experienced no vesiculation but was loosely attached to the granite jacket. Sample RRS-03 remained primarily glass with vesiculation limited to rims of spherulites (Fig. 46). During cutting, the sample was separated from the granite host. One large spherulite, located in the center of the core, appears to be accompanied by multiple minerals. A small chain of spherulites along the top of the margin cut generated pumice further away from the heat source (Fig. 47). Yellow stains are also present in this sample. The top line of the chain did not vesiculate or generate pumice. On the right side of the chain, vesicles are elongated. Along the top cut, the sheared section of the core along the margin present in other samples is non-existent. Even with the lack of vesiculation near the top of the sample a material extrusion of ~10 mm in height formed.

4.12 RRG-04 and RRS-04

At 950 °C, RRG-04 remained completely glass. No welding occurred with the granite jacket, and the sample was removable without any cutting (Fig. 48). Sample RRS-04 was welded into the granite jacket. No vesicles were produced around spherulites. However, temperature was still high enough to generate the translucent halos around each spherulite (Fig. 48).

4.13 RRG-05/06 and RRS-05/06

A temperature of 1150 °C was the highest reached for samples RRG-05/06 and RRS-05/06, which are glass and spherulite-bearing obsidians, respectively. Samples RRG-05 and RRS-05 were encased in granite, while the RRG/S-06 samples were isolated cores. The column

from RRG-05 was the largest from any sample at ~26.5 mm tall. The center of RRG-05 is completely vesiculated (Fig. 49). Vesicles along the bottom of the conduit are attached to the surrounding material similarly to vesicles around spherulites. The periphery and center contact are only traceable at the bottom of the conduit. Much like other samples, the margin of the core reflects what occurred in the center (Fig. 50). The top cut of RRG-05 is transparent enough for light to be transmitted through the sample (Fig. 51), allowing the contact between glass edges and pumiceous center to be better visible than other glass samples. Sample RRS-05 is also completely vesiculated (Fig. 52, 53, and 54). The contact between the periphery and center is in similar size and position compared with RRG-05. Spherulites in RRS-05 lost their spherical shape and began to flow with the ascent of generated pumices. Unlike other spherulite-bearing samples the extruded portion of the material was shorter compared to the extruded portion of the glass core heated at the same temperature, totaling only ~24 mm. Both unconfined heated samples maintained a cylindrical shape (Fig. 55). More extensive vesiculation occurred in RRG-06 than in RRS-06. Sample RRS-06 is the only sample that did not turn into a light gray color from heating. Instead, both spherulites and pumice remained dark-colored (Fig. 56).

CHAPTER 5

DISCUSSION

5.1 Viscous Flow

Experimental vesiculation of silicic magma helped reveal the physical changes that drive gas exsolution, growth, and deformation from nanoscale to microscale. At nanoscale, vesiculation was nonexistent except in areas of the glass obsidian powders 1 and 3 where pre-existing vesicles were present (Figs. 27-28). During heating to 1300 °C (Table 2), incipient plagioclase and quartz nanolite formation in the melt was observed starting at 1000 °C (Fig. 30). This nanoscopic crystallization does not, however, change the residual melt composition appreciably because no further chemical differentiation is expected from a starting rhyolitic liquid (Frimme and Okrusch, 2020). Thermodynamic simulations via Rhyolite-MELTS show the absence of chemical changes during equilibrium crystallization from 1300 to 950 °C at which quartz, feldspar, and oxides crystallize out of the melt (Table 8). During the STEM experiments, there was observable crystallization at this temperature, confirming slow crystallization kinetics in relatively cool, high-viscosity, silica-rich systems (Polacci et al., 2018). The low concentration of volatiles in these obsidians further increases viscosity (Morizet et al., 2007) and inhibits potential mineral nucleation. Therefore, the lack of crystallization at nanoscale also confirms that the residual glass phase does not experience compositional changes except for H_2O concentration reduced by vesiculation, which, in turn, affect melt viscosity (Hess and Dingwell, 1996).

Main physical changes related to vesiculation occur solely at the micro-scale, as observed in the final products of the conduit experiments. Overall, after being heated in the granitic con-

duits, the samples have similar flow morphologies, regardless of whether they contain glassy obsidian or spherulite-bearing glasses (Figs. 33-56). The major difference observed between the two types of samples used in the conduit experiments is represented by the temperature at which vesiculation initiates. Sample RRG-01 best displays the typical internal arrangement of vesicles within the conduit: sheared vesicles in the upper portion of the sample resulting pumiceous with subspherical vesicles in the center cut of the conduit, and mostly circular vesicles composing the lower portion of the sample (Fig. 33). This internal arrangement of bubble shape (elongated due to deformation versus subspherical due to reduced or lack of deformation) shows two deformation patterns that resemble laminar flow (with a parabola trend as indicated by solid black line in Fig. 33) in the lower portion (compare Figs. 33 and 57) with copresence of shear deformation at the conduit margins and pure shear in the central cut of the conduit (compare Figs. 33 and 58). The strain gradient is high along the contact between the foaming obsidian and the conduit wall. As the ascent of the conduit is driven by vesiculation, vesicles near the conduit wall are sheared by drag. Following the shape of the parabola across the conduit, the foaming material appears to be formed by a low-strain bubbles that move due to the high-strain upper zone. This flow style can result from outgassing through sheared and, in place, connected bubbles in the upper zone that extrudes out of the conduit. The pure shear of the vesicles observed in the central and upper portion of the sample is due to sample vesiculation-driven ascent and bubble stretching at the end of the conduit (Fig. 34). In natural systems pure shear components are interpreted to be associated to a deformational component near the fragmentation surface (Dingwell et al., 2016; Ohashi et al., 2021) however, pure shear in experiments is not associated with fragmentation. A similar vesicle deformation pattern is observed in sample RRS-02 in which the apex of the parabolic trend is more pronounced than the one observed in RRG-1 despite a portion of it is outside the

conduit and now removed (Fig. 43). In this sample, isolated spherulites are entrained along a trail near the central portion of the conduit. The transversal chain of smaller spherulites divide the highly vesiculated upper portion of the sample and the relatively glassy lower portion with pockets displaying clusters of spherical vesicles. The spherulite chain appears to prevent vesiculation from occurring in the lower portion of the sample. As vesiculation drives the obsidian ascent in these experiments, spherulites behave as rigid particles that enhance the internal resistance in the material while flowing. Specifically, growing bubbles during gas exsolution at 1050 °C must move forcefully and interact with the chain of spherulites, which slightly deformed and acquire a weakly folded aspect (Fig. 43). The other inspected samples (RRS-01, RRS-05, RRS-06, RRG-05, RRG-06) display completely vesiculated cores without displaying a clearly identifiable internal structure as observed in samples RRG-01 and RRS-02. The main internal arrangement of the exsolved bubbles is driven by high strain gradients at the conduit margins and subspherical vesicles with no apparent deformation (Figs. 33-56).

The absence of the parabolic profile observed in previous samples suggests that a plug flow occurs within the conduit (Fig. 59) and parabolic velocity profiles are the onsets of the plug flows. Plug flows occur because the material behaves largely as a Bingham fluid, where flow will not occur until a specific yield stress is reached (Philpotts and Ague, 2022) (Fig. 59). The extruded portions of the samples can help determine the type of flow, although most of the starting samples exceeded the height of the surrounding jacket by a few millimeters (Figs. 60-62). The extruded shape of the material during the simulated vesiculation is modulated by whether the sample is higher than the conduit, which results into a plug flow extrusion, or whether the sample is shorter than the conduit and is associated with a parabolic profile extrusion (Fig. 60-62). The missing expected plug flow of the extruded material below the granite jacket could be

associated with a potential increase of melt viscosity upon material cooling during extrusion from a body efficiently heated (granitic conduit) into a thermally insulated medium (i.e., air) as it occurs in natural magmas erupted during volcanic activity. In this scenario, prior to extensive cooling, sample extrusion might have been accompanied by initially deformed bubbles becoming spherical again due to the viscoelastic behavior of magmas (Wadsworth et al., 2017). For example, the top cut of both samples RRG-01 (Fig. 36) and RRS-02 (Fig. 46) shows vesicles elongated along the contact of the core and granite jacket, while the center of the core presents circular vesicles. Additionally, once the material is extruded from the confined conduit into the unconfined environment at the top of the conduit, outgassing may be enhanced, causing a further increase in the sample viscosity.

5.2 Brittle Deformation

Experimentally heated obsidians did not experience any evident brittle deformation. The level of stress did not overcome the material strength by generating fractures. Here, a quantification of the potential brittleness of the sample foaming and flowing in conduits is applied using the Deborah number (De), which is the dimensionless ratio between the Maxwell relaxation time of magma and the deformation time scale or characteristic time of the flow expressed as the inverse of strain rate (Pistone et al., 2015, and references therein):

$$\mathrm{De}_{\mathrm{melt}} = \frac{\eta app \dot{\gamma}}{G\infty} = \frac{\tau}{G\infty}$$

Where $\mathrm{De}_{\mathrm{melt}}$ is the Deborah number of the melt, ηapp is the apparent viscosity of the bulk magma composed of crystals, melt, bubbles in different modal proportions, $\dot{\gamma}$ is the strain rate, G_∞ is a constant $10^{10\pm0.5}$ described as the elastic shear modulus at infinite frequency of the melt phase (Dingwell and Webb, 1989), and τ is the stress. The obsidian samples used in this study do

not display pre-existing phenocrysts or microlites and, upon heating, do not experience any crystallization at nanoscale to microscale (Figs. 27-56). Therefore, no crystallinity is considered in the determination of the De. Sample cores were heated at room pressure (1 bar) and, thus, the samples experienced internal overpressure during exsolution of residual volatiles upon heating. The gas overpressure in the expanding bubbles is here assumed as the driving stress onto the surrounding melt and is calculated as the difference between the pressure at which the initial water concentration (here assumed to be identical to the LOI) is soluble in melt. This pressure is estimated using the model of Zhang et al. (2007) without the presence of CO_2:

$$C_{\mathrm{w}} = \frac{354.94\sqrt{P_{\mathrm{w}}} + 9.623P_{\mathrm{w}} - 1.5223P_{\mathrm{w}}^{\frac{3}{2}}}{T} + 0.0012439P_{\mathrm{w}}^{\frac{3}{2}}$$

C_w is total dissolved H_2O concentration (wt.%), T is temperature (K), P_w is water pressure with X^g_w as H_2O mole fraction in the gas phase, and P as solubility pressure (MPa). This model allows to estimate the pressure at which a specific water concentration is completely soluble in the rhyolitic melt. By inserting the H_2O mole fraction in the gas phase and using excel solver, the overpressure from vesiculation is also calculated. For these calculations, the molar volume and density of the water are estimated using the Java script-based fugacity calculator of pure water from the equation of state Pitzer and Sterner (1994) using the analytical solution presented in Sterner and Pitzer (1994) and the Dekker method to estimate water molar volume as a function of pressure and temperature:

$$\ln f = [\ln\rho + A^{\mathrm{res}}/\mathrm{R}T + P/\rho\mathrm{R}T]_{P,T} + \ln(\mathrm{R}T) - 1$$

where f is fugacity, A^{res} is residual Helmholtz energy, ρ is molar density (mol/cm^3), P is pressure (GPa), T is temperature (°C), and R is the universal gas constant (8.31 J·K^{-1}·mol^{-1}). Density of

water as a supercritical fluid in magmas is calculated using the Thermophysical Properties of Fluid Systems, an online calculator of the NIST Standard Reference Data (U.S. Department of Commerce). The total amount of volatiles exsolved as gas is:

$$H_2O\ melt\ (wt.\%) = \frac{\left(\frac{V}{18.015}\right)}{(100*\rho)}$$

Where V is volume (cm^3/g) and ρ is density (g/cm^3). Localized strain rate can be calculated using the empirical formulation proposed by Pistone et al. (2016; 2017):

$$\dot{y} = A\tau^n\ exp\left(-\frac{Q}{RT}\right)$$

where $\dot{y}$ is the strain rate (s^{-1}), A is the pre-exponential term or material constant ($MPa^{-n} \cdot s^{-1}$), τ is deviatoric stress (MPa), *n* is the stress component, Q is the activation energy (J/mol), T is the temperature (K), and R is the gas constant (8.31 $J \cdot K^{-1} \cdot mol^{-1}$). Assuming a shear thinning regime in which magma viscosity decreases with increasing strain rate, A, Q, and *n* are estimated as follows (Pistone et al., 2016; 2017):

$$A = \exp(19.36\ \chi^3 - 126.59\ \chi^2 + 153.5\ \chi - 65.78)$$

$$Q = 5.85\ \chi + 7.4$$

$$n = -0.52\ \chi^3 + 10.96\ \chi^2 - 17.14\ \chi + 6.95$$

where χ is the bubble volume fraction without the presence of minerals and in presence of a viscous melt. Bubble volume fraction at experimental temperatures used for the conduit experiments is estimated by extrapolating the bubble volume fraction in a similar temperature range from the in situ, time-resolved experiments of Pistone et al. (2015). After stress and strain values are acquired, apparent viscosity (η, measured as Pa·s) is calculated as:

$$\eta = \frac{\tau}{\dot{y}}$$

From here, it is possible to calculate De_{melt}. Following this, the critical Deborah number of the magma can be calculated:

$$De_{c\ magma} = De_{melt}\ (1 - \beta)$$

where $De_{c\ magma}$ is the critical Deborah number and β is the volume fraction of bubbles. From 950 to 1150 °C for the conduit experiments, the $De_{c\ magma}$ is too low for brittle behavior because a critical value of 0.004 is required to trigger fracturing in silicic systems (Pistone et al., 2015) (Fig. 63). By setting the $De_{c\ magma}$ to 0.004 and recalculating the required $De_{c\ melt}$ can be estimated:

$$De_{c\ melt} = 4.0e^{-3}\ (1 - \beta)$$

Acquiring the needed De_{melt} for brittle failure. The required stress can also be acquired by writing the first equation as:

$$\tau = \frac{De\ melt * 10^{10}}{\eta\dot{\gamma}}$$

Critical shear stress was not attained in experiments and relied only on overpressure exerted by growing bubbles.

This set of calculations provides comparisons for estimated bubble volume fractions and what is observed in heating experiments. However, image segmentation software is not able to accurately discern vesicles from heating experiments. Calculations show all but 0.01 wt.% of the 0.66 wt.% H_2O remaining in the melt at 950 °C (Table 7), but the glass and spherulite-bearing cores did not vesiculate at 950 °C (Fig. 48a). Calculations do not match water solubility of 0.1 wt.% expected at 1 atm (Zhang et al., 2007). In contrast to Arrhenius equations estimates from

spherulite bearing core viscometry (Table 5), estimated viscosities remain relatively constant with increasing temperature. Low values of De confirms the lack of cracking induced by vesiculation observed in the heated cores. Values of De related to the critical failure for crystal-free silicate melts can be as high as 0.01 (Wadsworth et al., 2019) and as low as 0.004 (Pistone et al., 2015) depending on the water concentration in the melt (the higher the water concentration, the lower the melt fragility) and the associated level of confining pressure that controls volatile concentration in melts (Giordano et al., 2008).

5.3 Role of Spherulites

The spherulite-bearing obsidian shows a slightly lower viscosity than the viscosity of the glassy obsidian (Fig. 25) owing to higher water concentration in the glassy portions surrounding the spherulites. Indeed, spherulite-bearing samples vesiculate at 1000 °C (Fig. 48), 50 °C lower than the temperature at which glassy obsidian starts to vesiculate (Fig. 43). Lower viscosity and earlier vesiculation combined with calorimetric data displaying a lower T_g for spherulite samples (Fig. 22) confirm that the spherulite-bearing obsidian starts as water-richer sample than the glassy obsidian. Experimental run products show the presence of vesicles around spherulites (Fig. 47 and 48), suggestive of potential heterogeneous bubble nucleation and growth (e.g., Shea, 2017) on spherulite surfaces acting as efficient sites for gas exsolution during heating. This style of bubble nucleation and growth is likely around spherulites because spherulites are characterized by the presence of a surrounding halo of high-water concentration that is formed during spherulite formation (Castro et al., 2008; Bullock et al., 2017). The spherulites inspected in this study can be classified as type-3 spherulite due to the presence of crystalline silica in the center of the spherulite structure (Fig. 4; Bullock et al., 2017). Thus, in combination with water-rich ha-

los, spherulites behave as efficient sites for gas exsolution as observed in sample RRS-03, showcasing signs of vesiculation around the whole surface of spherulites (Fig. 46). In sample RRS-01 vesiculating at 1100 °C, spherulites are deformed and appear to be part of the flow of the material during vesiculation (Fig. 37).

Except for samples RRG-05 and RRG-06, spherulite-bearing run products show more extensive signs of vesiculation than what was observed in foaming glassy obsidian. The portions of the samples that have high water concentration stimulate enhanced vesiculation and make these samples less viscous than the glassy obsidian, as demonstrated by the viscosity measurements and the viscosity determination via the VFT and Arrhenius models (Fig. 25). At the same time, these samples also experience potential resistance to flow due to the presence of spherulite particles at local spatial scale. The presence of minerals suspended in the melt increases the viscosity of magmas (e.g., Costa et al., 2009; Takeuchi, 2011). However, a crystal content as low as 10 vol.% does not favor a significant increase in magma viscosity (Caricchi et al., 2007) due to the loose solid network of rigid spherulites that do not hamper the overall flow of the obsidian during vesiculation (Fig. 64). For instance, the center cut of sample RRS-03 displays ~13 vol.% of spherulites (Fig. 64), the maximum spherulite content recorded in the selected suite of samples in this study. Another example is offered by the center cut of sample RRS-02 that displays ~2 vol.% of spherulites (Fig. 65). Overall, the content of spherulites as rigid particles (< 13 vol.%) may contribute to the sample's internal resistance to flow at the spatial scale of the single spherulite, but this potential viscosity increase is an unlikely contributor to the bulk viscosity of the sample flowing en mass. The overall flow of the spherulite-bearing material results is mainly controlled by gas exsolution and bubbles undergoing deformation, which contributes to the de-

crease of bulk viscosity (Oshaghi et al., 2019). At 1150 ℃, spherulite-bearing samples experience outgassing due to the increase of temperature and decrease of viscosity that allows single gas bubbles to connect and create potential permeable pathway for the gas to escape from the foaming and flowing sample.

5.4 Comparison with Natural Volcanic Systems

Heating experiments went to temperatures as high as 1150 ℃. By comparison, natural rhyolitic magmas erupt between 800 and 1000 ℃ and basaltic magmas between 1100 and 1200 ℃ (Philpotts and Ague, 2022). Samples were heated past their natural temperature to ensure enhanced and fastened vesiculation during the experimental timescale simulating vesiculation of water-poor systems that, under natural conditions, are expected to be richer in water within shallow plumbing systems (H_2O < 4 wt.% at < 4 km depth). The heating approach to stimulate vesiculation does, however, simulate a decompression process during which water exsolution from the melt largely dictates the change of viscosity more effectively than temperature increase (Hess and Dingwell, 1996) (Fig. 66).

The simulated magma flow in the conduit experiments helps decipher the internal dynamics of plug flows that commonly occur at silicic volcanoes erupting lava domes in effusive and explosive styles (Pistone et al., 2017, and references therein). Lava domes are high-viscosity magmas that can also build up internal pressure until they can fragment violently and trigger explosive episodes (Sparks, 1997). Lava dome growth can cause explosive eruptions by increasing the accumulation of exsolved volatiles and preventing their escape through conduit walls and lava dome plugs, increasing the hazardous potential of the extruded body (Tanguy, 2004). For example, the May 8th, 1902, eruption of Mount Pelée was the result of a plug flow creating a lava dome in the crater that suddenly decompressed, creating an eruption column accompanied

by a pyroclastic flow (Gueugneau et al., 2020) that caused 28,000 fatalities (Tanguy, 1994). Other examples of similar activity also include Redoubt, a volcano in Alaska, that formed 14 lava domes between 1989 and 1990, 13 of which fragmented by explosive activity. Also, in 1980, Saint Helens extruded two lava domes that were subsequently destroyed by explosive activity (Dzurisin, 2018).

The heating experiments conducted in this study do not capture the full physical dynamics of the explosive-effusive transition proposed for the volcanic activity of Mount Pilato and Rocche Rosse in Lipari Island. However, the experiments offer insights into the conditions of pre-eruptive magma movement upon drastic vesiculation that either lead to explosive activity when gas is accumulated mainly in the magma (eruptive phase of Mt Pilato) or lead to effusive activity when gas is readily removed from the magma (eruptive phase of Rocche Rosse). Similar features can be observed comparing the microstructures between the experimental run products and representative natural rocks collected at Mt. Pilato and Rocche Rosse in Lipari (Figs. 17-18). Vesicles encased in the obsidian samples from the Rocche Rosse lava flow deposit retain their spherical shape, whereas highly deformed vesicles populate the pumice samples from Mt Pilato. Such a comparison indicates the potential role played by multiple factors, including the rate of magma ascent, the level of gas accumulation without the formation of extensive gas permeability in the magma and along the volcanic conduit walls, and the level of stress, strain, and/or strain rate that modulate the viscous to brittle transition during magma flow. Low crystallinity with individual suspended minerals such as albitic plagioclase, quartz, and orthopyroxene in glass (Fig. 17) do not contribute substantially to the increase of magma viscosity as tested with spherulites in the conduit experiments. Finally, while the heating experiments were conducted at low water

concentrations (< 1 wt.%), minor variations in H_2O content in the melt strongly control the temperature at which magma can start to exsolve water upon heating and decompression.

CHAPTER 6

CONCLUSIONS AND FUTURE WORK

6.1 Conclusions

The interpretation of the complete data set suggests small shifts of H_2O concentrations modulate the level of gas exsolution at temperatures relevant to magmatic systems. Vesiculation-driven ascent was observed in spherulite bearing samples (0.66 wt.% LOI = assumed total H_2O) at 1000 °C, 50 °C lower when compared to foaming glassy obsidian samples (0.51 wt.% LOI = assumed total H_2O). The exact water content of each sample is unknown, but higher LOI, lower T_g, and lower viscosity confirm that spherulite-bearing samples vesiculate at initial higher water concentrations compared to the glassy obsidian samples. Nanoscale vesiculation was limited to pre-existing vesicles in the obsidian melt at 700-1000 °C. Bubble formation primarily occurred at the microscale, as observed in the conduit experiments simulating the flow of foaming material. During vesiculation, all materials experienced plug flow induced by enhanced vesiculation stimulated by temperature increase. Before material extrusion, gas bubbles underwent simple shear through the conduit domain and pure shear in the center of the upper portion. Spherulites as rigid particles do not contribute substantially to changes in bulk viscosity of the foaming samples; they act as efficient sites of bubble nucleation and growth due to initial halos of water-rich glassy bands surrounding each spherulite. Elberton Granite jackets preserved each obsidian core during heating by preventing open system outgassing through jacket walls. Estimated bubble volume fractions from previous studies (Pistone et al., 2015) and gas phase estimated do not correspond with what is observed from heating until 1100 °C. Obsidian subject to heating had a viscous flow and did not experience brittle failure. Stress from overpressure of vesicle formation and expansion was inadequate to reach a minimum critical Deborah number of 0.004 required

for the foaming material to fragment. The experimental work of this study offers important insights into deciphering the natural textures of the rocks erupted from the two eruptive activities of Mt Pilato (explosive phase) and Rocche Rosse (effusive phase). Such a comparison allows us to infer that the efficiency of gas accumulation versus gas escape through the permeable network is the main parameter that modulates the transition from explosive to effusive dynamics at volcanic centers in Lipari.

6.2 Future Research

FTIR (Fourier Transform Infrared Spectroscopy) should be used to analyze obsidians to acquire precise H_2O percentages to strengthen the results of these experiments further. Knowing the exact H_2O concentration is vital and would allow for more confident interpretations. Water concentration in this study was assumed to be represented by the LOI, but other volatile phases, such as CO_2 and S, are present in residual glass of obsidians and, thus, were potentially available in the ascending magmas prior to eruption. Heating experiments using different jacket materials would also be of interest, as marble in this study failed. Structural failures not present in granite jackets could appear. Findings from this study provide a point for future work to establish the influence of volatile concentration on the formation of specific velocity profiles during magma flow in conduits. If repeat experiments are executed, the top of each obsidian core should be at most the height of the granite jacket. If the core is cut shorter than the jacket, then the velocity profile is expected to have a better chance of being visible based on the shape of the extruded material. If cores could be separated from jackets and accurately analyzed for porosity, then calculations estimating strain rates and Deborah numbers would benefit from better measurement accuracy. Further experimental understanding of how extruded material relates to the material

flow within the conduit could be used to infer how the modality of emplacement of lava domes is controlled by the processes occurring in the conduit.

References

Avard, G., and Whittington, A.G., 2012, Rheology of arc dacite lavas: experimental determination at low strain rates: Bulletin of Volcanology, v. 74, p. 1039–1056, doi:10.1007/s00445-012-0584-2.

Bagdassarov, N.Sh., and Dingwell, D.B., 1992, A rheological investigation of vesicular rhyolite: Journal of Volcanology and Geothermal Research, v. 50, p. 307–322, doi:10.1016/0377-0273(92)90099-Y.

Benson, P.M., Heap, M.J., Lavallée, Y., Flaws, A., Hess, K.-U., Selvadurai, A.P.S., Dingwell, D.B., and Schillinger, B., 2012, Laboratory simulations of tensile fracture development in a volcanic conduit via cyclic magma pressurisation: Earth and Planetary Science Letters, v. 349–350, p. 231–239, doi:10.1016/j.epsl.2012.07.003.

Blackburn, E.A., Wilson, L., and Sparks, R.S.J., 1976, Mechanisms and dynamics of strombolian activity: Journal of the Geological Society, v. 132, p. 429–440, doi:10.1144/gsjgs.132.4.0429.

Bonechi, B. et al., 2024, Direct observation of degassing during decompression of basaltic magma: Science Advances, v. 10, p. eado2585, doi:10.1126/sciadv.ado2585.

Bouhifd, M.A., Whittington, A.G., Withers, A.C., and Richet, P., 2013, Heat capacities of hydrous silicate glasses and liquids: Chemical Geology, v. 346, p. 125–134, doi:10.1016/j.chemgeo.2012.10.026.

Brown, S.K., Jenkins, S.F., Sparks, R.S.J., Odbert, H., and Auker, M.R., 2017, Volcanic fatalities database: analysis of volcanic threat with distance and victim classification: Journal of Applied Volcanology, v. 6, p. 15, doi:10.1186/s13617-017-0067-4.

Bullock, L.A., Gertisser, R., and O'Driscoll, B., 2018, Emplacement of the Rocche Rosse rhyolite lava flow (Lipari, Aeolian Islands): Bulletin of Volcanology, v. 80, p. 48, doi:10.1007/s00445-018-1222-4.

Cabrera, A., Weinberg, R.F., and Wright, H.M.N., 2015, Magma fracturing and degassing associated with obsidian formation: The explosive–effusive transition: Journal of Volcanology and Geothermal Research, v. 298, p. 71–84, doi:10.1016/j.jvolgeores.2014.12.014.

Calanchi, N., Peccerillo, A., Tranne, C.A., Lucchini, F., Rossi, P.L., Kempton, P., Barbieri, M., and Wu, T.W., 2002, Petrology and geochemistry of volcanic rocks from the island of Panarea: implications for mantle evolution beneath the Aeolian island arc (southern Tyrrhenian sea): Journal of Volcanology and Geothermal Research, v. 115, p. 367–395, doi:10.1016/S0377-0273(01)00333-X.

Calder S., Lavallée Y., Jackie E. Kendrick, Bernstein M., 2015, The Encyclopedia of Volcanoes (Second Edition): Cambridge Academic Press, p. 343-362.

Caricchi, L., Burlini, L., Ulmer, P., Gerya, T., Vassalli, M., and Papale, P., 2007, Non-Newtonian rheology of crystal-bearing magmas and implications for magma ascent dynamics: Earth and Planetary Science Letters, v. 264, p. 402–419, doi:10.1016/j.epsl.2007.09.032.

Carr, B.B., Clarke, A.B., and De' Michieli Vitturi, M., 2020, Volcanic conduit controls on effusive-explosive transitions and the 2010 eruption of Merapi Volcano (Indonesia): Journal of Volcanology and Geothermal Research, v. 392, p. 106767, doi:10.1016/j.jvolgeores.2019.106767.

Cashman, K. V., and Scheu, B., 2015, The Encyclopedia of Volcanoes (Second Edition): Cambridge, Academic Press, p. 459–471.

Castro, J.M., Schipper, C.I., Mueller, S.P., Militzer, A.S., Amigo, A., Parejas, C.S., and Jacob, D., 2013, Storage and eruption of near-liquidus rhyolite magma at Cordón Caulle, Chile: Bulletin of Volcanology, v. 75, p. 702, doi:10.1007/s00445-013-0702-9.

Clay, P.L., O'Driscoll, B., Gertisser, R., Busemann, H., Sherlock, S.C., and Kelley, S.P., 2013, Textural characterization, major and volatile element quantification and Ar–Ar systematics of spherulites in the Rocche Rosse obsidian flow, Lipari, Aeolian Islands: a temperature continuum growth model: Contributions to Mineralogy and Petrology, v. 165, p. 373–395, doi:10.1007/s00410-012-0813-x.

Coats, R., Kendrick, J.E., Wallace, P.A., Miwa, T., Hornby, A.J., Ashworth, J.D., Matsushima, T., and Lavallée, Y., 2018, Failure criteria for porous dome rocks and lavas: a study of Mt. Unzen, Japan: Solid Earth, v. 9, p. 1299–1328, doi:10.5194/se-9-1299-2018.

Costa, A., Caricchi, L., and Bagdassarov, N., 2009, A model for the rheology of particle-bearing suspensions and partially molten rocks: Geochemistry, Geophysics, Geosystems, v. 10, p. 2008GC002138, doi:10.1029/2008GC002138.

Costello, J.O., Crawford, R. F., Edwards, T. K., Grant, W. H., Higgings, M. W., LaTour, T. E., Linkous, M. A., 2002, The Tate Marble Hill window, in the marble belt of northern Georgia: Field trip guidebook, 200104.

Crisci, G.M., De Rosa, R., Esperança, S., Mazzuoli, R., and Sonnino, M., 1991, Temporal evolution of a three component system: the island of Lipari (Aeolian Arc, southern Italy): Bulletin of Volcanology, v. 53, p. 207–221, doi:10.1007/BF00301231.

Davì, M., De Rosa, R., and Holtz, F., 2010, Mafic enclaves in the rhyolitic products of Lipari historical eruptions; relationships with the coeval Vulcano magmas (Aeolian Islands, Italy): Bulletin of Volcanology, v. 72, p. 991–1008, doi:10.1007/s00445-010-0376-5.

De Rosa, R., Gillot, P., Lanzafame, G., Mazzuoli, R., 1985, The island of Lipari: IAVCEI Scientific Assembly, Excursions Guide-book, p. 114–124.

deSilva, S.L., Self, S., Francis, P.W., Drake, R.E., Carlos, R.R., 1994, Effusive silicic volcanism in the Central Andes: The Chao dacite and other young lavas of the Altiplano-Puna Volcanic Complex: Journal of Geophysical Research, v. 99(B9), p. 17805–17825, doi:10.1029/94JB00652.

Del Moro, A., Fulignati, P., Marianelli, P., and Sbrana, A., 2001, Magma contamination by direct wall rock interaction: constraints from xenoliths from the walls of a carbonate-hosted magma chamber (Vesuvius 1944 eruption): Journal of Volcanology and Geothermal Research, v. 112, p. 15–24, doi:10.1016/S0377-0273(01)00231-1.

Di Genova, D. et al., 2020, In situ observation of nanolite growth in volcanic melt: A driving force for explosive eruptions: Science Advances, v. 6, doi:10.1126/sciadv.abb0413.

Dingwell, D. B., and Webb, S. L., 1989, Structural relaxation in silicate melts and non-Newtonian melt rheology in geologic processes: Physics and Chemistry of Minerals, v. 16, doi:10.1007/BF00197020.

Dingwell, D.B., Lavallée, Y., Hess, K.-U., Flaws, A., Marti, J., Nichols, A.R.L., Gilg, H.A., and Schillinger, B., 2016, Eruptive shearing of tube pumice: pure and simple: Solid Earth, v. 7, p. 1383–1393, doi:10.5194/se-7-1383-2016.

Dzurisin, D., 2018, Mount St. Helens Retrospective: Lessons Learned Since 1980 and Remaining Challenges: Frontiers in Earth Science, v. 6, p. 142, doi:10.3389/feart.2018.00142.

Egerton, R.F., 2016, Physical Principles of Electron Microscopy: Cham, Springer International Publishing, doi:10.1007/978-3-319-39877-8.

Eichelberger, J.C., 1995, Silicic Volcanism: Ascent of Viscous Magmas from Crustal Reservoirs: Annual Review of Earth and Planetary Sciences, v. 23, p. 41–63, doi:10.1146/annurev.ea.23.050195.000353.

Esperança, S., Crisci, G.M., De Rosa, R., and Mazzuoli, R., 1992, The role of the crust in the magmatic evolution of the island of Lipari (Aeolian Islands, Italy): Contributions to Mineralogy and Petrology, v. 112, p. 450–462, doi:10.1007/BF00310777.

Fink, J.H., 1983, Structure and emplacement of a rhyolitic obsidian flow: Little Glass Mountain, Medicine Lake Highland, northern California: Geological Society of America Bulletin, v. 94, p. 362, doi:10.1130/0016-7606(1983)94<362:SAEOAR>2.0.CO;2.

Fink, J.H., 1985, Geometry of silicic dikes beneath the Inyo Domes, California: Journal of Geophysical Research: Solid Earth, v. 90, p. 11127–11133, doi:10.1029/JB090iB13p11127.

Fink, J. H., and Anderson, S. W., 2000, The Encyclopedia of Volcanoes (First Edition): Cambridge, Academic Press, p. 307-319.

Frimmel, E. H., Okrusch, M., 2020, Mineralogy An Introduction to, Rocks, and Mineral Deposits: Springer, p. 249-274.

Frontoni, A., Costa, A., Vona, A., and Romano, C., 2022, A comprehensive database of crystal-bearing magmas for the calibration of a rheological model: Scientific Data, v. 9, p. 247, doi:10.1038/s41597-022-01363-w.

Fulcher, G.S., 1925, ANALYSIS OF RECENT MEASUREMENTS OF THE VISCOSITY OF GLASSES: Journal of the American Ceramic Society, v. 8, p. 339–355, doi:10.1111/j.1151-2916.1925.tb16731.x.

Gent, A.N., 1960, Theory of the parallel plate viscometer: British Journal of Applied Physics, v. 11, p. 85–87, doi:10.1088/0508-3443/11/2/310.

Giordano, D., Russell, J.K., and Dingwell, D.B., 2008, Viscosity of magmatic liquids: A model: Earth and Planetary Science Letters, v. 271, p. 123–134, doi:10.1016/j.epsl.2008.03.038.

Gonnermann, H.M., 2015, Magma Fragmentation: Annual Review of Earth and Planetary Sciences, v. 43, p. 431–458, doi:10.1146/annurev-earth-060614-105206.

Gueugneau, V., Kelfoun, K., Charbonnier, S., Germa, A., and Carazzo, G., 2020, Dynamics and Impacts of the May 8th, 1902 Pyroclastic Current at Mount Pelée (Martinique): New Insights From Numerical Modeling: Frontiers in Earth Science, v. 8, p. 279, doi:10.3389/feart.2020.00279.

Guo, Q., Su, H., Liu, J., Yin, Q., Jing, H., and Yu, L., 2020, An experimental study on the fracture behaviors of marble specimens subjected to high temperature treatment: Engineering Fracture Mechanics, v. 225, p. 106862, doi:10.1016/j.engfracmech.2019.106862.

Halverson, B.A., A Emerson, Hammer, J., Lira, J., Whittington, A.W., 2024, Estimates of crystallinity utilizing differential scanning calorimetry: Application to the Kīlauea 2018 Lower East Rift Zone eruption: Journal of Petrology, v. 65, egae010, doi.org/10.1093/petrology/egae010.

Heap, M.J., Farquharson, J.I., Baud, P., Lavallée, Y., and Reuschlé, T., 2015, Fracture and compaction of andesite in a volcanic edifice: Bulletin of Volcanology, v. 77, p. 55, doi:10.1007/s00445-015-0938-7.

Heap, M.J., Xu, T., and Chen, C., 2014, The influence of porosity and vesicle size on the brittle strength of volcanic rocks and magma: Bulletin of Volcanology, v. 76, p. 856, doi:10.1007/s00445-014-0856-0.

Hess, K.-U., and Dingwell, D.D., 1996, Viscosities of hydrous leucogranitic melts: A non-Arrhenian model: American Mineralogist, v. 81, p. 1287-1300.

Higgins, M.W., Crawford, R.F. and Grant, W.H., 2002, The Tate-Marble Hill area and the Murphy marble belt, GEOLOGIC FEATURES OF EASTERN PICKENS, DAWSON, AND WESTERN LUMPKIN COUNTIES, GEORGIA, p. 3.

Honnorez, J. and Keller, J., 1968, Xenolithe in vulkanischen Gesteinen der Aolischen Inseln: Geol. Rundsch., v. 57: p. 719-736.

Hui, H., and Zhang, Y., 2007, Toward a general viscosity equation for natural anhydrous and hydrous silicate melts: Geochimica et Cosmochimica Acta, v. 71, p. 403–416, doi:10.1016/j.gca.2006.09.003.

Johnson, H., 2024, Heat Capacity by the Sapphire Method, https://mcl.mse.utah.edu/heat-capacity-sapphire-method/ (accessed October 2024).

La Monica, M., Rotolo, S., Foresta Martin, F., 2019, Petrographic and spectroscopic (FT-IR) study of Western Mediterranean obsidians geological sources and of a lithic collection from Ustica Island (Sicily): Annals of Geophysics, v. 61, doi:10.4401/ag-8058.

Lavallée, Y. et al., 2021, Transient conduit permeability controlled by a shift between compactant shear and dilatant rupture at Unzen volcano (Japan): Solid Earth Discussions, doi:10.5194/se-2021-127.

Lavallée, Y., Benson, P.M., Heap, M.J., Hess, K.-U., Flaws, A., Schillinger, B., Meredith, P.G., and Dingwell, D.B., 2013, Reconstructing magma failure and the degassing network of dome-building eruptions: Geology, v. 41, p. 515–518, doi:10.1130/G33948.1.

Laye, P.G., 2002. Principles of Thermal Analysis and Calorimetry: The Royal Society of Chemistry, p. 55-72.

Moynihan, C.T., Easteal, A.J., Wilder, J., 1974, Dependence of the glass transition temperature on heating and cooling-rate. Journal of Physical Chemistry, v. 78, p. 2673-2677.

Moynihan, C.T., Easteal, A.J., DeBolt, M.A., Tucker, J., 1976, Dependence of fictive temperature of glass on cooling-rate. Journal of American Ceramics Society, v. 59, p. 12-16.

Morizet, Y., Nichols, A.R.L.K., Brooker, R.A., and Dingwell, D.B., 2007, The influence of H2O and CO2 on the glass transition temperature: insights into the effects of volatiles on magma viscosity: European Journal of Mineralogy, v. 19, p. 657–669, doi:10.1127/0935-1221/2007/0019-1751.

Narayanaswamy, O.S., 1971, Model of structural relaxation in glass. Journal of American Ceramics Society, v. 54, p. 491-498.

Neuville, D.R., Courtial, P., Dingwell, D.B., and Richet, P., 1993, Thermodynamic and rheological properties of rhyolite and andesite melts: Contributions to Mineralogy and Petrology, v. 113, p. 572–581, doi:10.1007/BF00698324.

Ohashi, M., Ichihara, M., Kennedy, B., and Gravley, D., 2021, Comparison of Bubble Shape Model Results With Textural Analysis: Implications for the Velocity Profile Across a Volcanic Conduit: Journal of Geophysical Research: Solid Earth, v. 126, p. e2021JB021841, doi:10.1029/2021JB021841.

Okumura, S., Nakamura, M., Nakano, T., Uesugi, K., and Tsuchiyama, A., 2010a, Shear deformation experiments on vesicular rhyolite: Implications for brittle fracturing, degassing, and compaction of magmas in volcanic conduits: Journal of Geophysical Research: Solid Earth, v. 115, p. 2009JB006904, doi:10.1029/2009JB006904.

Okumura, S., Nakamura, M., Nakano, T., Uesugi, K., and Tsuchiyama, A., 2010b, Shear deformation experiments on vesicular rhyolite: Implications for brittle fracturing, degassing,

and compaction of magmas in volcanic conduits: Journal of Geophysical Research: Solid Earth, v. 115, p. 2009JB006904, doi:10.1029/2009JB006904.

Okumura, S., Nakamura, M., Takeuchi, S., Tsuchiyama, A., Nakano, T., and Uesugi, K., 2009, Magma deformation may induce non-explosive volcanism via degassing through bubble networks: Earth and Planetary Science Letters, v. 281, p. 267–274, doi:10.1016/j.epsl.2009.02.036.

Oshaghi, M.R., Shahsavari, M., Afshin, H., and Firoozabadi, B., 2019, Experimental investigation of the bubble motion and its ascension in a quiescent viscous liquid: Experimental Thermal and Fluid Science, v. 103, p. 274–285, doi:10.1016/j.expthermflusci.2019.01.014.

Petford, N., 2009, Which effective viscosity?: Mineralogical Magazine, v. 73, p. 167–191, doi:10.1180/minmag.2009.073.2.167.

Parfitt, E. & Wilson, L., 2008, Fundamentals of Physical Volcanology: Blackwell Science Ltd, p. 64-104.

Philpotts, R. A. and Ague, J. J., Principles of Igneous and Metamorphic Petrology (Third Edition): Cambridge University Press, p. 47-74.

Pichler, H., 1976, Carta geologica dell'Isola di Lipari (scala 1: 10,000): Firenze, Litografia Artistica Cartografica.

Pistolesi, M., Rosi, M., Malaguti, A.B., Lucchi, F., Tranne, C.A., Speranza, F., Albert, P.G., Smith, V.C., Di Roberto, A., and Billotta, E., 2021, Chrono-stratigraphy of the youngest (last 1500 years) rhyolitic eruptions of Lipari (Aeolian Islands, Southern Italy) and implications for distal tephra correlations: Journal of Volcanology and Geothermal Research, v. 420, p. 107397, doi:10.1016/j.jvolgeores.2021.107397.

Pistone, M., Caricchi, L., Ulmer, P., Burlini, L., Ardia, P., Reusser, E., Marone, F., and Arbaret, L., 2012, Deformation experiments of bubble- and crystal-bearing magmas: Rheological and microstructural analysis: Journal of Geophysical Research: Solid Earth, v. 117, p. 2011JB008986, doi:10.1029/2011JB008986.

Pistone, M., Caricchi, L., Ulmer, P., Reusser, E., and Ardia, P., 2013, Rheology of volatile-bearing crystal mushes: Mobilization vs. viscous death: Chemical Geology, v. 345, p. 16–39, doi:10.1016/j.chemgeo.2013.02.007.

Pistone, M., Cordonnier, B., Caricchi, L., Ulmer, P., and Marone, F., 2015, The Viscous to Brittle Transition in Crystal- and Bubble-Bearing Magmas: Frontiers in Earth Science, v. 3, doi:10.3389/feart.2015.00071.

Pistone, M., Cordonnier, B., Ulmer, P., and Caricchi, L., 2016, Rheological flow laws for multiphase magmas: An empirical approach: Journal of Volcanology and Geothermal Research, v. 321, p. 158–170, doi:10.1016/j.jvolgeores.2016.04.029.

Pistone, M., Whittington, A.G., Andrews, B.J., and Cottrell, E., 2017, Crystal-rich lava dome extrusion during vesiculation: An experimental study: Journal of Volcanology and Geothermal Research, v. 347, p. 1–14, doi:10.1016/j.jvolgeores.2017.06.018.

Pitzer, K.S., and Sterner, S.M., 1994, Equations of State Valid Continuously from Zero to Extreme Pressures with H_2O and CO_2 as Examples: International Journal of Thermophysics, v. 16.

Polacci, M. et al., 2018, Crystallization in basaltic magmas revealed via in situ 4D synchrotron X-ray microtomography: Scientific Reports, v. 8, p. 8377, doi:10.1038/s41598-018-26644-6.

Romine, W.L., and Whittington, A.G., 2015, A simple model for the viscosity of rhyolites as a function of temperature, pressure and water content: Geochimica et Cosmochimica Acta, v. 170, p. 281–300, doi:10.1016/j.gca.2015.08.009.

Russell, J.K., Hess, K.-U., and Dingwell, D.B., 2024, Ultramafic melt viscosity: A model: Earth and Planetary Science Letters, v. 643, p. 118899, doi:10.1016/j.epsl.2024.118899.

Seaman, S.J., Dyar, M.D., and Marinkovic, N., 2009, The effects of heterogeneity in magma water concentration on the development of flow banding and spherulites in rhyolitic lava: Journal of Volcanology and Geothermal Research, v. 183, p. 157–169, doi:10.1016/j.jvolgeores.2009.03.001.

Shea, T., 2017, Bubble nucleation in magmas: A dominantly heterogeneous process? Journal of Volcanology and Geothermal Research, v. 343, p. 155–170, doi:10.1016/j.jvolgeores.2017.06.025.

Shields, J.K., Mader, H.M., Caricchi, L., Tuffen, H., Mueller, S., Pistone, M., and Baumgartner, L., 2016, Unravelling textural heterogeneity in obsidian: Shear-induced outgassing in the Rocche Rosse flow: Journal of Volcanology and Geothermal Research, v. 310, p. 137–158, doi:10.1016/j.jvolgeores.2015.12.003.

Smith, R.K., Tremallo, R.L., and Lofgren, G.E., 2001, Growth of megaspherulites in a rhyolitic vitrophyre: American Mineralogist, v. 86, p. 589–600, doi:10.2138/am-2001-5-601.

Sparks, R. S. J. & Wilson, L., 1976, A model for the formation of ignimbrite by gravitational column collapse: Geological Society of London, 132,441-451.

Sparks, R.S.J., 1978, The dynamics of bubble formation and growth in magmas: A review and analysis: Journal of Volcanology and Geothermal Research, v. 3, p. 1–37, doi:10.1016/0377-0273(78)90002-1.

Stevenson, R.J., Briggs, R.M., and Hodder, A.P.W., 1993, Emplacement history of a low-viscosity, fountain-fed pantelleritic lava flow: Journal of Volcanology and Geothermal Research, v. 57, p. 39–56, doi:10.1016/0377-0273(93)90030-U.

Stormer, J. C. Whitney, J.A., and Hess, J.R, Petrology and Geochemistry of the Elberton Granite: Georgia Geological Society Guidebook. v. 19, p. 10-30.

Takeuchi, S., 2011, Preeruptive magma viscosity: An important measure of magma eruptibility: Journal of Geophysical Research, v. 116, p. B10201, doi:10.1029/2011JB008243.

Tammann, G., and Hesse, W., 1926, Die Abhängigkeit der Viscosität von der Temperatur bie unterkühlten Flüssigkeiten: Zeitschrift für anorganische und allgemeine Chemie, v. 156, p. 245–257, doi:10.1002/zaac.19261560121.

Tanguy, J. C., 2004, Rapid dome growth at Montagne Pelée during the early stages of the 1902-1905 eruption: a reconstruction from Lacroix's data: Bulletin of Volcanology, v. 66, p. 615–621, doi:10.1007/s00445-004-0344-z.

Tanguy, J. C., 1995, The 1902-1905 eruptions of Montagne Pelée, Martinique: anatomy and retrospection: Journal of Volcanology and Geothermal Research, v. 60, p. 87-107.

Tool, A.Q., 1946, Relation between inelastic deformability and thermal expansion of glass in its annealing range. Journal of American Ceramics Society, v. 29, p. 240-253.

Trafton, K.R., and Giachetti, T., 2022, The pivotal role of Vulcanian activity in ending the explosive phase of rhyolitic eruptions: the case of the Big Obsidian Flow eruption (Newberry Volcano, USA): Bulletin of Volcanology, v. 84, p. 104, doi:10.1007/s00445-022-01610-3.

Ventura, G., 2013, Chapter 2 Kinematics of the Aeolian volcanism (Southern Tyrrhenian Sea) from geophysical and geological data: Geological Society, London, Memoirs, v. 37, p. 3–11, doi:10.1144/M37.2.

Vogel, H., 1925, The temperature-dependent viscosity law for liquids: Physikalische Zeitschrift (in German), v. 22, p. 645.

Vona, A., Di Piazza, A., Nicotra, E., Romano, C., Viccaro, M., and Giordano, G., 2017, The complex rheology of megacryst-rich magmas: The case of the mugearitic "cicirara" lavas of Mt. Etna volcano: Chemical Geology, v. 458, p. 48–67, doi:10.1016/j.chemgeo.2017.03.029.

Vona, A., and Romano, C., 2013, The effects of undercooling and deformation rates on the crystallization kinetics of Stromboli and Etna basalts: Contributions to Mineralogy and Petrology, v. 166, p. 491–509, doi:10.1007/s00410-013-0887-0.

Wadsworth, F.B., Llewellin, E.W., Vasseur, J., Gardner, J.E., and Tuffen, H., 2020, Explosive-effusive volcanic eruption transitions caused by sintering: Science Advances, v. 6, p. eaba7940, doi:10.1126/sciadv.aba7940.

Wadsworth, F.B., Witcher, T., Vasseur, J., Dingwell, D.B., and Scheu, B., 2017, When Does Magma Break?: Springer International Publishing, Advances in Volcanology, p. 171–184, doi:10.1007/11157_2017_23.

Watkins, J., Manga, M., Huber, C., and Martin, M., 2009, Diffusion-controlled spherulite growth in obsidian inferred from H2O concentration profiles: Contributions to Mineralogy and Petrology, v. 157, p. 163–172, doi:10.1007/s00410-008-0327-8.

Webb, P.A., 2001, Volume and Density Determinations for Particle Technologists: Micromeritics Instrument Corporation.

Webb, S.L., 2021, Thermal stress, cooling-rate and fictive temperature of silicate melts. Contributions to Mineralogy and Petrology, v. 176, 78, https://doi.org/10.1007/s00410-021-01836-y.

Wenner, D. B., 1980, Oxygen, Isotope Relations in the Elberton Granite: Georgia Geological Society Guidebook. v. 19, p. 31-33.

Whitney, J.A., Wells, D.E., Rozen, R.W., 1980, Structural and Tectonic Setting of the Elberton Batholith, Eastern Georgia Piedmont: Georgia Geological Society Guidebook. v. 19, p. 1-9.

Whittington, A.G., Hellwig, B.M., Behrens, H., Joachim, B., Stechern, A., and Vetere, F., 2009, The viscosity of hydrous dacitic liquids: implications for the rheology of evolving silicic magmas: Bulletin of Volcanology, v. 71, p. 185–199, doi:10.1007/s00445-008-0217-y.

Williams, D.B., and Carter, C.B. (Eds.), 2009, Transmission Electron Microscopy: A Textbook for Materials Science: Boston, MA, Springer US, SpringerLink Bücher, 760 p., doi:10.1007/978-0-387-76501-3.

Yoshimura, S., and Nakamura, M., 2008, Diffusive dehydration and bubble resorption during open-system degassing of rhyolitic melts: Journal of Volcanology and Geothermal Research, v. 178, p. 72–80, doi:10.1016/j.jvolgeores.2008.01.017.

Zhang, Y., Xu, Z., Zhu, M., and Wang, H., 2007, Silicate melt properties and volcanic eruptions: Reviews of Geophysics, v. 45, p. 2006RG000216, doi:10.1029/2006RG000216.

Table 1: Oxide wt.% for Elberton Granite (Stormer et al., 1980) and Mounte Pilato/Rocche Rosse eruptive products (Gioncada et al., 2003).

Oxide (wt.%)	Elberton Granite	Mounte Pilato/Rocche Rosse
SiO_2	71.50	74.31
TiO_2	0.38	0.09
Al_2O_3	15.06	12.75
FeO	1.09	1.86
Fe_2O_3	0.79	0.00
MgO	0.58	0.16
CaO	1.65	0.67
Na_2O	3.98	4.14
K_2O	4.82	4.69
P_2O_5	0.10	0.01

*Reported by Gioncada et al., 2003; Stormer et al., 1980.

Table 2: Oxide wt.% for STEM glass powder areas 1 and 3 (1-5 is area 1 and 6-15 is area 3).

Oxide (wt.%)	Spectrum 1	Spectrum 2	Spectrum 3	Spectrum 4	Spectrum 5	Spectrum 6	Spectrum 7	Spectrum 8	Spectrum 9	Spectrum 10	Spectrum 11	Spectrum 12	Spectrum 13	Spectrum 14	Spectrum 15
SiO_2	87.4	88.3	86.4	87.8	88.6	60.6	60.2	63.9	66.0	64.5	60.7	95.0	94.4	96.6	82.7
Al_2O_3	11.6	11.1	11.9	11.6	10.6	21.2	16.2	19.0	12.6	17.1	16.6	2.5	3.1	1.6	5.4
Fe_2O_3	1.0	0.6	1.7	0.6	0.7	-	0.4	-	0.6	-	-	-	-	-	-
MgO	-	-	-	-	-	0.8	1.0	0.7	1.4	0.8	1.2	-	-	-	1.0
CaO	-	-	-	-	-	16.7	18.6	16.0	19.2	16.8	19.0	1.9	2.0	1.2	10.3
SO_2	-	-	-	-	-	-	2.9	-	-	-	1.9	-	-	-	-

Table 3: Sample size, mass, density, and porosity of Lipari and Granite samples used for the experimental tests in this study. G and S indicate glassy and spherulite-bearing samples respectively.

Sample	Height (mm)	Diameter (mm)	Weight (g)	Calculated Density (kg/cm^3)	True Density (kg/cm^3)	Bulk Volume (cm^2)	Skeletal Volume (cm^3)	Total Porosity (%)	Connected Porosity (%)
RRG-01	23.74	12.76	7.09	2318	2363	3.04	3.00	5.16	-
RRG-02	24.46	12.73	7.31	2348	2356	3.11	3.10	3.91	-
RRG-03	25.25	12.75	7.52	2331	2358	3.22	3.19	4.62	-
RRG-04	22.04	12.74	6.57	2339	2354	2.81	2.79	4.30	-
RRG-05	26.36	12.74	7.87	2343	2357	3.36	3.34	4.15	-
RRG-06	20.91	12.74	6.25	2345	2358	2.66	2.65	4.03	-
RRG-Pow	-	-	11.65	-	2444	-	4.77	-	-
RRS-01	27.81	12.77	8.31	2334	2358	3.56	3.52	2.38	-
RRS-02	27.79	12.76	8.29	2334	2353	3.55	3.52	2.38	-
RRS-03	25.38	12.76	7.54	2324	2347	3.25	3.21	2.82	-
RRS-04	25.69	12.77	7.69	2340	2351	3.29	3.27	2.14	-
RRS-05	21.50	12.77	6.39	2324	2359	2.75	2.71	2.81	-
RRS-06	22.11	12.76	6.59	2332	2350	2.83	2.80	2.48	-
RRS-Pow	-	-	32.47	-	2391	-	13.58	-	-
EG-03	-	-	1.97	2481	2634	0.80	0.75	5.81	5.80
EG-03-3900	-	-	1.97	2376	2627	0.83	0.75	9.55	9.53

Table 4: Glassy sample viscosity data.

								Ø=6.12 mm	h=17.35 mm
T (˚C)	10000/T(K)	Time (min)	L (cm)	ΔL (%)	σ (Pa)	γ (s^{-1})	η (Pa s)	logη (Pa s)	'FT logη (Pa s)
725	10.02	73.6	17.31	0.19	2.93E+05	2.63E-06	3.73E+10	10.57	10.88
730	9.97	74.2	17.31	0.20	2.93E+05	2.89E-06	3.39E+10	10.53	10.78
736	9.91	74.7	17.31	0.21	2.93E+05	4.20E-06	2.33E+10	10.37	10.68
740	9.87	75.1	17.31	0.22	2.93E+05	4.73E-06	2.07E+10	10.32	10.62
745	9.82	75.6	17.31	0.24	2.93E+05	6.36E-06	1.54E+10	10.19	10.52
751	9.76	76.1	17.30	0.26	2.93E+05	7.36E-06	1.33E+10	10.12	10.43
756	9.72	76.7	17.30	0.28	2.93E+05	8.93E-06	1.09E+10	10.04	10.34
760	9.68	77.1	17.29	0.30	2.93E+05	9.25E-06	1.06E+10	10.02	10.28
766	9.63	77.6	17.29	0.33	2.93E+05	1.16E-05	8.44E+09	9.93	10.19
770	9.59	78.0	17.28	0.36	2.93E+05	1.22E-05	8.04E+09	9.91	10.13
775	9.54	78.5	17.28	0.40	2.93E+05	1.53E-05	6.40E+09	9.81	10.04
781	9.49	79.0	17.27	0.45	2.93E+05	1.79E-05	5.45E+09	9.74	9.96
786	9.44	79.6	17.26	0.51	2.92E+05	1.90E-05	5.14E+09	9.71	9.87
790	9.40	79.9	17.25	0.55	2.92E+05	2.06E-05	4.74E+09	9.68	9.81
796	9.36	80.5	17.24	0.62	2.92E+05	2.37E-05	4.10E+09	9.61	9.73
800	9.32	80.8	17.23	0.67	2.92E+05	2.61E-05	3.73E+09	9.57	9.67
805	9.27	81.4	17.21	0.76	2.92E+05	3.01E-05	3.23E+09	9.51	9.59
811	9.23	81.9	17.20	0.86	2.91E+05	3.33E-05	2.92E+09	9.46	9.51
816	9.18	82.4	17.18	0.98	2.91E+05	3.97E-05	2.44E+09	9.39	9.43
820	9.15	82.8	17.16	1.07	2.91E+05	4.34E-05	2.23E+09	9.35	9.38
826	9.10	83.3	17.14	1.22	2.90E+05	4.83E-05	2.00E+09	9.30	9.29
831	9.06	83.9	17.11	1.39	2.90E+05	5.79E-05	1.67E+09	9.22	9.22
835	9.02	84.2	17.08	1.52	2.89E+05	6.49E-05	1.49E+09	9.17	9.17
841	8.98	84.8	17.05	1.74	2.89E+05	7.36E-05	1.31E+09	9.12	9.09
846	8.93	85.3	17.00	1.99	2.88E+05	8.53E-05	1.13E+09	9.05	9.02
850	8.91	85.7	16.97	2.19	2.87E+05	1.00E-04	9.56E+08	8.98	8.97
855	8.86	86.2	16.91	2.52	2.86E+05	1.17E-04	8.18E+08	8.91	8.90
861	8.82	86.7	16.84	2.93	2.85E+05	1.37E-04	6.96E+08	8.84	8.83
865	8.79	87.1	16.79	3.23	2.84E+05	1.53E-04	6.18E+08	8.79	8.78
870	8.75	87.6	16.70	3.74	2.83E+05	1.80E-04	5.24E+08	8.72	8.71
875	8.71	88.2	16.59	4.35	2.81E+05	2.17E-04	4.32E+08	8.64	8.64
881	8.66	88.7	16.47	5.05	2.79E+05	2.43E-04	3.82E+08	8.58	8.57
885	8.63	89.1	16.38	5.55	2.77E+05	2.58E-04	3.58E+08	8.55	8.52
890	8.59	89.6	16.23	6.42	2.75E+05	3.02E-04	3.04E+08	8.48	8.46
896	8.55	90.1	16.06	7.42	2.72E+05	3.66E-04	2.47E+08	8.39	8.39
900	8.53	90.5	15.93	8.18	2.69E+05	4.05E-04	2.22E+08	8.35	8.35
905	8.49	91.0	15.70	9.48	2.65E+05	4.66E-04	1.90E+08	8.28	8.28
911	8.45	91.6	15.46	10.90	2.61E+05	5.17E-04	1.69E+08	8.23	8.22
916	8.41	92.1	15.18	12.50	2.56E+05	6.26E-04	1.36E+08	8.14	8.15
920	8.38	92.5	14.97	13.72	2.53E+05	6.57E-04	1.28E+08	8.11	8.11
926	8.34	93.0	14.63	15.65	2.47E+05	7.71E-04	1.07E+08	8.03	8.05
930	8.31	93.5	14.39	17.06	2.43E+05	8.14E-04	9.94E+07	8.00	8.00
935	8.28	93.9	13.99	19.36	2.36E+05	9.31E-04	8.44E+07	7.93	7.94
941	8.24	94.4	13.57	21.80	2.29E+05	1.01E-03	7.52E+07	7.88	7.88
946	8.20	95.0	13.12	24.36	2.21E+05	1.09E-03	6.76E+07	7.83	7.82
950	8.18	95.2	12.80	26.21	2.16E+05	1.18E-03	6.10E+07	7.79	7.78
1000	7.85	-	-	-	-	-	-	-	7.27
1050	7.56	-	-	-	-	-	-	-	6.80
1000	7.85	-	-	-	-	-	-	-	6.38
1150	7.03	-	-	-	-	-	-	-	5.98
1300	6.36	-	-	-	-	-	-	-	4.98

Table 5: Spherulite bearing sample viscosity data.

								Ø=11.32 mm	h=18.94 mm
T (˚C)	10000/T(K)	Time (min)	L (cm)	ΔL (%)	σ (Pa)	γ (s^{-1})	η (Pa s)	logη (Pa s)	ARH logη (Pa s)
725	10.01	74.0	18.9182	0.09	9.74E+04	2.40E-06	1.35E+10	10.13	10.40
731	9.96	74.5	18.9167	0.10	9.74E+04	4.33E-06	7.51E+09	9.88	10.32
735	9.92	74.9	18.9148	0.11	9.74E+04	4.81E-06	6.76E+09	9.83	10.27
740	9.87	75.4	18.9126	0.12	9.74E+04	4.81E-06	6.75E+09	9.83	10.19
746	9.81	76.0	18.9089	0.14	9.74E+04	6.25E-06	5.19E+09	9.72	10.10
750	9.77	76.3	18.9062	0.15	9.74E+04	5.77E-06	5.63E+09	9.75	10.05
756	9.72	76.9	18.9026	0.17	9.74E+04	6.25E-06	5.19E+09	9.72	9.97
761	9.67	77.4	18.8982	0.19	9.73E+04	7.70E-06	4.22E+09	9.62	9.90
765	9.63	77.8	18.8947	0.21	9.73E+04	9.62E-06	3.37E+09	9.53	9.84
771	9.58	78.3	18.8885	0.25	9.73E+04	1.11E-05	2.93E+09	9.47	9.77
776	9.53	78.8	18.8813	0.28	9.72E+04	1.27E-05	2.55E+09	9.41	9.70
780	9.49	79.2	18.8757	0.31	9.72E+04	1.35E-05	2.40E+09	9.38	9.64
785	9.45	79.7	18.8668	0.36	9.72E+04	1.54E-05	2.10E+09	9.32	9.58
790	9.41	80.1	18.8599	0.40	9.71E+04	1.74E-05	1.87E+09	9.27	9.52
795	9.37	80.6	18.8484	0.46	9.71E+04	1.83E-05	1.77E+09	9.25	9.46
800	9.32	81.2	18.8363	0.52	9.70E+04	2.22E-05	1.46E+09	9.16	9.38
806	9.26	81.7	18.8225	0.59	9.69E+04	2.23E-05	1.45E+09	9.16	9.31
810	9.23	82.1	18.8128	0.65	9.69E+04	2.42E-05	1.34E+09	9.13	9.26
815	9.19	82.6	18.7977	0.73	9.68E+04	2.66E-05	1.21E+09	9.08	9.19
821	9.14	83.1	18.7807	0.81	9.67E+04	2.88E-05	1.12E+09	9.05	9.13
825	9.11	83.5	18.7688	0.88	9.67E+04	3.10E-05	1.04E+09	9.02	9.08
830	9.06	84.0	18.7490	0.98	9.65E+04	3.44E-05	9.35E+08	8.97	9.02
836	9.02	84.6	18.7275	1.10	9.64E+04	3.52E-05	9.12E+08	8.96	8.95
841	8.97	85.1	18.7044	1.22	9.63E+04	3.94E-05	8.15E+08	8.91	8.88
845	8.95	85.5	18.6875	1.31	9.62E+04	4.39E-05	7.31E+08	8.86	8.84
850	8.90	86.0	18.6595	1.45	9.61E+04	4.68E-05	6.85E+08	8.84	8.77
856	8.86	86.5	18.6295	1.61	9.59E+04	5.56E-05	5.75E+08	8.76	8.71
860	8.83	86.9	18.6071	1.73	9.58E+04	5.86E-05	5.45E+08	8.74	8.67
865	8.78	87.4	18.5685	1.94	9.56E+04	6.61E-05	4.82E+08	8.68	8.60
871	8.74	88.0	18.5251	2.16	9.54E+04	7.76E-05	4.10E+08	8.61	8.55
875	8.71	88.3	18.4921	2.34	9.52E+04	8.60E-05	3.69E+08	8.57	8.50
880	8.67	88.9	18.4371	2.63	9.49E+04	1.01E-04	3.13E+08	8.50	8.44
886	8.63	89.4	18.3743	2.96	9.46E+04	1.15E-04	2.74E+08	8.44	8.38
891	8.59	89.9	18.3031	3.34	9.42E+04	1.27E-04	2.47E+08	8.39	8.32
895	8.56	90.3	18.2485	3.63	9.39E+04	1.44E-04	2.17E+08	8.34	8.28
901	8.52	90.8	18.1575	4.11	9.34E+04	1.67E-04	1.87E+08	8.27	8.22
906	8.48	91.4	18.0551	4.65	9.29E+04	1.90E-04	1.63E+08	8.21	8.16
910	8.45	91.7	17.9760	5.06	9.25E+04	2.11E-04	1.46E+08	8.17	8.12
915	8.41	92.3	17.8467	5.75	9.18E+04	2.40E-04	1.28E+08	8.11	8.07
921	8.37	92.8	17.6978	6.53	9.10E+04	2.78E-04	1.09E+08	8.04	8.00
925	8.35	93.2	17.5867	7.12	9.04E+04	3.01E-04	1.00E+08	8.00	7.97
930	8.31	93.7	17.4049	8.08	8.95E+04	3.47E-04	8.58E+07	7.93	7.91
936	8.27	94.3	17.1924	9.20	8.84E+04	4.09E-04	7.20E+07	7.86	7.85
940	8.24	94.6	17.0375	10.02	8.75E+04	4.42E-04	6.60E+07	7.82	7.82
945	8.21	95.1	16.7808	11.38	8.62E+04	5.09E-04	5.64E+07	7.75	7.76
950	8.18	95.7	16.4900	12.91	8.47E+04	5.76E-04	4.90E+07	7.69	7.71
955	8.14	96.0	16.2808	14.02	8.36E+04	6.03E-04	4.62E+07	7.66	7.67
960	8.11	96.6	15.9404	15.82	8.18E+04	7.17E-04	3.80E+07	7.58	7.62
965	8.08	96.9	15.6862	17.16	8.05E+04	7.67E-04	3.50E+07	7.54	7.58
969	8.05	98.5	14.4924	23.46	7.28E+04	8.40E-04	2.89E+07	7.46	7.53
1000	7.85	-	-	-	-	-	-	-	7.25
1050	7.56	-	-	-	-	-	-	-	6.81
1100	7.28	-	-	-	-	-	-	-	6.41
1150	7.03	-	-	-	-	-	-	-	6.04

Table 6: H_2O wt.% estimates using the model of Romaine and Whittington 2015.

T(°C)	T(K)	P (Mpa)	Glass H_2O (wt%)	Spherulite H_2O (wt%)	VFT Glass logη (Pa s)	Arrhenian Spherulite logη (Pa s)
700	973	0.1	0.34	0.46	11.33	10.75
750	1023	0.1	0.33	0.42	10.44	10.40
950	1223	0.1	0.28	0.30	7.78	7.73
1000	1273	0.1	0.27	0.28	7.27	7.25
1050	1323	0.1	0.26	0.26	6.80	6.81
1100	1373	0.1	0.25	0.24	6.38	6.39
1150	1423	0.1	0.23	0.23	5.98	6.00
1300	1573	0.1	0.20	0.20	4.98	4.96
		H2O (wt%) Loss	0.14	0.26		

Table 7: Calculated bubble fraction, H_2O volume/density, H_2O wt.% in melt/gas, stress, localized strain, viscosity, and Deborah numbers for 0.66 wt. % H_2O spherulite bearing obsidian.

T (°C)	T (K)	Bubble Fraction (Φ)	H_2O molar V (cm^3/mol)	H_2O ρ (g/cm^3)	H2O in melt (wt.%)	H_2O in gas (wt.%)	τ (Mpa)	γ (s^{-1})	η (Pa s)	logη (Pa s)	De_{melt}	Magma $De_{critical}$	Critical De_{melt}	Critical τ (Mpa)
950	1223	0.403	101690.00	1.77E-04	0.01000007	0.64999993	3.51	1.02E+00	3.44E+06	6.54	0.00123	0.00074	0.00670	19.88
1000	1273	0.473	105849.27	1.70E-04	0.01000015	0.64999985	3.51	9.87E-01	3.55E+06	6.55	0.00123	0.00065	0.00759	21.09
1050	1323	0.543	110008.23	1.64E-04	0.01000043	0.64999957	3.51	9.76E-01	3.60E+06	6.56	0.00123	0.00056	0.00875	23.76
1100	1373	0.613	114167.00	1.58E-04	0.01000015	0.64999985	3.51	9.64E-01	3.64E+06	6.56	0.00123	0.00048	0.01034	27.38
1150	1423	0.683	118325.62	1.52E-04	0.00999989	0.65000011	3.51	9.52E-01	3.69E+06	6.57	0.00123	0.00039	0.01262	32.58

Table 8: Simulated MELTS cooling mineral percentages.

	T (˚C)	Liquid (%)	Feldspar (%)	Quartz (%)	rhm-Oxide (%)	Water (%)	Solids (%)
Glass							
	1300	99.57	-	-	-	0.43	0.43
	1250	99.57	-	-	-	0.43	0.43
	1200	99.57	-	-	-	0.43	0.43
	1150	99.57	-	-	-	0.43	0.43
	1100	99.57	-	-	-	0.43	0.43
	1050	99.57	-	-	-	0.43	0.43
	1000	98.03	1.54	-	-	0.43	1.97
	950	24.05	51.34	22.58	1.55	0.49	75.95
Spherulite Bearing							
	1300	99.44	-	-	-	0.56	0.56
	1250	99.44	-	-	-	0.56	0.56
	1200	99.44	-	-	-	0.56	0.56
	1150	99.44	-	-	-	0.56	0.56
	1100	99.44	-	-	-	0.56	0.56
	1050	99.44	-	-	-	0.56	0.56
	1000	97.95	1.49	-	-	0.56	2.05
	950	24.01	51.27	22.55	1.55	0.62	75.99

Figure 1. Google Earth map of the seven volcanic islands making up the Aeolian Archipelago (Sicily, Italy).

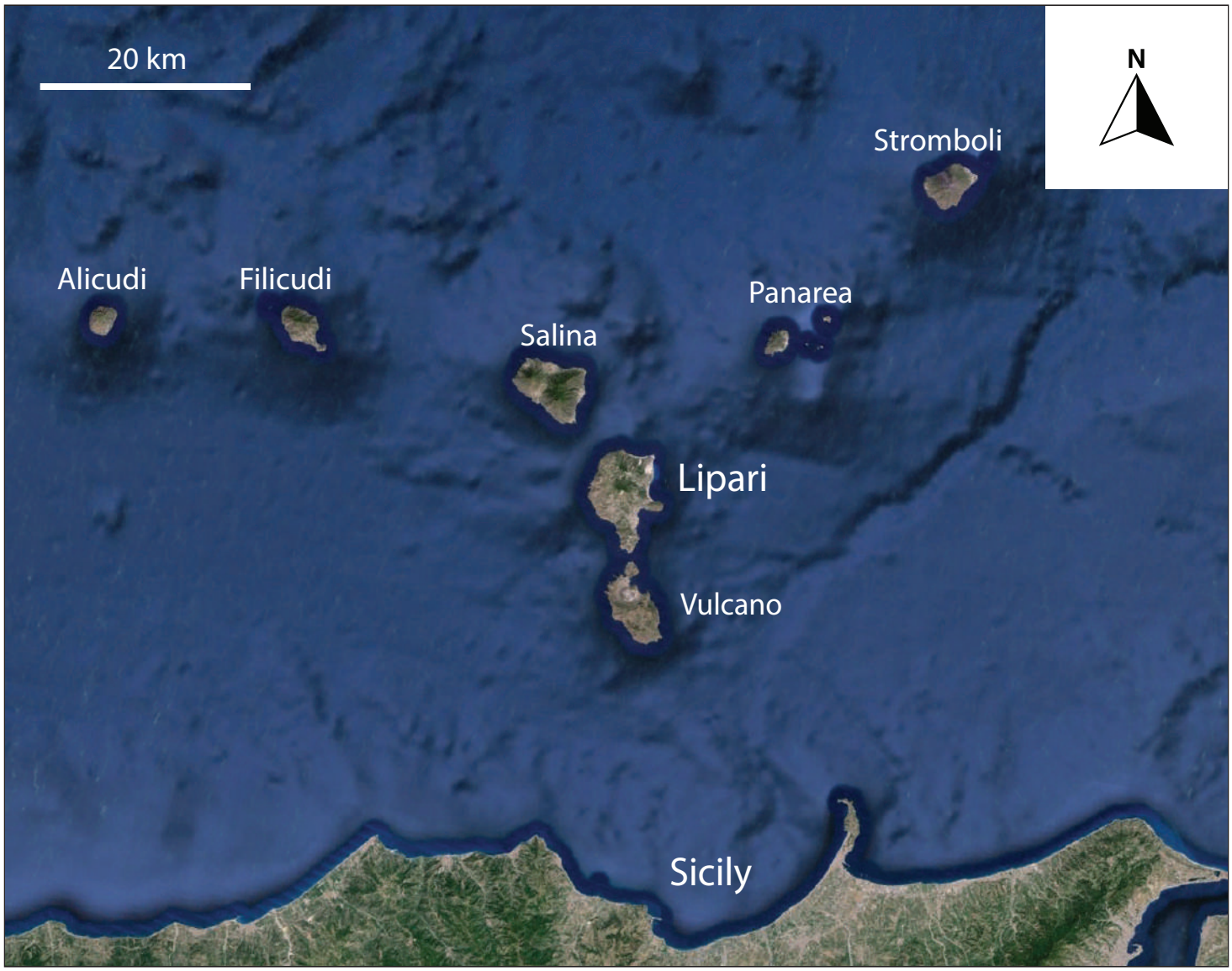
20 km
N
Stromboli
Alicudi
Filicudi
Panarea
Salina
Lipari
Vulcano
Sicily

Figure 2. Geologic map of Lipari divided into ten cycles from Crisci et al. (1991) and modified from De Rosa et al. (1985). 1, Cycle I (old volcanoes); 2, Cycle II (Costa D'Agosto-Chirica); 3, Cycle III (S. Angelo I); 4, Cycle IV (S. Angelo II); 5, Cycles V and VI (younger cycles of Costa D'Agosto and S. Angelo); 6, Cycles VII and VIII (M. Guardia I and II); 7, Cycles IX and X (V.ne Gabellotto and M. Pilato); 8, Alluvial deposits; 9, Crater rims including Mt. Pilato and Rocche Rosse; 10, Volcano-tectonic collapses.

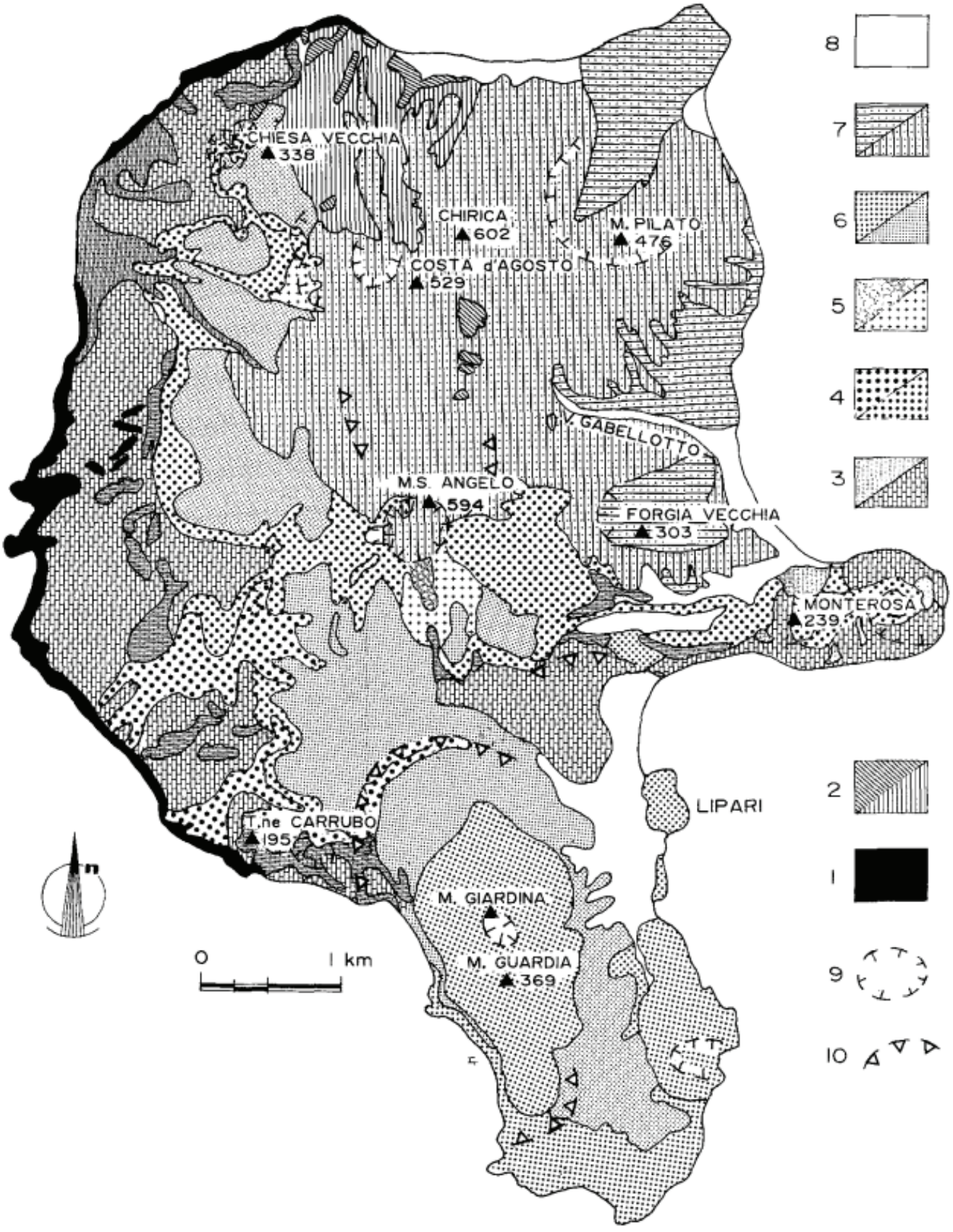
CHIESA VECCHIA
338
CHIRICA
602
M. PILATO
476
COSTA d'AGOSTO
529
V. GABELLOTTO
M.S. ANGELO
594
FORGIA VECCHIA
303
MONTEROSA
239
LIPARI
T.ne CARRUBO
195
M. GIARDINA
M. GUARDIA
369
0
1 km
8
7
6
5
4
3
2
1
9
10

Figure 3. Stratigraphic correlation of the four most recent eruptions on Lipari Island, which includes paleomagnetic ages from Pistolesi et al. (2021).

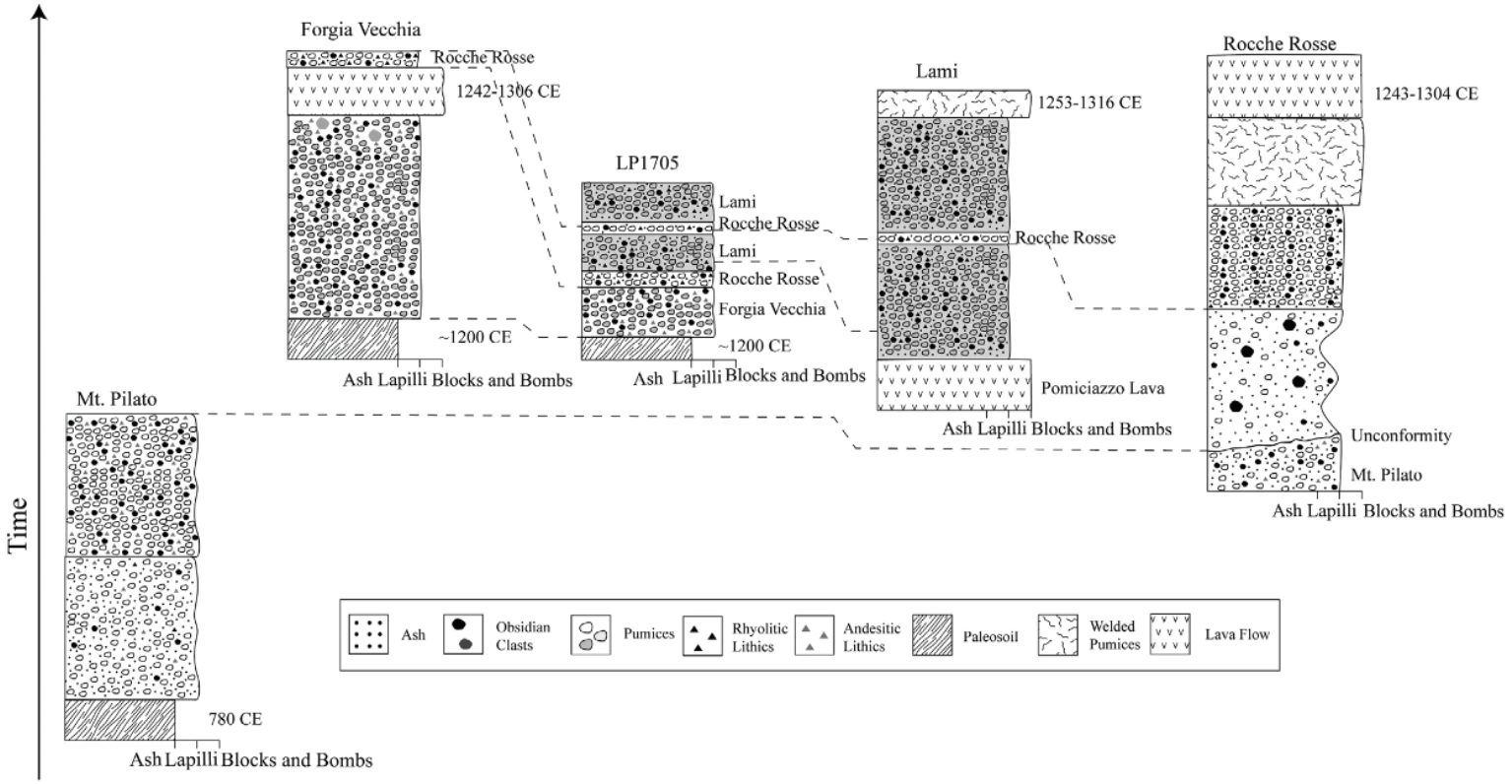
Time
Forgia Vecchia
Rocche Rosse
1242-1306 CE
~1200 CE
Ash Lapilli Blocks and Bombs
LP1705
Lami
Rocche Rosse
Lami
Rocche Rosse
Forgia Vecchia
~1200 CE
Ash Lapilli Blocks and Bombs
Lami
1253-1316 CE
Rocche Rosse
Pomiciazzo Lava
Ash Lapilli Blocks and Bombs
Rocche Rosse
1243-1304 CE
Unconformity
Mt. Pilato
Ash Lapilli Blocks and Bombs
Mt. Pilato
780 CE
Ash Lapilli Blocks and Bombs
Ash
Obsidian Clasts
Pumices
Rhyolitic Lithics
Andesitic Lithics
Paleosoil
Welded Pumices
Lava Flow

Figure 4. Classification of spherulites as a function of temperature (modified after Bullock et al., 2017). Different types of spherulite can form concurrently in different sections of a lava flow deposit. Four out of the five types can occur in the estimated Tg range. The brown dashed line represents Tg from calorimetry on obsidian glass powder from Rocche Rosse (from Fig. 18 in this study).

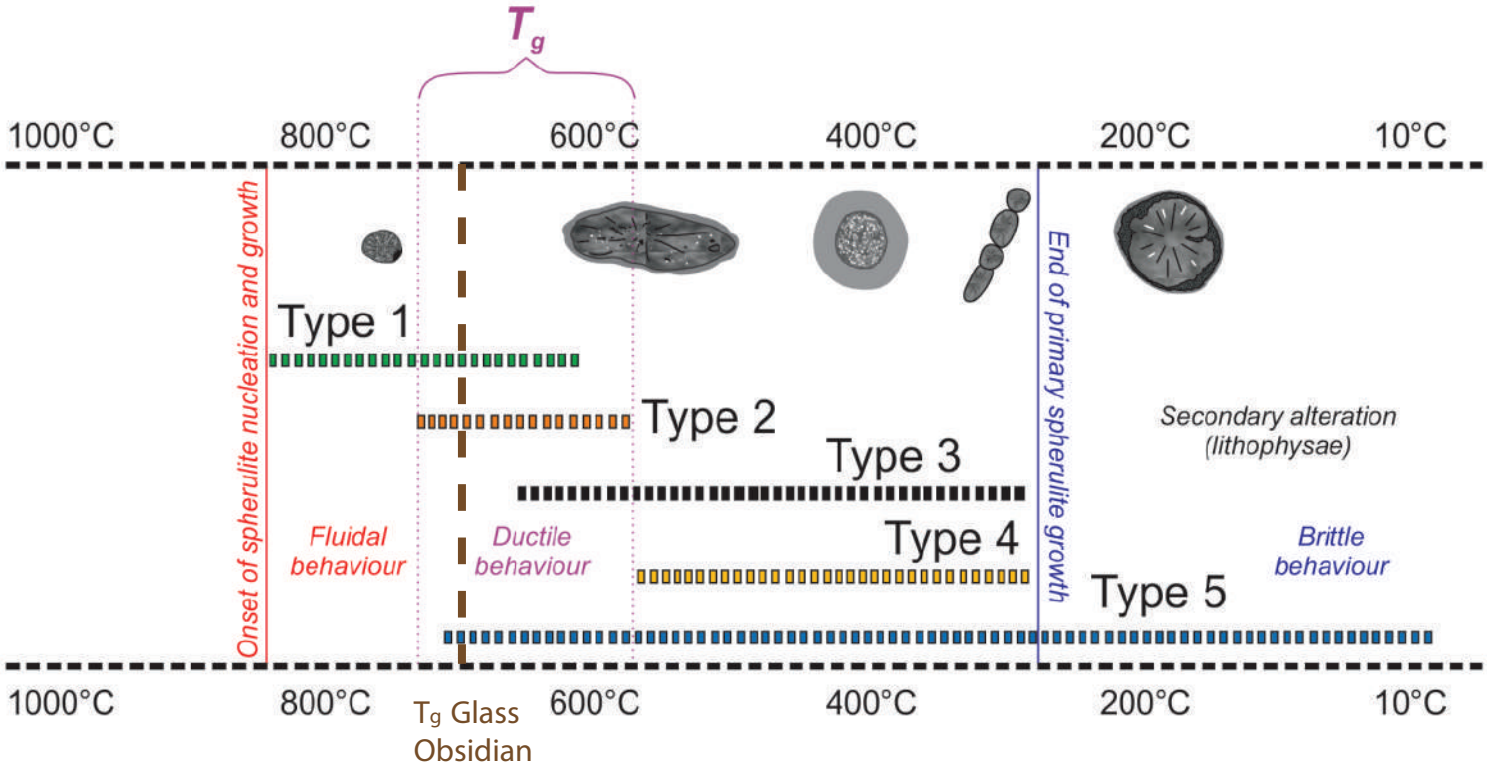
T_g
1000°C
800°C
600°C
400°C
200°C
10°C
Onset of spherulite nucleation and growth
Type 1
Type 2
Type 3
Type 4
Type 5
End of primary spherulite growth
Secondary alteration
(lithophysae)
Fluidal
behaviour
Ductile
behaviour
Brittle
behaviour
1000°C
800°C
Tg Glass
Obsidian
600°C
400°C
200°C
10°C

Figure 5. (a) Spherulite bearing sample 05-RR05 used for STEM experiments. (b) Lithic encased in sample 05-RR05 contains small obsidian fragments, compacted pumice, and an mm-sized sanidine feldspar crystal.

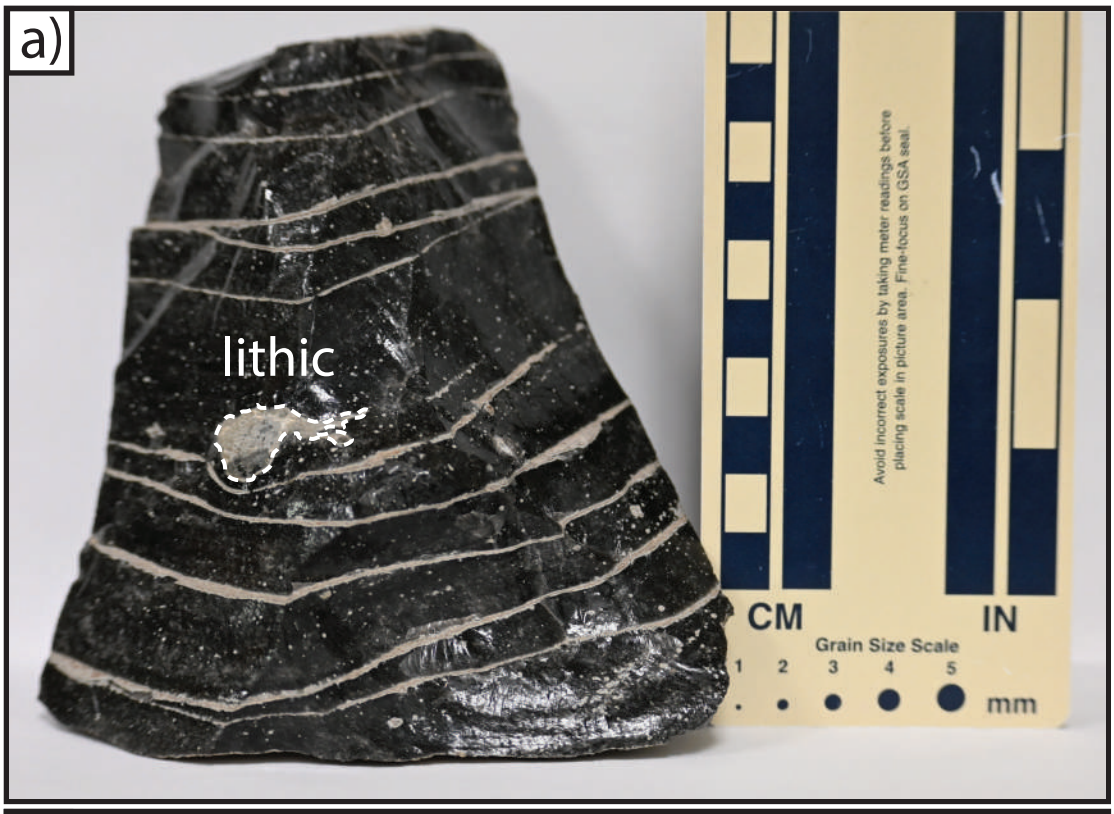
a)
lithic
Avoid incorrect exposures by taking meter readings before placing scale in picture area. Fine-focus on GSA seal.
CM
IN
Grain Size Scale
1 2 3 4 5
mm

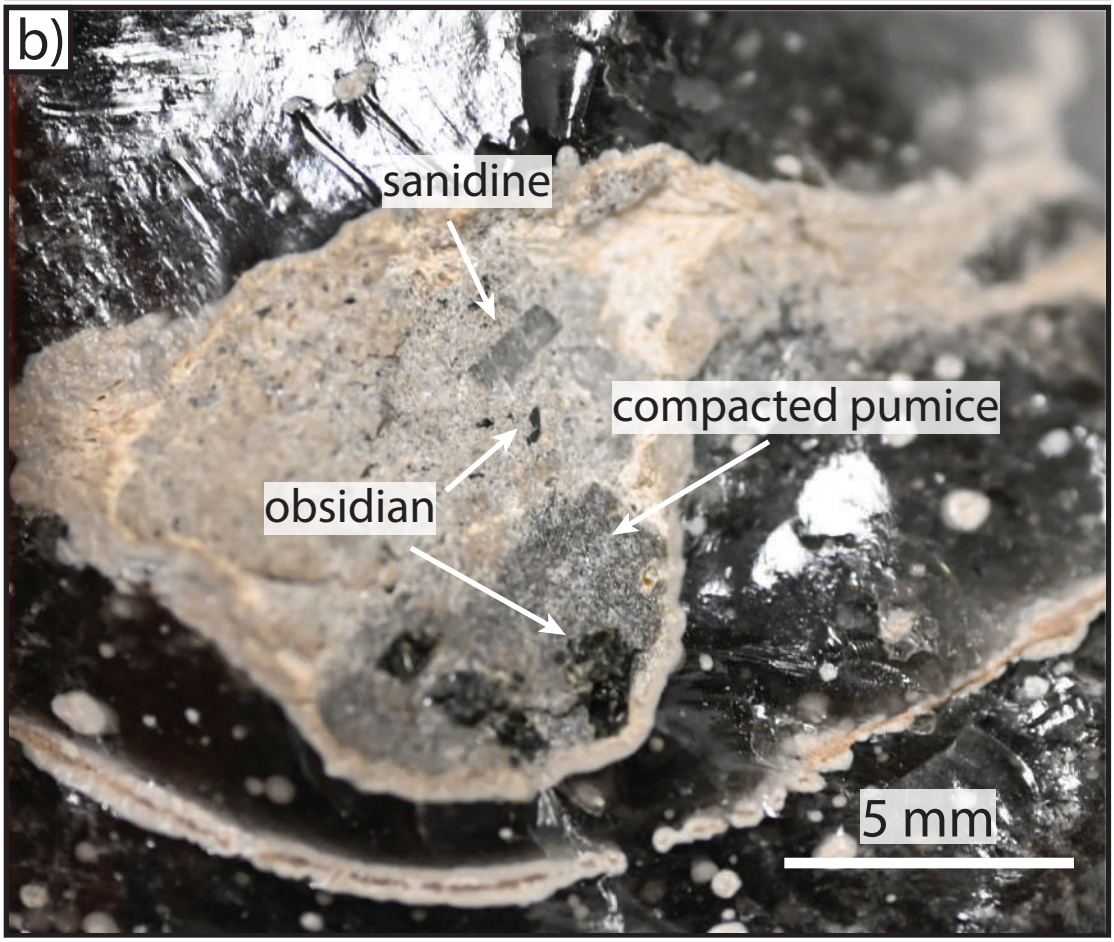
b)
sanidine
compacted pumice
obsidian
5 mm

Figure 6. (a) Front and (b) backside side of glassy spherulite bearing sample 09-RR06 collected from stop six and used for heating experiments.


a)
AR-12R066152
Avoid incorrect exposures by taking meter readings before placing scale in picture area. Fine-focus on GSA seal.
CM
IN
Grain Size Scale
1 2 3 4 5
mm


b)
Avoid incorrect exposures by taking meter readings before placing scale in picture area. Fine-focus on GSA seal.
CM
IN
Grain Size Scale
1 2 3 4 5
mm

Figure 7. (a) Glassy sample 12-RR08 collected from stop eight and used for STEM experiments. (b) Sample 13-RR10 with embedded lithic collected from stop ten and used for heating experiments.

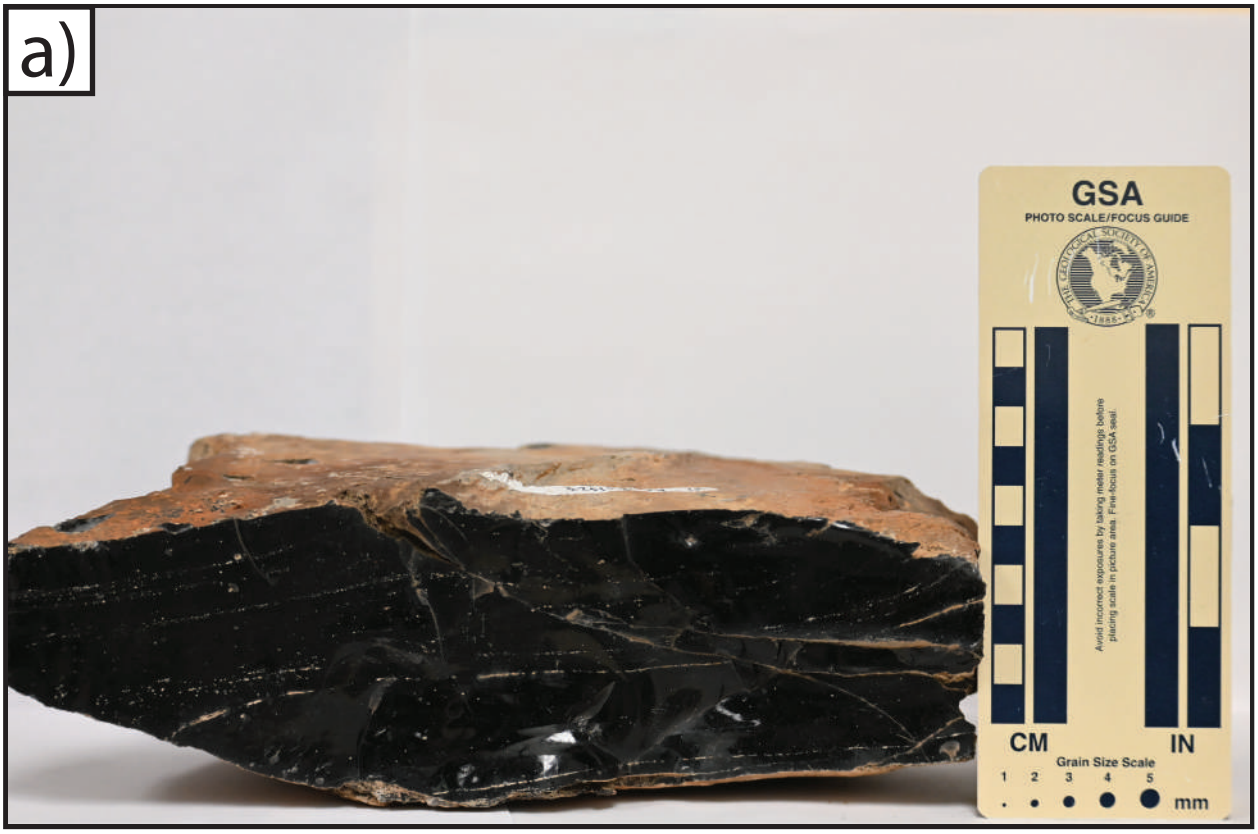
a)
GSA
PHOTO SCALE/FOCUS GUIDE
CM
IN
Grain Size Scale
1 2 3 4 5
mm

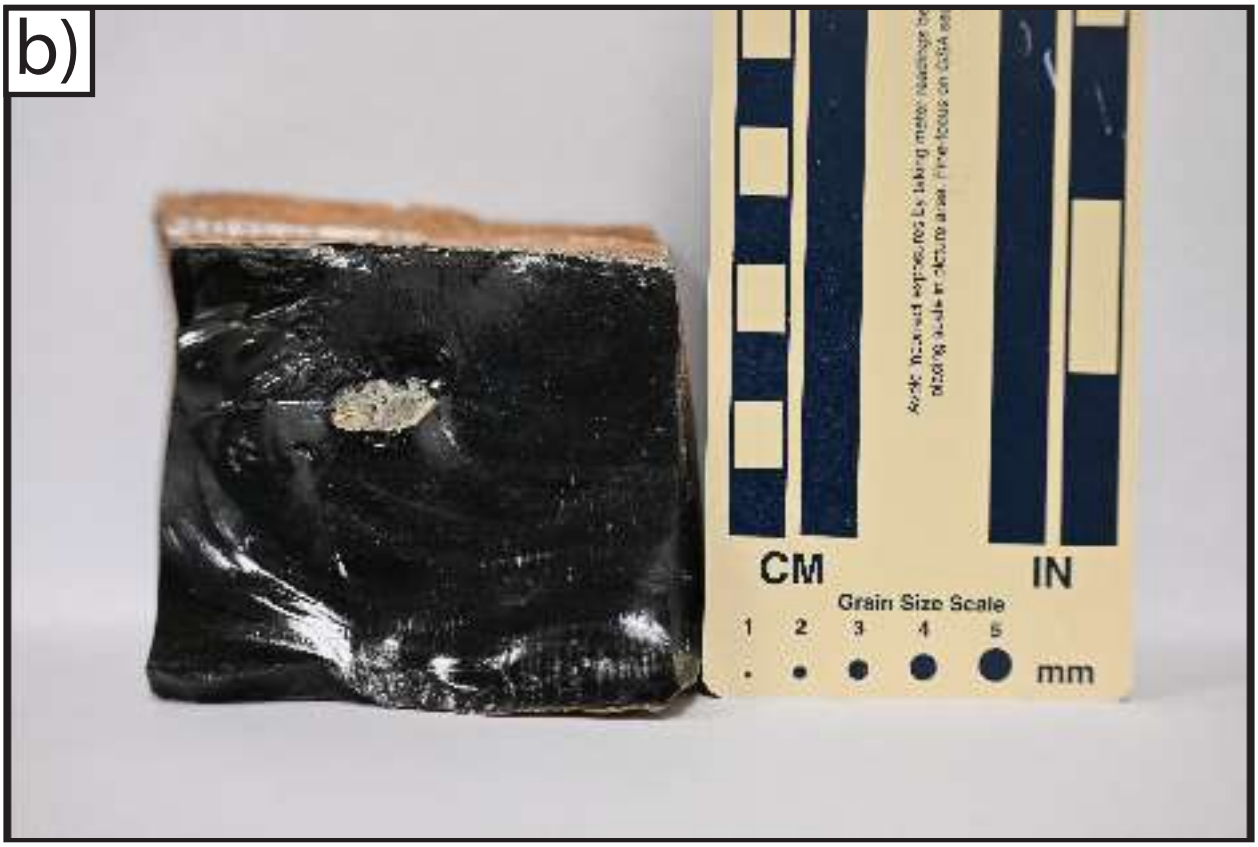
b)
CM
IN
Grain Size Scale
1 2 3 4 5
mm

Figure 8. STEM-based EDS spot analysis of sites 1 and 3 seen in secondary electron (SE) mode. (a) Site 1 shows collapsed vesicle area seen in Fig. 29b. (b) Site 3 (also reported in Fig. 29d) shows plagioclase seen in Fig. 30c. "Spectrum #" refers to numbered spot analysis via EDS using the Aztec software (Oxford Instruments).


a)
Spectrum 2
Spectrum 4
Spectrum 5
Spectrum 1
Spectrum 3
50nm

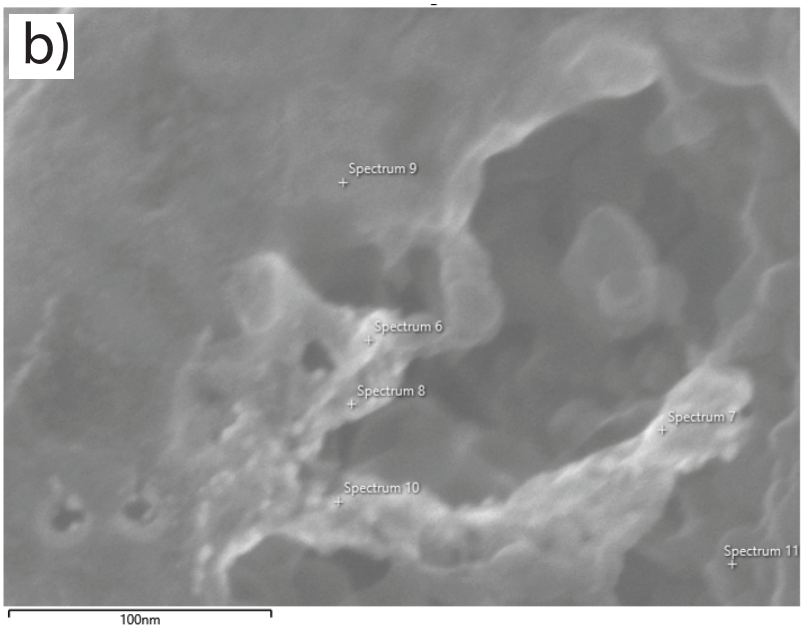
b)
Spectrum 9
Spectrum 6
Spectrum 8
Spectrum 7
Spectrum 10
Spectrum 11
100nm

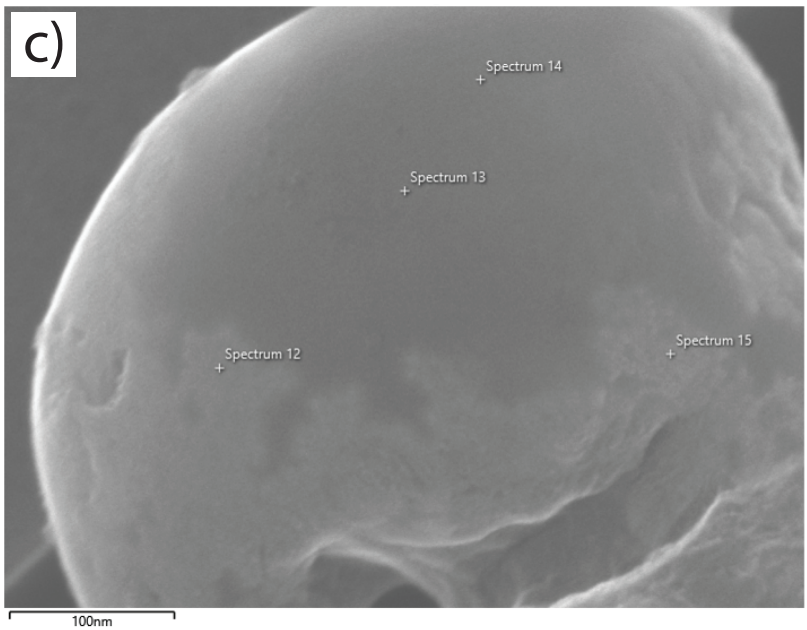
c)
Spectrum 14
Spectrum 13
Spectrum 12
Spectrum 15
100nm

Figure 9. Protocol of cutting the experimental conduits after the heating experiments to expose the run product for analytical investigation. 1. The extruded material and top portion of the granite jacket are decapitated with a ~6 mm gap. 2. The margin of the conduit is cut. 3. The center of the conduit is cut slightly off center. The remaining piece has the center of the conduit on one side and the margin on the other (bottom right). 4. Foamed extruded obsidian is cut to allow the bottom face to be laid flat for microscope viewing.

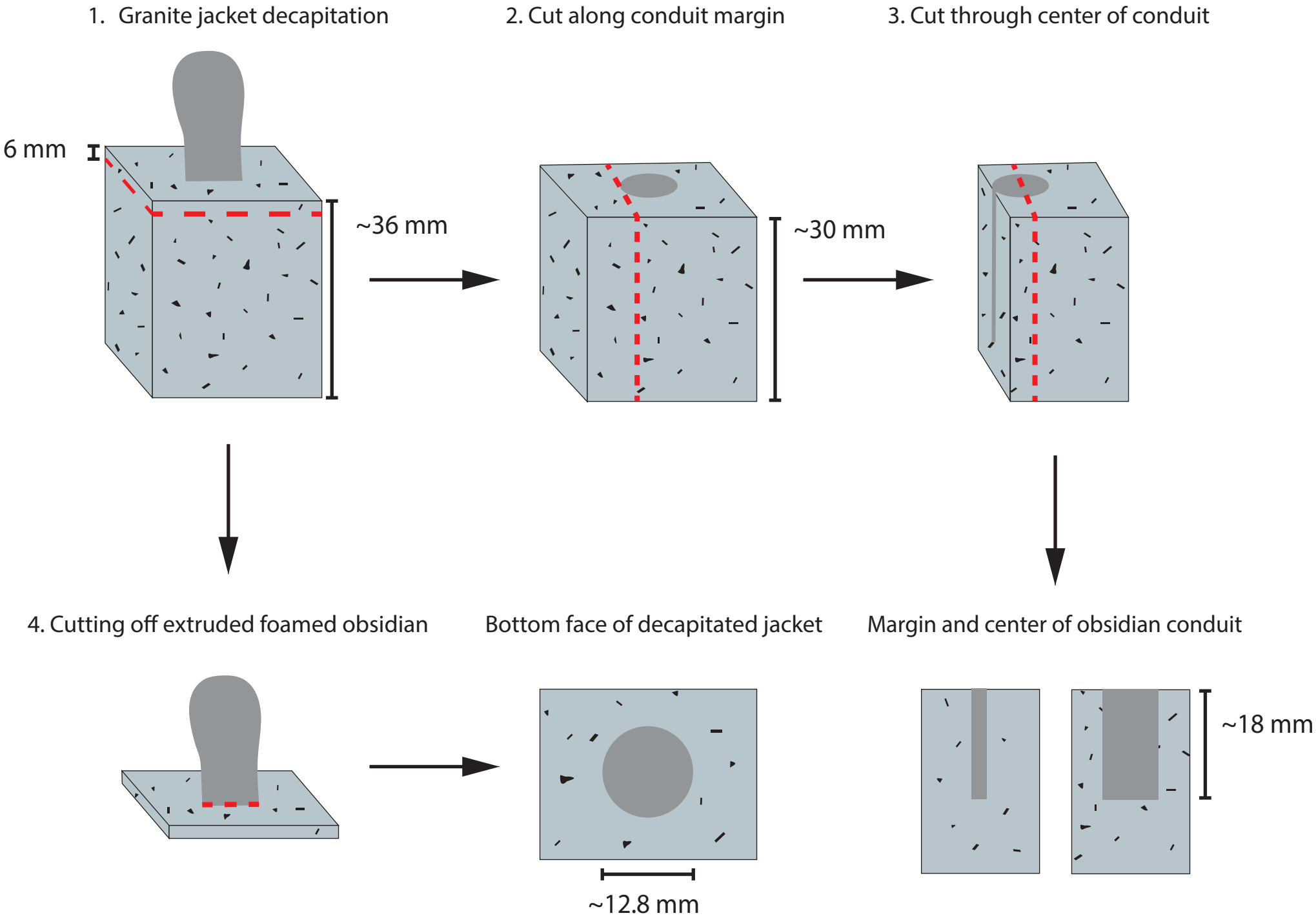
1. Granite jacket decapitation
2. Cut along conduit margin
3. Cut through center of conduit
6 mm
~36 mm
~30 mm
4. Cutting off extruded foamed obsidian
Bottom face of decapitated jacket
Margin and center of obsidian conduit
~12.8 mm
~18 mm

Figure 10. Geologic sketch map of the study area of Lipari Island adapted from Pistolesi et al. (2021). Numbered white circles indicate sampling sites and outcrop locations.

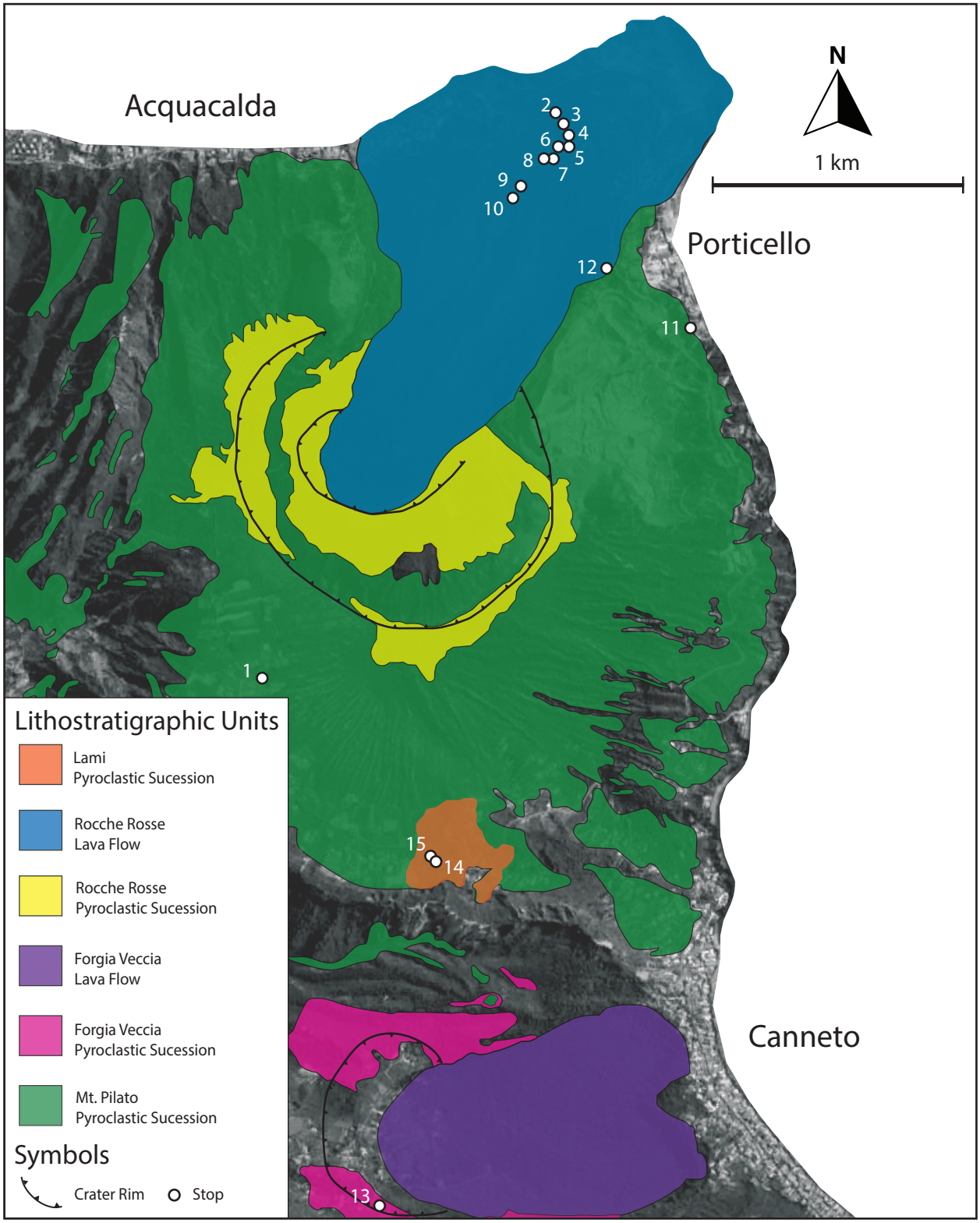
Acquacalda
Porticello
Canneto
N
1 km
1
2
3
4
5
6
7
8
9
10
11
12
13
14
15
Lithostratigraphic Units
Lami
Pyroclastic Sucession
Rocche Rosse
Lava Flow
Rocche Rosse
Pyroclastic Sucession
Forgia Veccia
Lava Flow
Forgia Veccia
Pyroclastic Sucession
Mt. Pilato
Pyroclastic Sucession
Symbols
Crater Rim
Stop

Figure 11. Site 1 located at the highest elevation of Mt. Pilato fallout deposits. Layers shift between cast and matrix-supported with obsidian and xenolith fragments scattered throughout the outcrop. The bottom of this outcrop is covered by eroded ash.

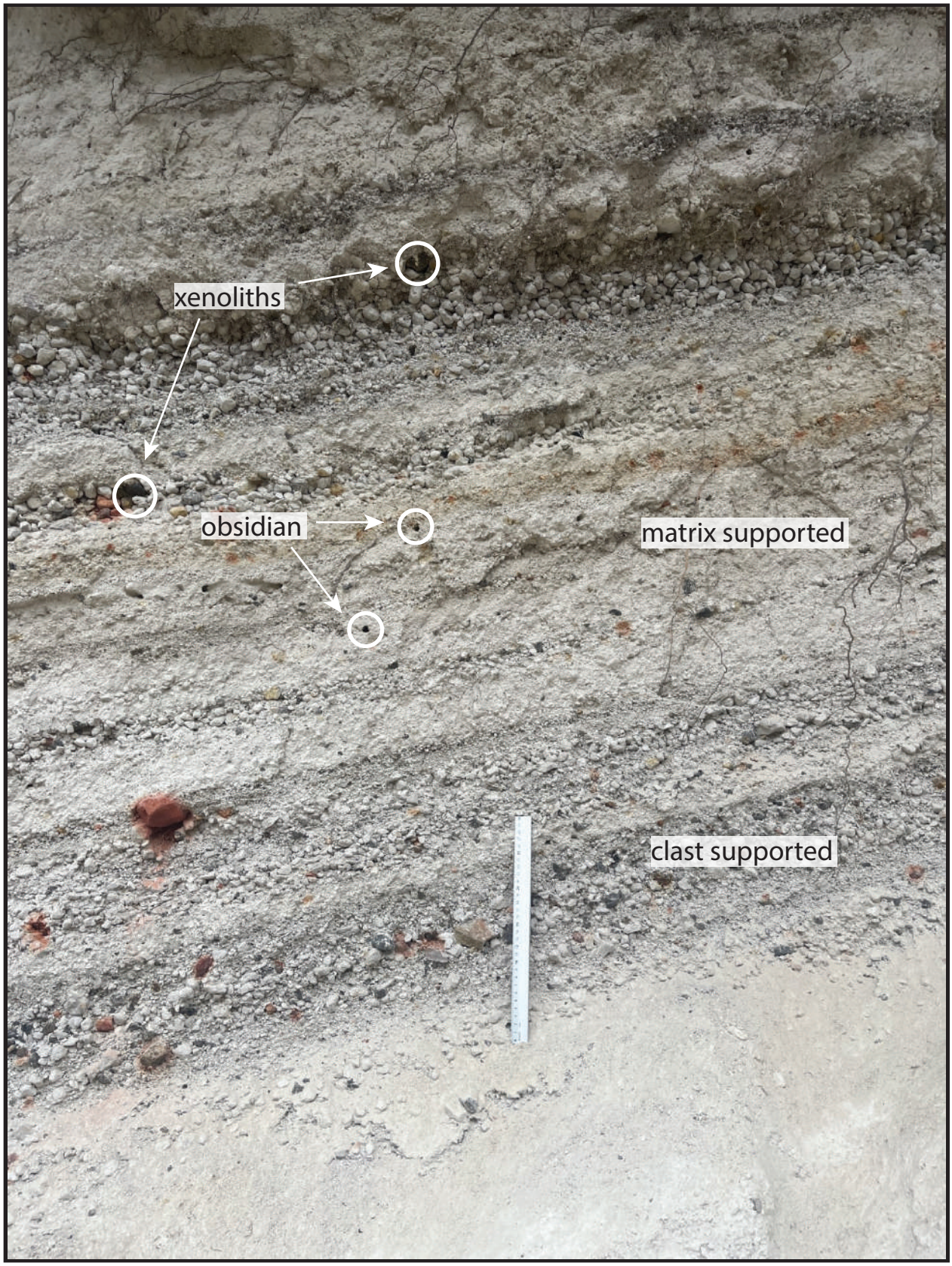
xenoliths
obsidian
matrix supported
clast supported

Figure 12. Site 11 located at the lowest elevation of Mt. Pilato fallout deposits. (a) View of the outcrop from the Naples-Lipari ferryapproaching the east side of Lipari Island. (b) The entirety of the outcrop from along the edge of the Porticello Quarry. (c) Weathered exposure of obsidian at the base of the outcrop.

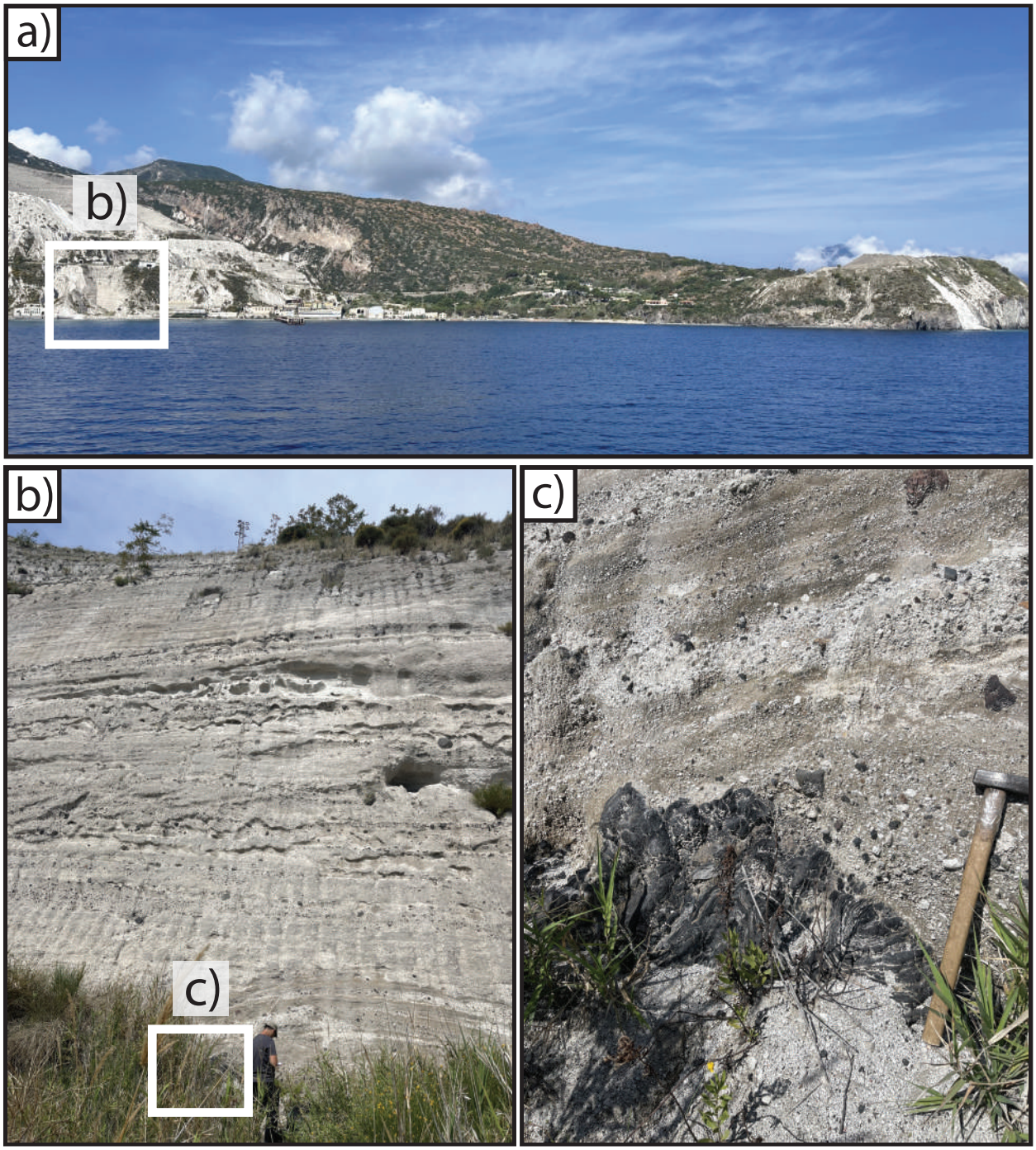
a)
b)
b)
c)
c)

Figure 13. View of the lithological contact between Mt Pilato and Rocche Rosse seen from the shoreline. To the leftof the contact is the Porticello Quarry. The bridge located behind the building seen in the center of the photo is the location of site 12.

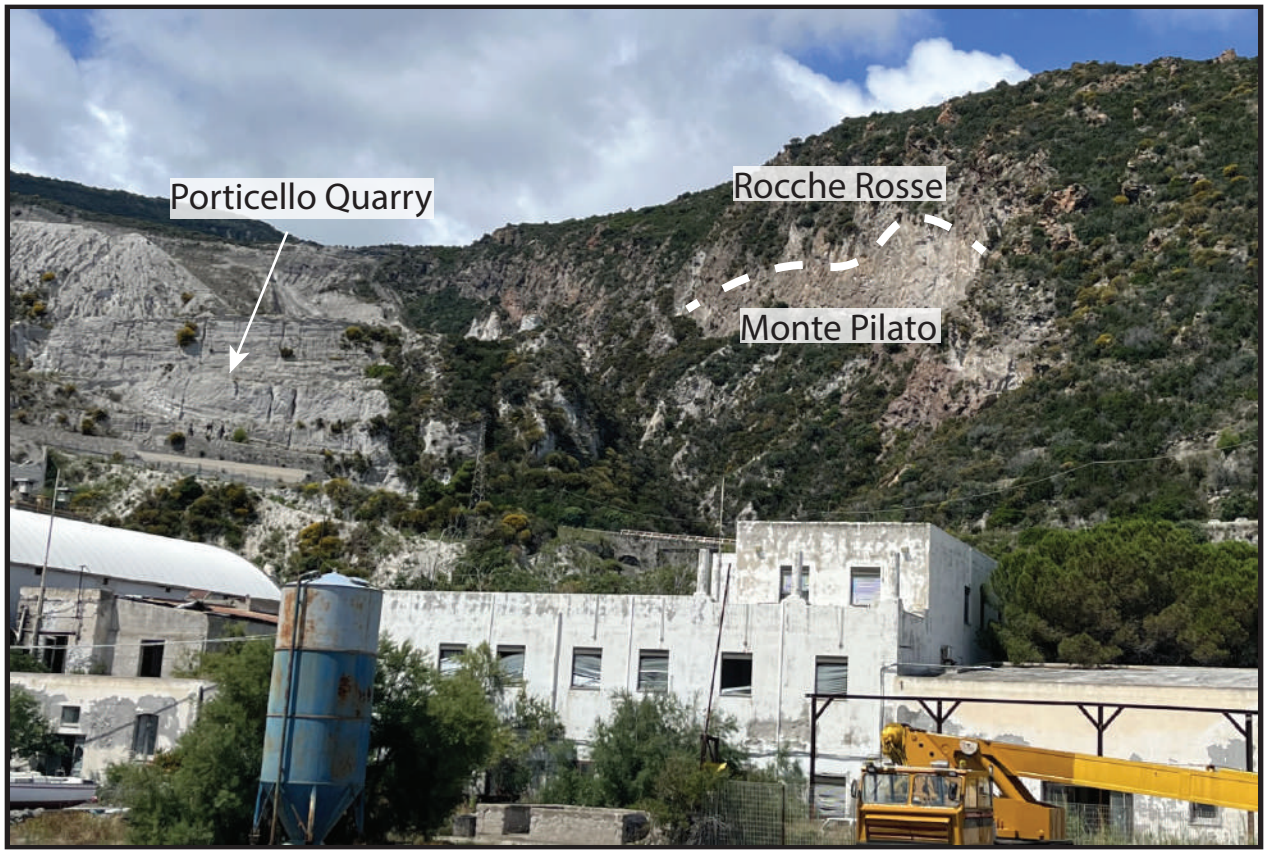
Porticello Quarry
Rocche Rosse
Monte Pilato

Figure 14. Different portions of Rocche Rosse lava flow outcrops seen at sites 6 and 8. (a) Eroded cross-section of obsidian outcrop showing sub-horizontal layering produced by lava flow during emplacement. (b) Tension cracks perpendicular to deposit layering generated during brittle flow of the lava during cooling. (c) Alternating welded vesicle-free layers and vesicle-rich glass within a single hand rock specimen.

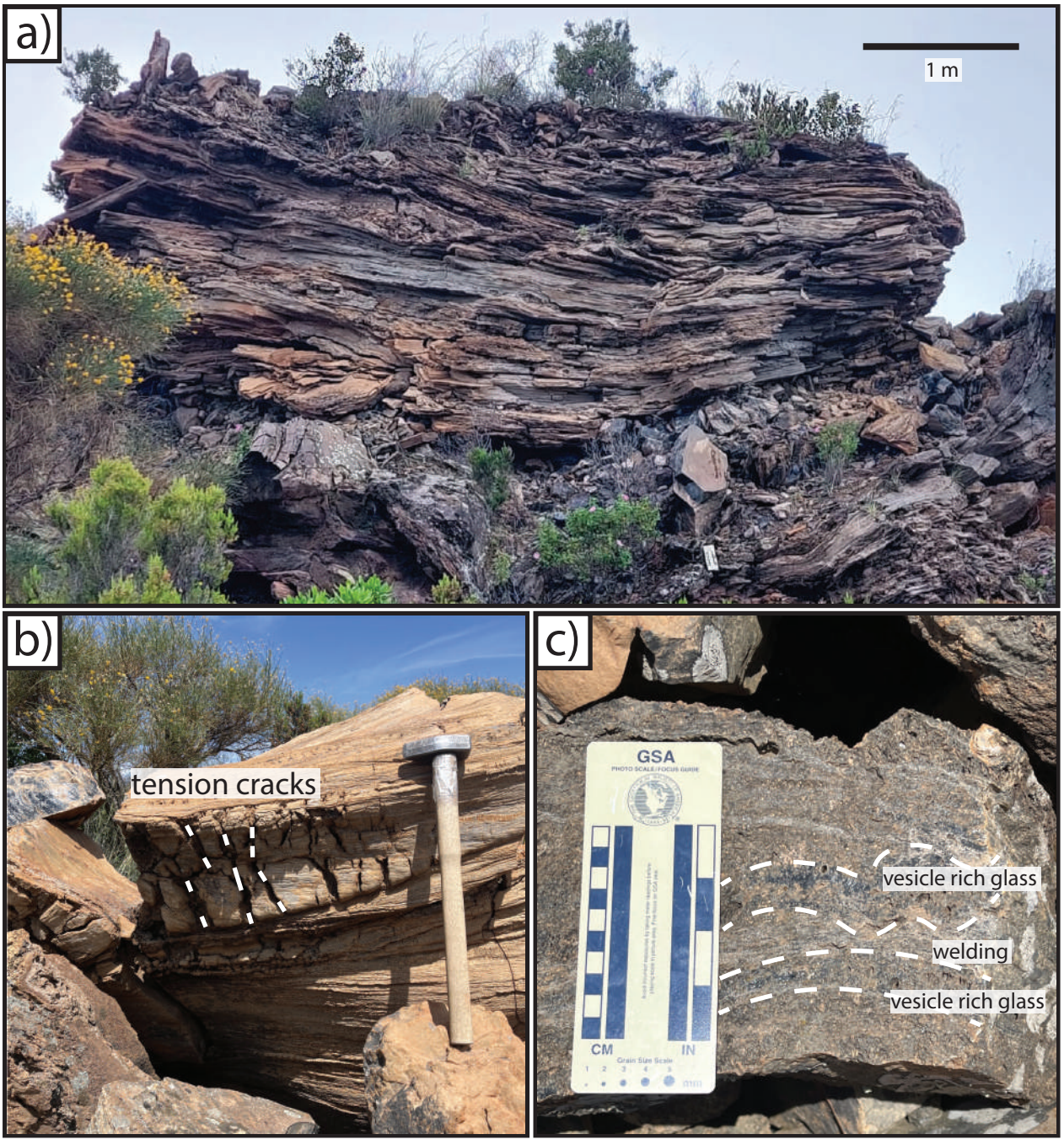
a)
1 m
b)
tension cracks
c)
GSA
CM
IN
vesicle rich glass
welding
vesicle rich glass

Figure 15. Eroded vertical sections of layered lava flow deposit of Rocche Rosse seen at sites 7 and 9: (a) squeeze out structure, and (b) pumiceous erosional remnant showing folded layers (highlighted by dashed white lines).

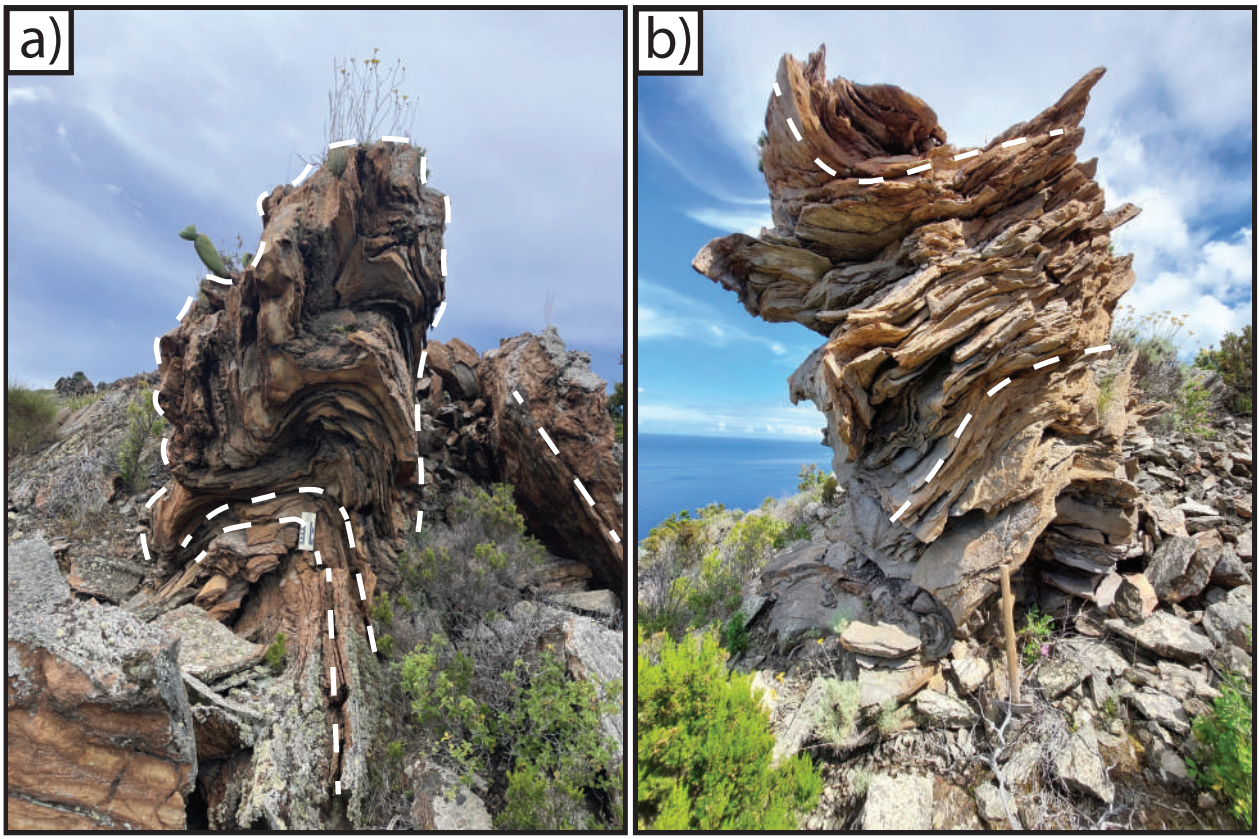
a)
b)

Figure 16. Site 10 is the highest point reached on the Rocche Rosse lava flow deposit during the field campaign of this study. (a) Outcrop showing the glassiest samples collected for this research. (b) View of the exact location where sample 13-RR10 was collected and then used for the heating experiments.

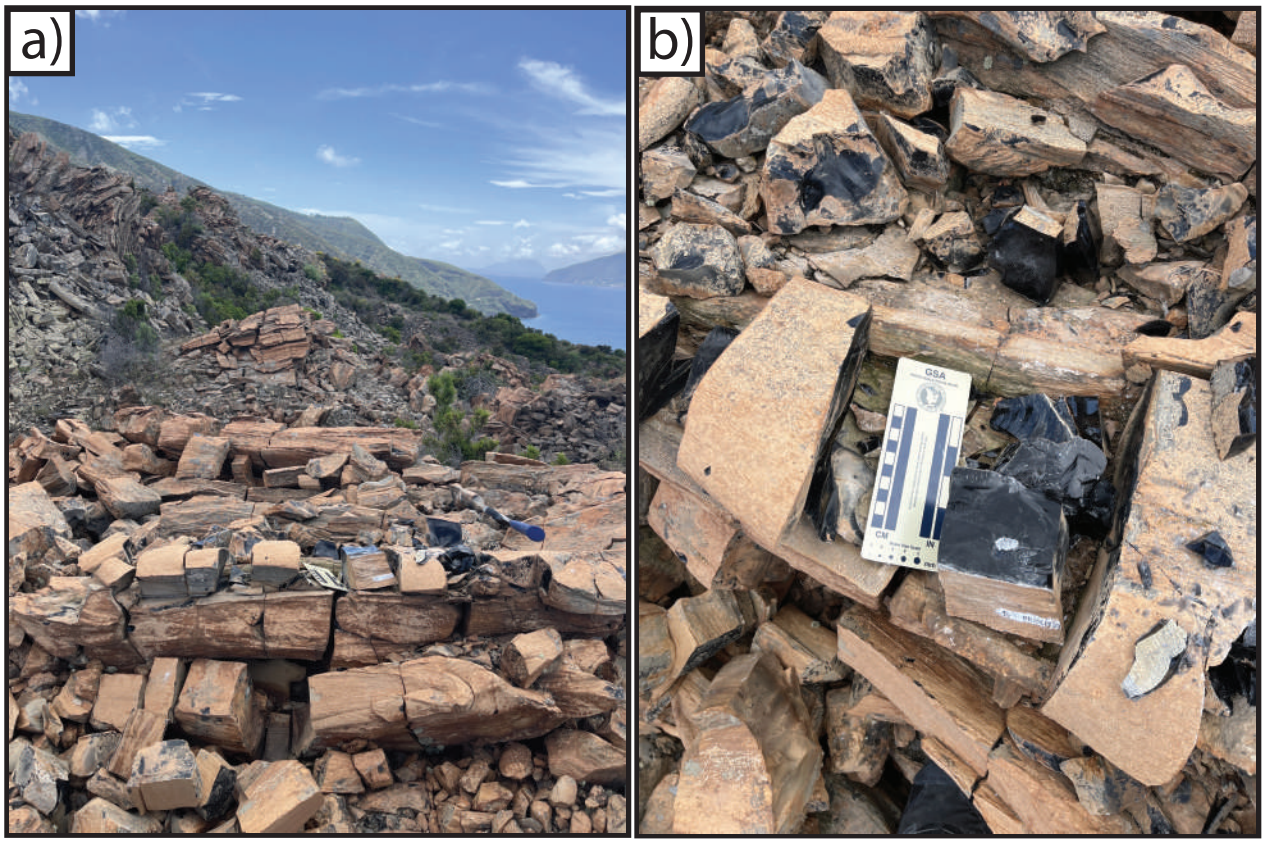
a)
b)
GSA
CM

Figure 17. (a-d) Plain light images of representative Rocche Rosse obsidian thin section. (f-j) Cross-polarized images of the same sample portions showing phenocrysts (f) and spherulites (g-j). (a) and (f) contain albite with orthopyroxenes and quartz sectorzoned in the albite.

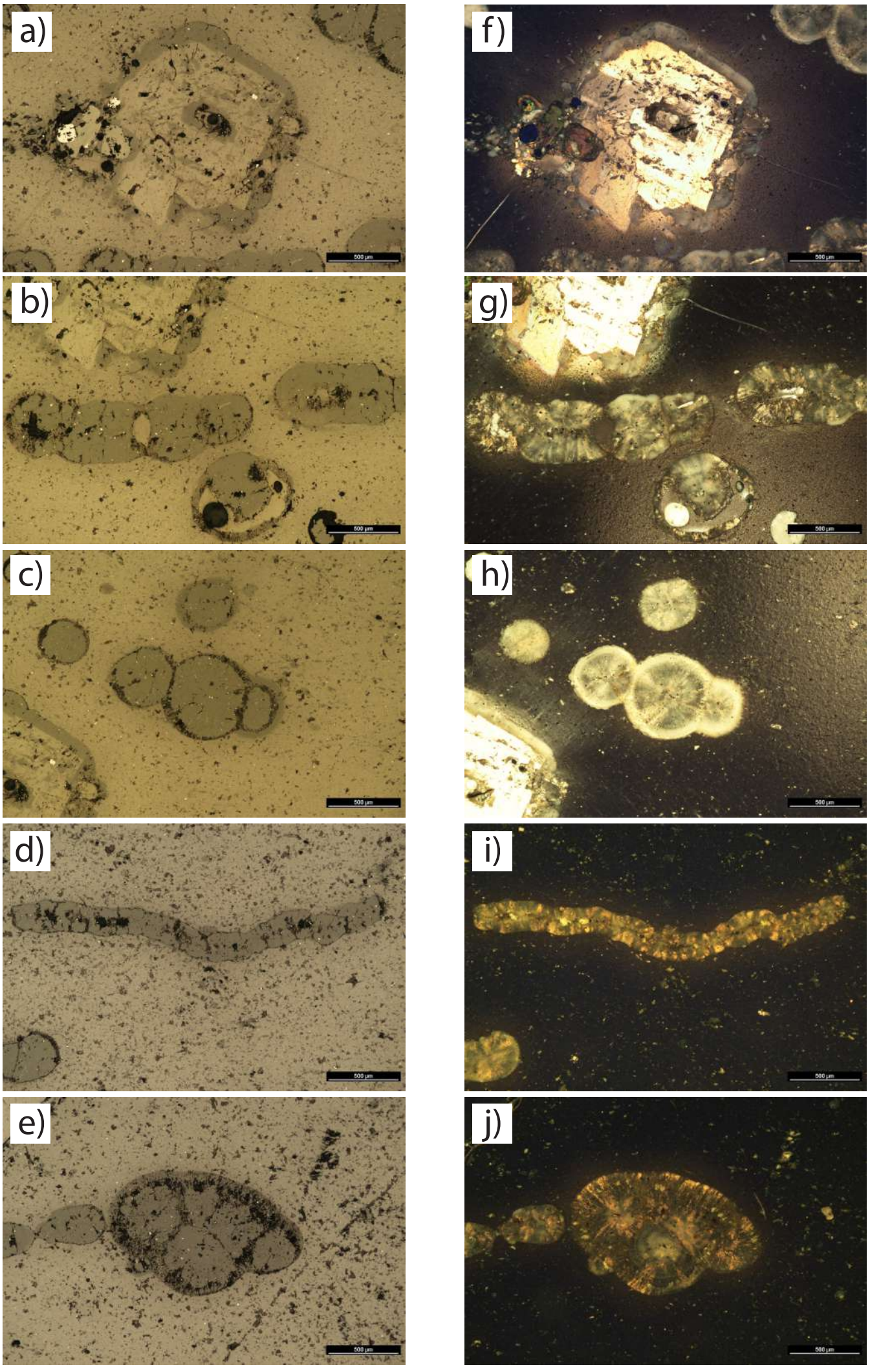
a)
f)
b)
g)
c)
h)
d)
i)
e)
j)

Figure 18. (a-d) Plain light images of representative Mount Pilato pumice thin section. (f-j) Cross-polarized images of Mount Pilato pumice showing highly stretched vesicles.


a)

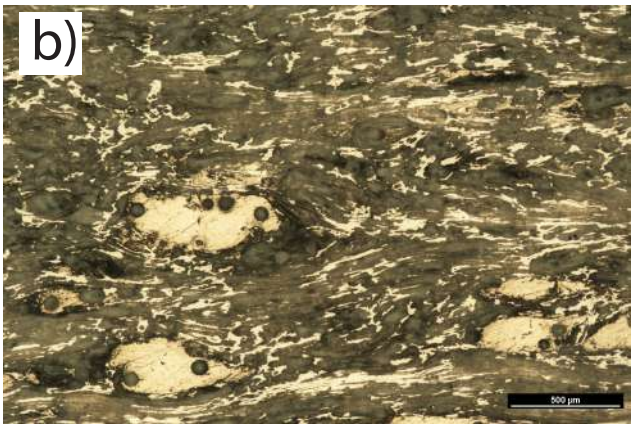
b)

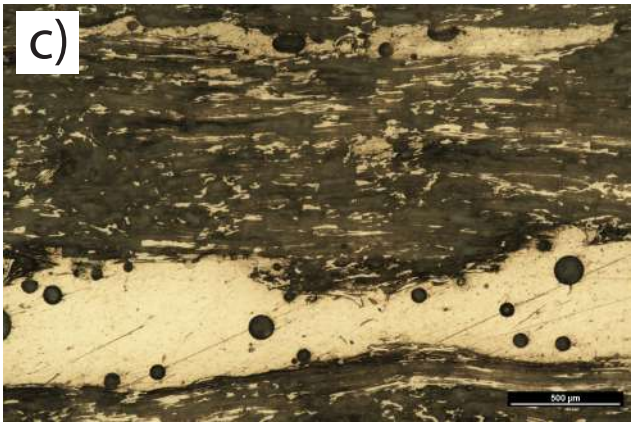
c)

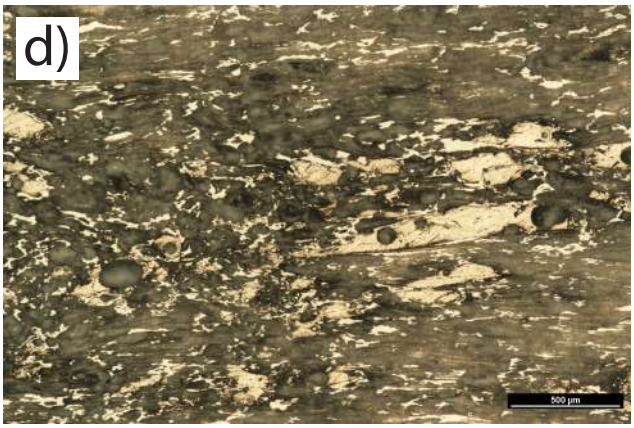
d)

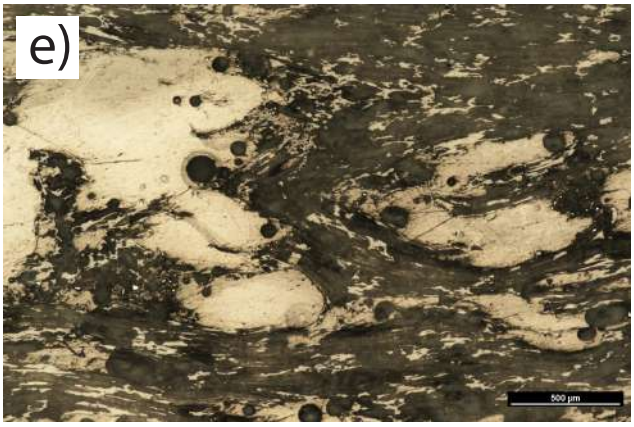
e)

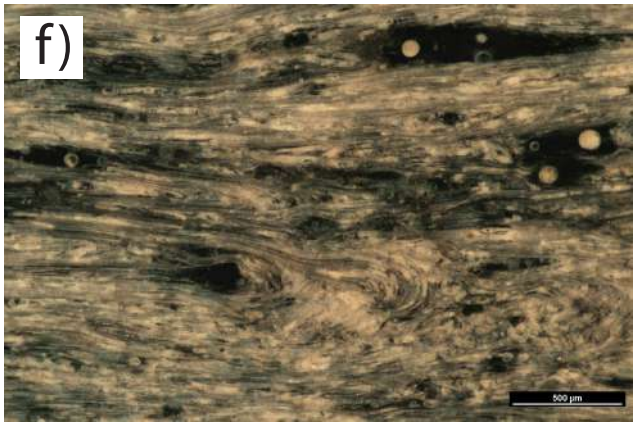
f)

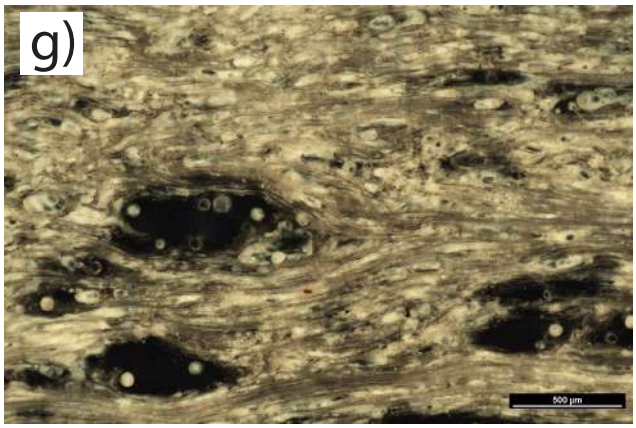
g)

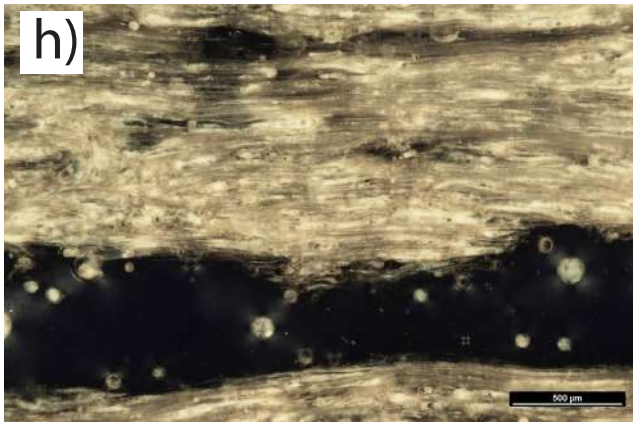
h)

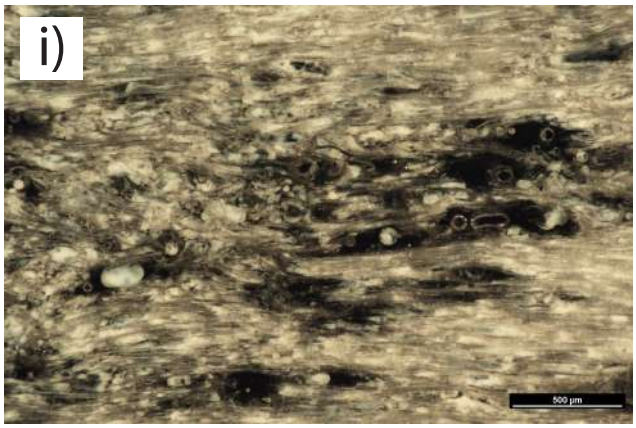
i)

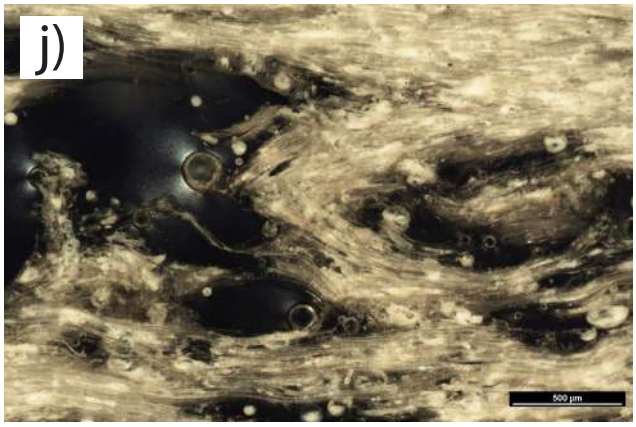
j)

Figure 19. First heating ramp applied to glass obsidian during differential scanning calorimeter (DSC) measurement. The plot shows the variation of specific heat capacity (cp) with temperature increase and the thermal location of the glass transition temperature (Tg). As explained by Webb (2021), the estimation of the Tg is based on the equivalent integrals of "equal area" method, which follows the fictive temperature approach of Tool (1946), Narayanaswamy (1971), and Moynihan et al. (1974; 1976).

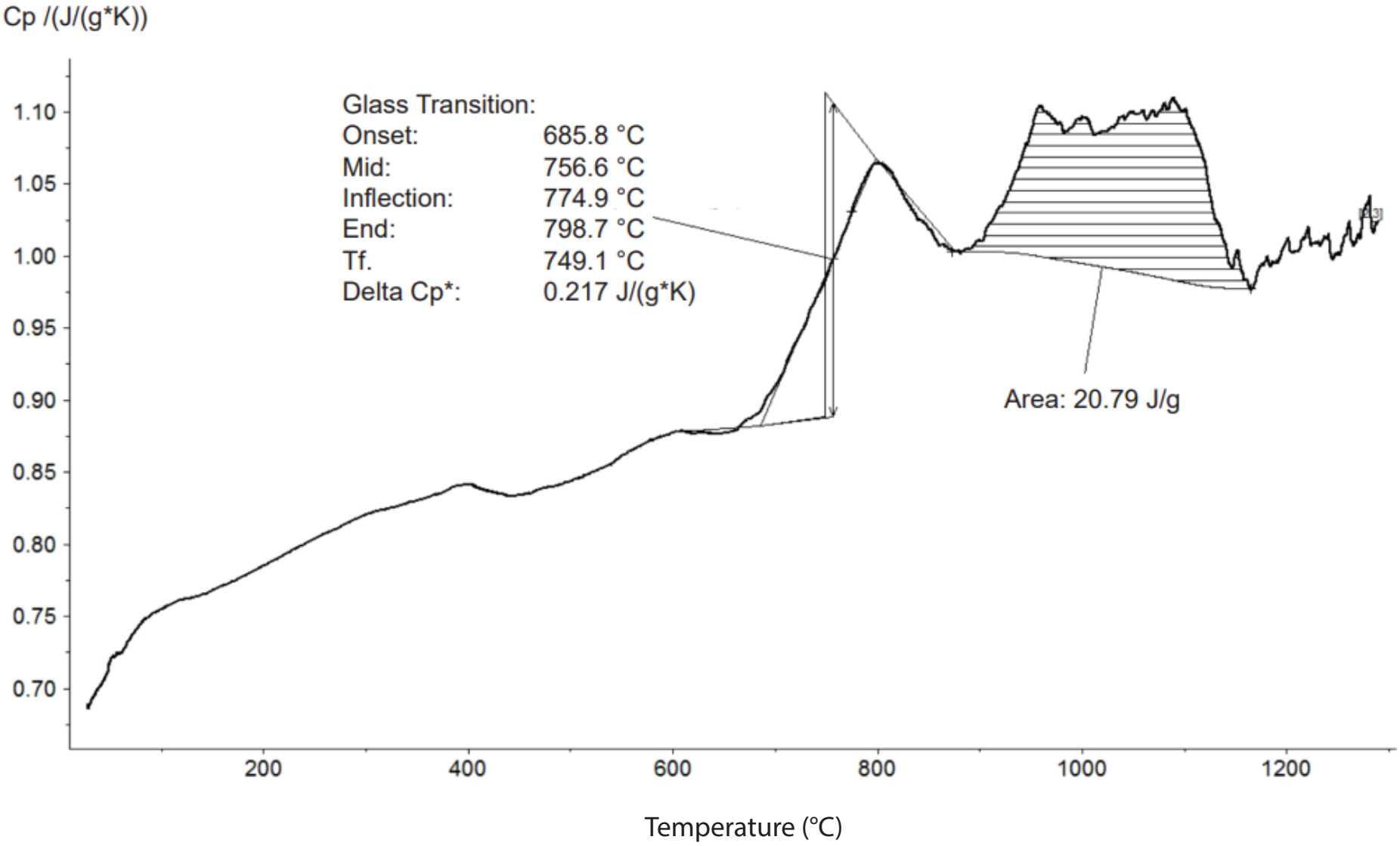
Cp /(J/(g*K))
Glass Transition:
Onset: 685.8 °C
Mid: 756.6 °C
Inflection: 774.9 °C
End: 798.7 °C
Tf. 749.1 °C
Delta Cp*: 0.217 J/(g*K)
Area: 20.79 J/g
1.10
1.05
1.00
0.95
0.90
0.85
0.80
0.75
0.70
200
400
600
800
1000
1200
Temperature (°C)

Figure 20. Reheating ramp applied to glass obsidian during differential scanning calorimeter (DSC) measurement. Details of the plots are the same as Fig. 19.

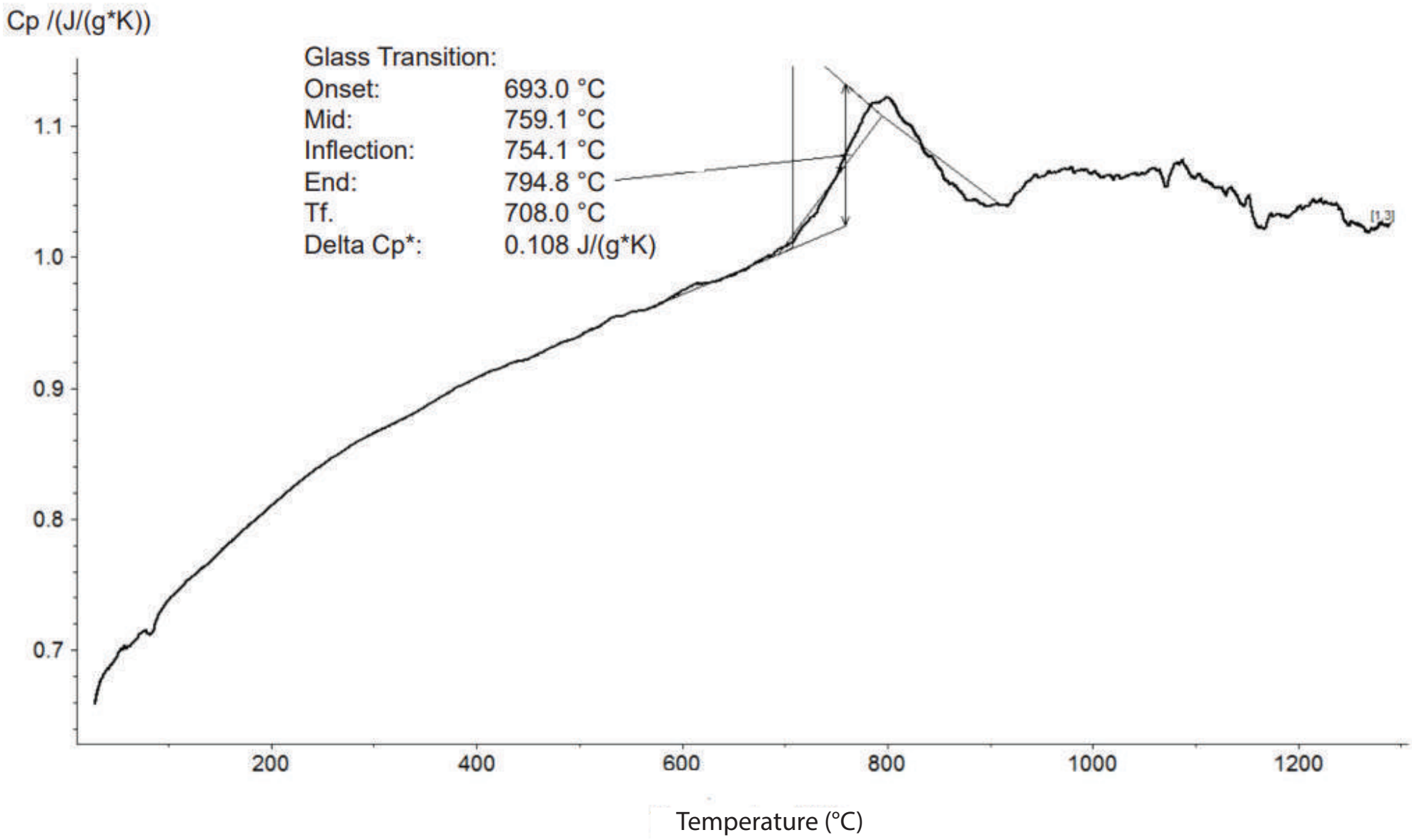
Cp /(J/(g*K))
Glass Transition:
Onset: 693.0 °C
Mid: 759.1 °C
Inflection: 754.1 °C
End: 794.8 °C
Tf. 708.0 °C
Delta Cp*: 0.108 J/(g*K)
1.1
1.0
0.9
0.8
0.7
200
400
600
800
1000
1200
Temperature (°C)

Figure 21. First heating ramp applied to spherulite bearing obsidian during differential scanning calorimeter (DSC) measurement. Details of the plots are the same as Fig. 19.

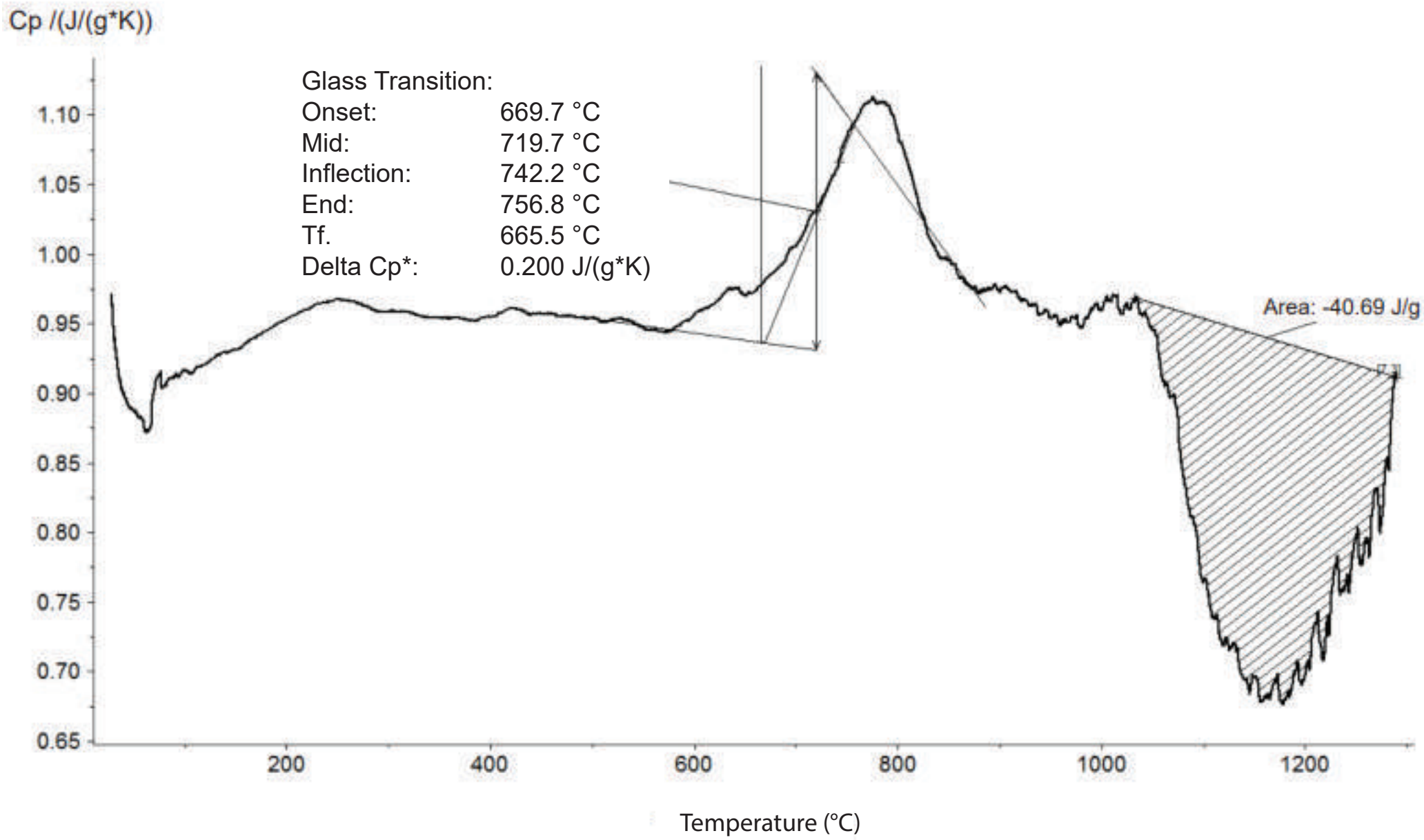
Cp /(J/(g*K))
Glass Transition:
Onset: 669.7 °C
Mid: 719.7 °C
Inflection: 742.2 °C
End: 756.8 °C
Tf. 665.5 °C
Delta Cp*: 0.200 J/(g*K)
Area: -40.69 J/g
1.10
1.05
1.00
0.95
0.90
0.85
0.80
0.75
0.70
0.65
200
400
600
800
1000
1200
Temperature (°C)

Figure 22. Reheating ramp applied to spherulite bearing obsidian during differential scanning calorimeter (DSC) measurement. Details of the plots are the same as Fig. 19.

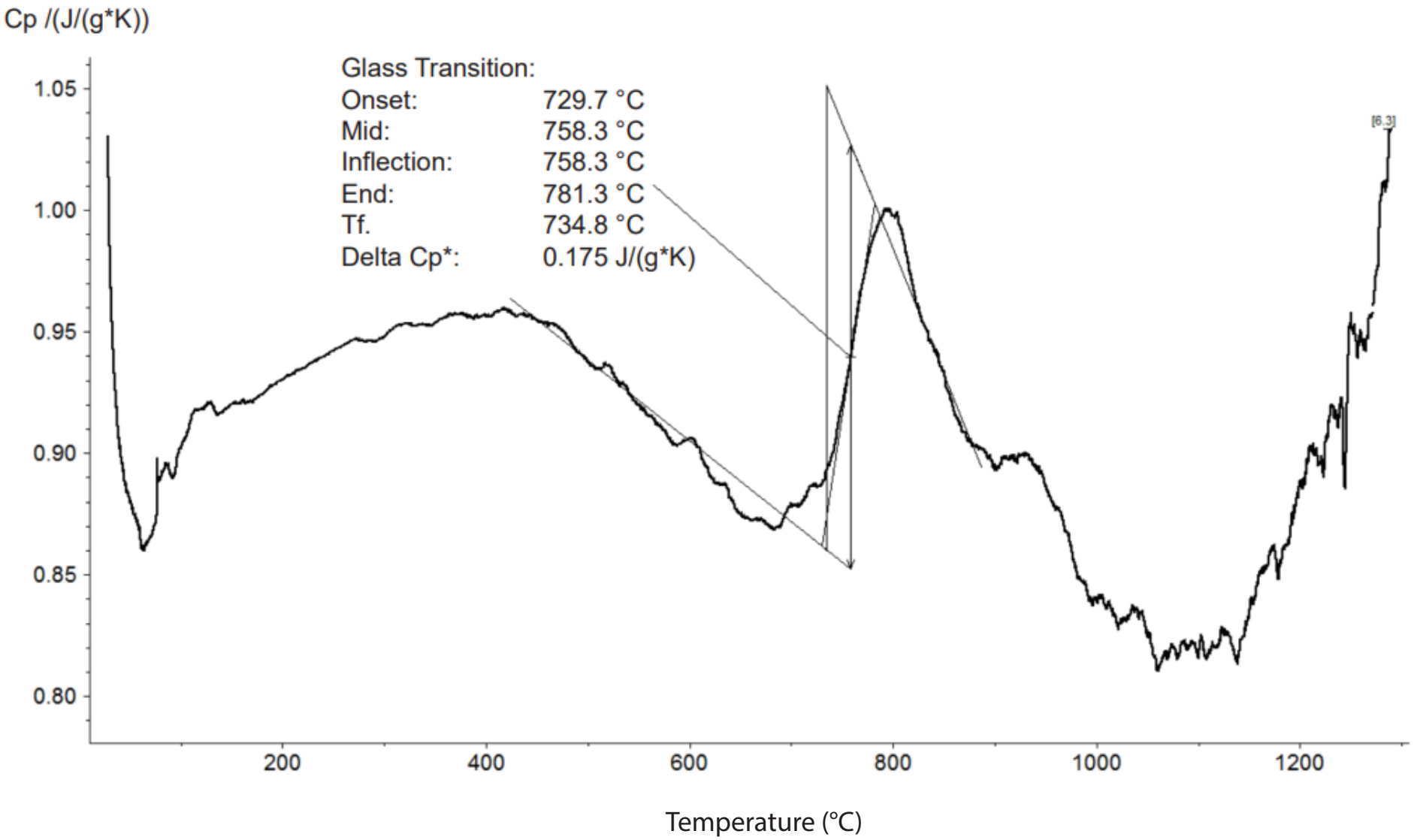
Cp /(J/(g*K))
Glass Transition:
Onset: 729.7 °C
Mid: 758.3 °C
Inflection: 758.3 °C
End: 781.3 °C
Tf. 734.8 °C
Delta Cp*: 0.175 J/(g*K)
[6.3]
1.05
1.00
0.95
0.90
0.85
0.80
200
400
600
800
1000
1200
Temperature (°C)

Figure 23. Vogel- Fulcher-Tammann (VFT) and Arrhenius viscosity fits for spherulite bearing and obsidian glass samples, respectively. See details in text.

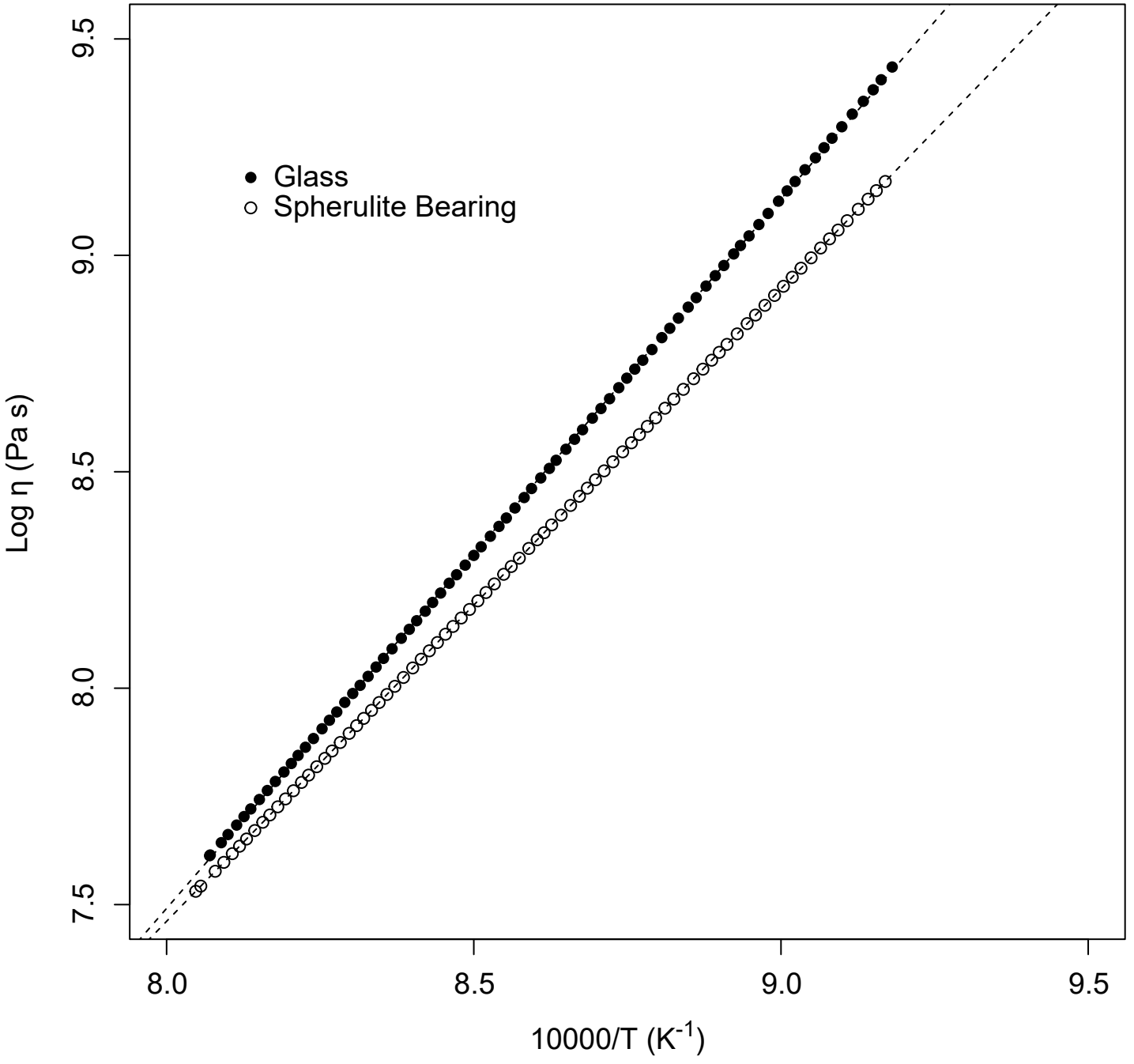
Glass
Spherulite Bearing
Log η (Pa s)
10000/T (K-1)
7.5
8.0
8.5
9.0
9.5

Figure 24. Extrapolated Vogel- Fulcher-Tammann (VFT) and Arrhenius viscosity fits for spherulite bearing and obsidian glass samples, respectively. See details in text.

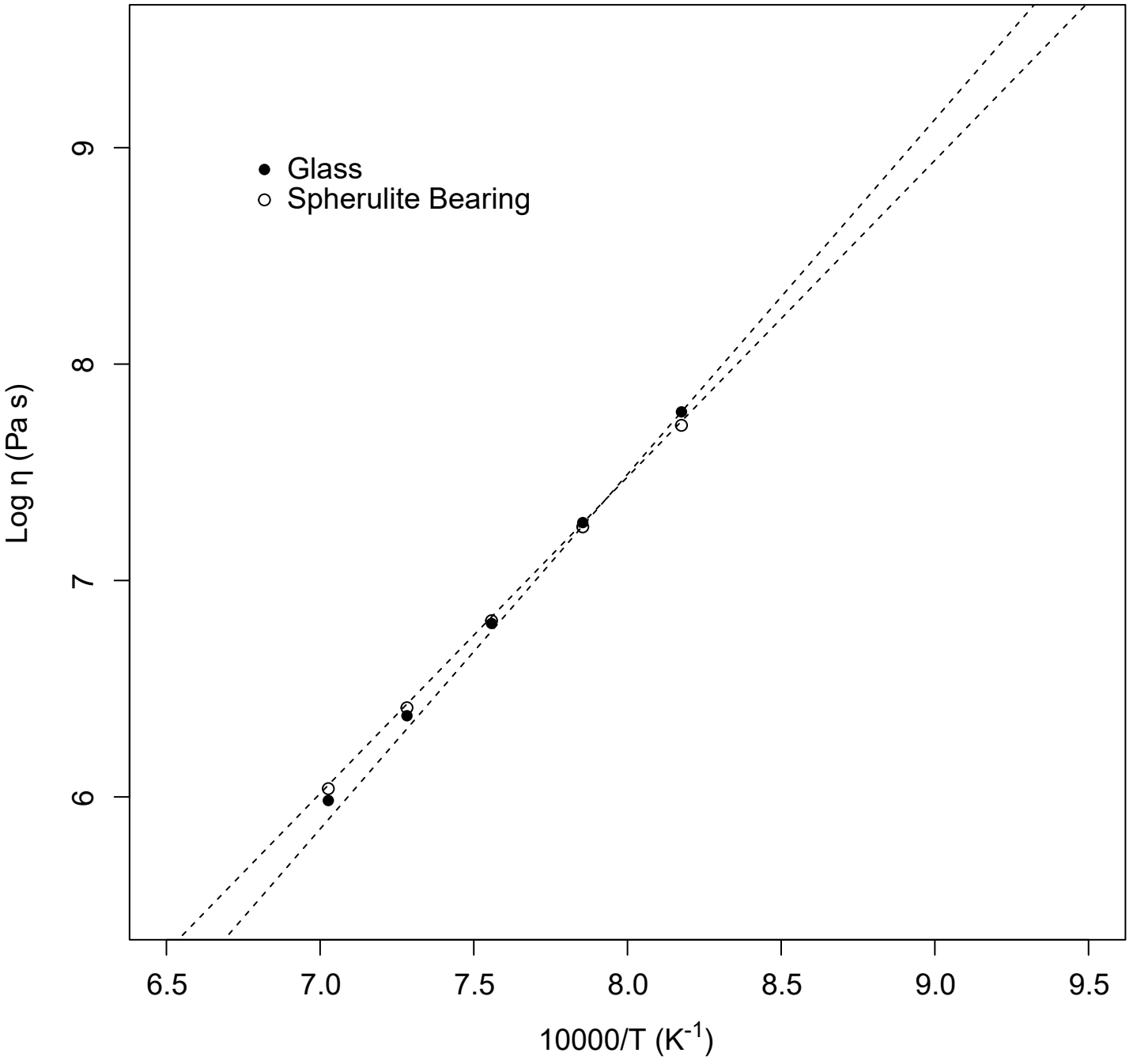
Glass
Spherulite Bearing
Log η (Pa s)
6
7
8
9
6.5
7.0
7.5
8.0
8.5
9.0
9.5
10000/T (K-1)

Figure 25. Sample height compression of spherulite bearing and obsidian glass specimens during heating in a parallel plate viscometer.

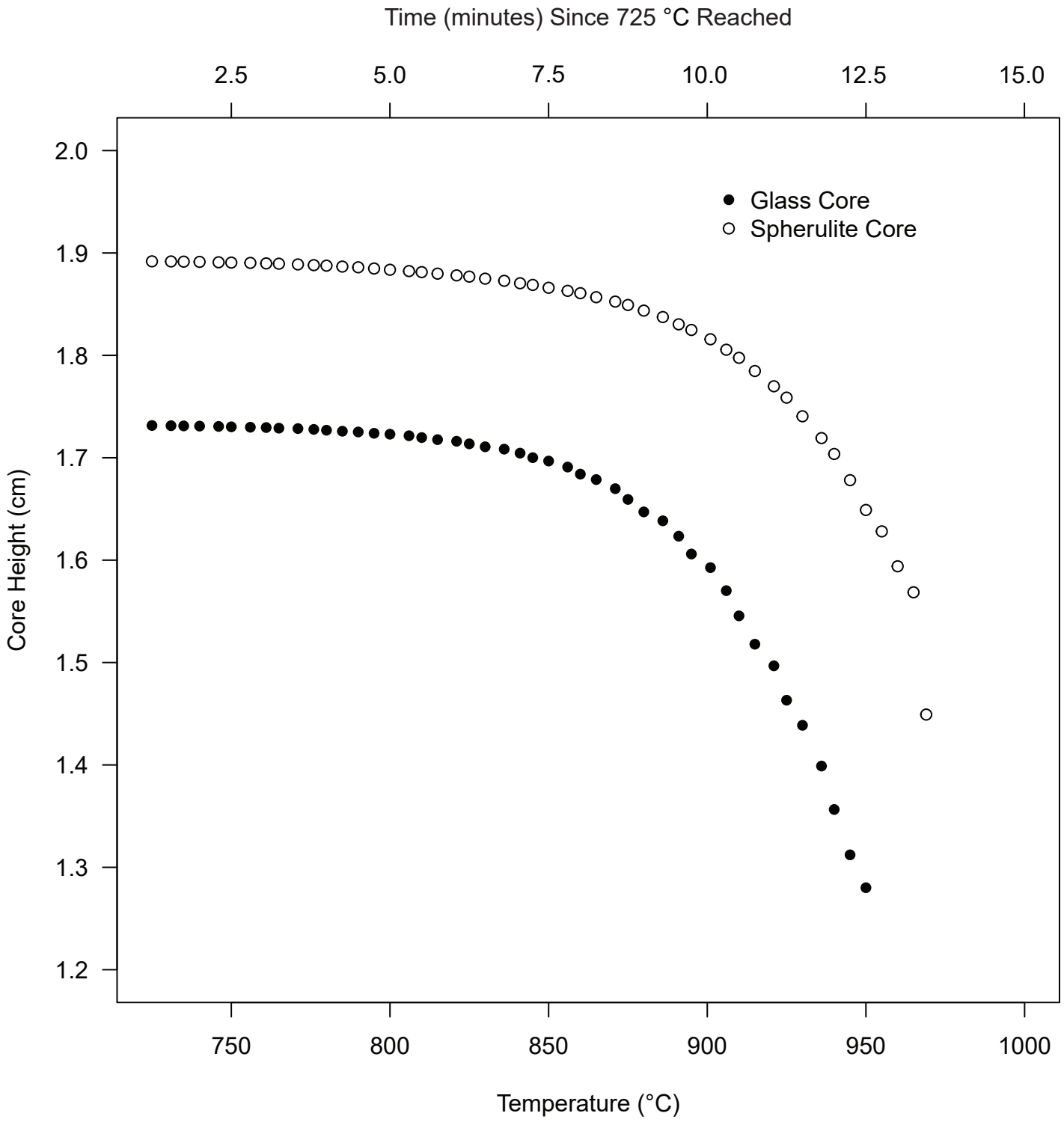
Time (minutes) Since 725 °C Reached
2.5
5.0
7.5
10.0
12.5
15.0
2.0
1.9
1.8
1.7
1.6
1.5
1.4
1.3
1.2
Core Height (cm)
Glass Core
Spherulite Core
750
800
850
900
950
1000
Temperature (°C)

Fig. 26. Viscosity data of glass and spherulite-bearing obsidian as a function of temperature based on the measurements via parallel plate viscometer.

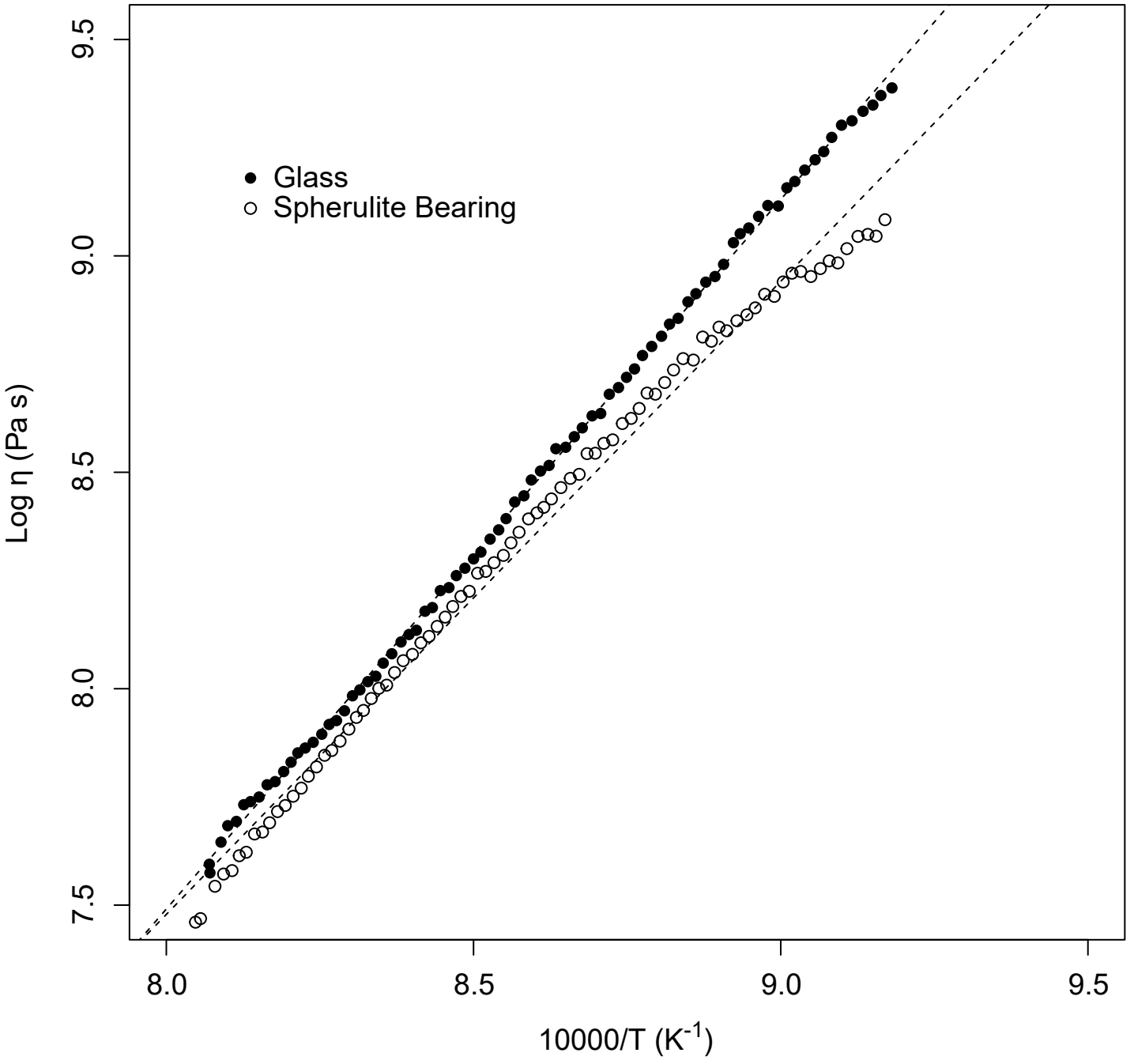
Glass
Spherulite Bearing
Log η (Pa s)
10000/T (K-1)
7.5
8.0
8.5
9.0
9.5

Figure 27. STEM-based SE images of glass powder grain from area 3. (a) The entire grain observed during heating with frame indication of image b. (b) Pre-existing pores in the powder grain at 500 °C, below Tg. (c) Pore growth of the same location occurring at 700 °C.

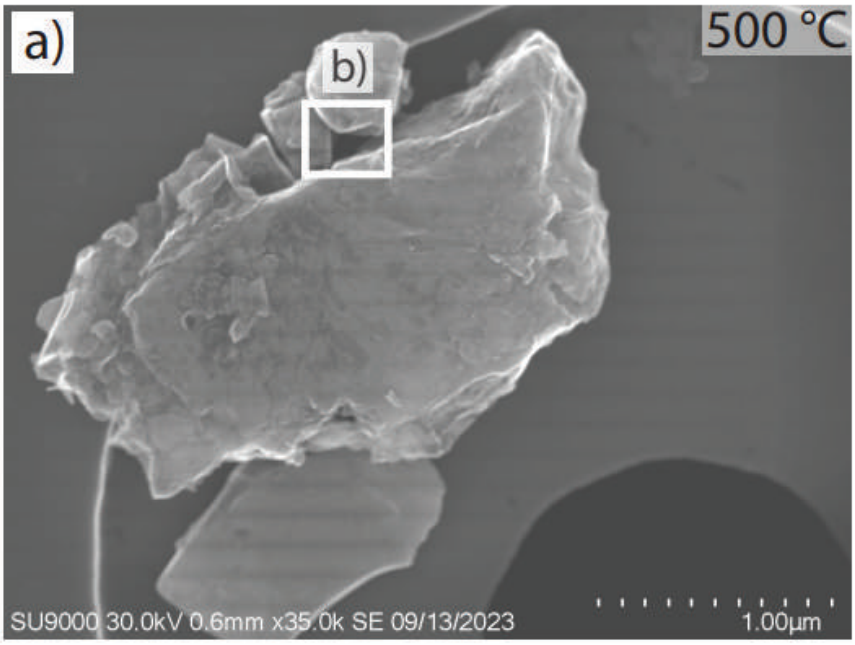
a)
b)
500 °C
SU9000 30.0kV 0.6mm x35.0k SE 09/13/2023
1.00µm

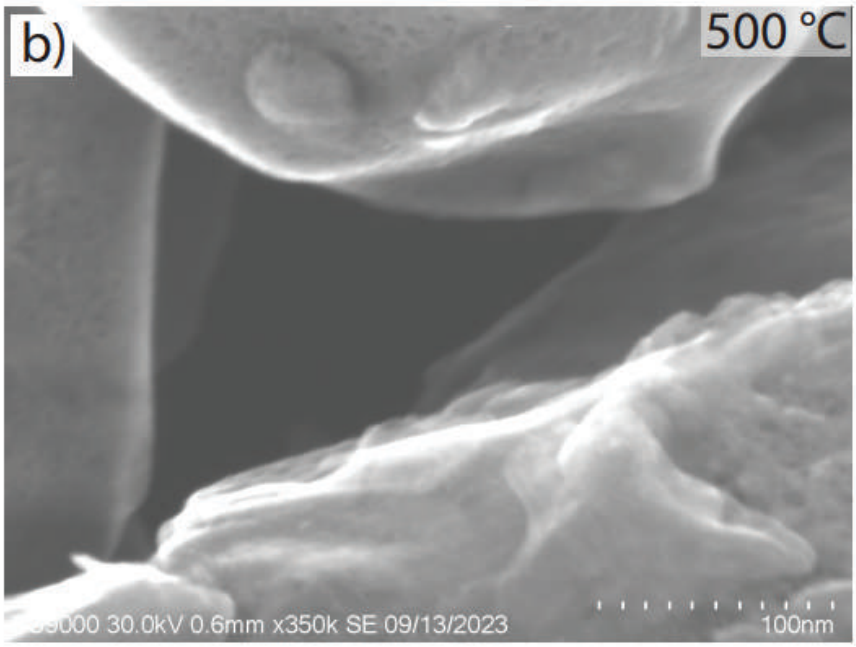
b)
500 °C
9000 30.0kV 0.6mm x350k SE 09/13/2023
100nm

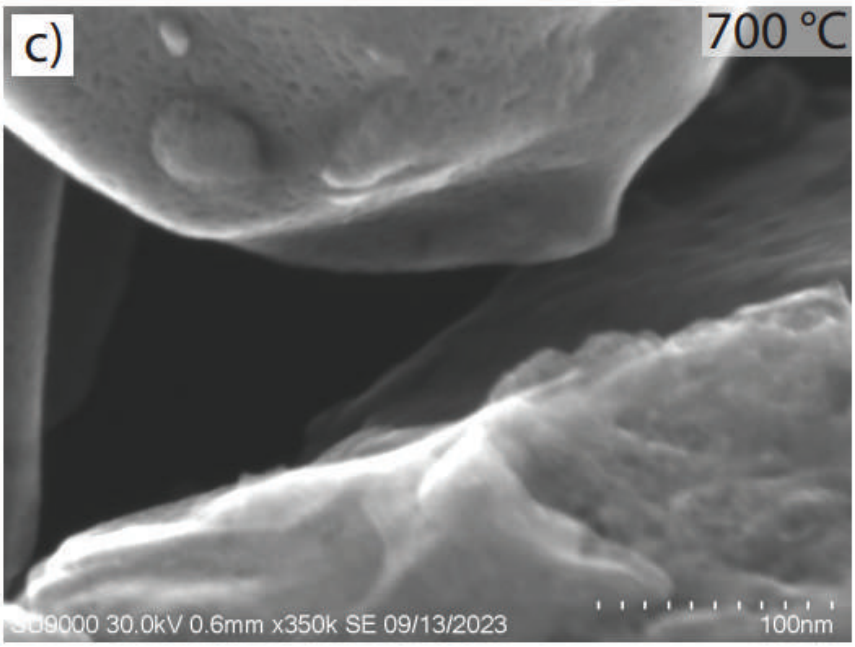
c)
700 °C
SU9000 30.0kV 0.6mm x350k SE 09/13/2023
100nm

Figure 28. STEM-based SE images of glass powder grain from area 1. (a) The entire grain observed during heating with frame indication of image b. (b) Pre-existing pores in the powder grain at 600 °C, below Tg. (c) Pore growth of the same location occurring at 800 °C.

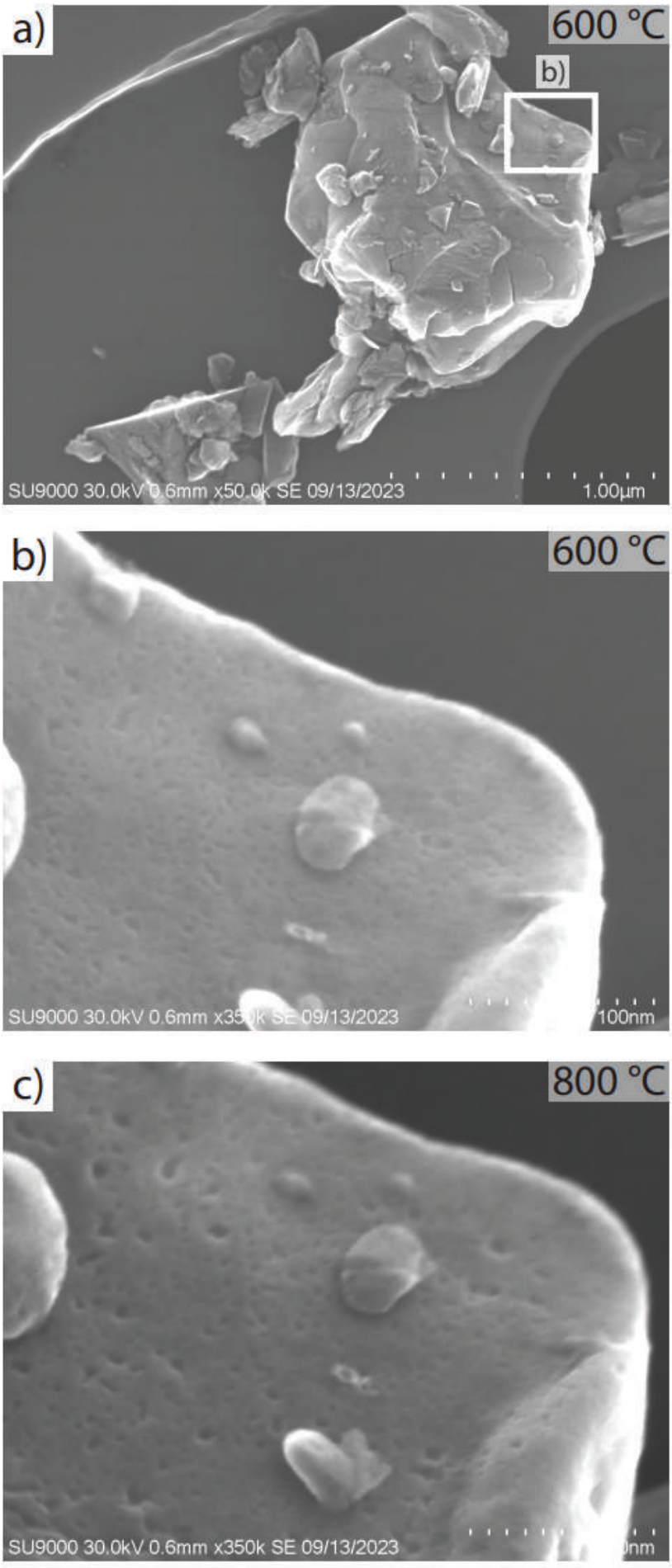
a)
600 °C
b)
SU9000 30.0kV 0.6mm x50.0k SE 09/13/2023
1.00µm
b)
600 °C
SU9000 30.0kV 0.6mm x350k SE 09/13/2023
100nm
c)
800 °C
SU9000 30.0kV 0.6mm x350k SE 09/13/2023

Figure 29. STEM-based SE images of glass powder grain from area 1. (a) ~1 minute after reaching 900 °C. Pre-existing pores are visible with the entire grain in view. (b) ~1 minute after reaching 1000 °C. The sample disintegrated where pores were present. The rest of the sample remains comparatively intact.

~1 Minute After 900 °C

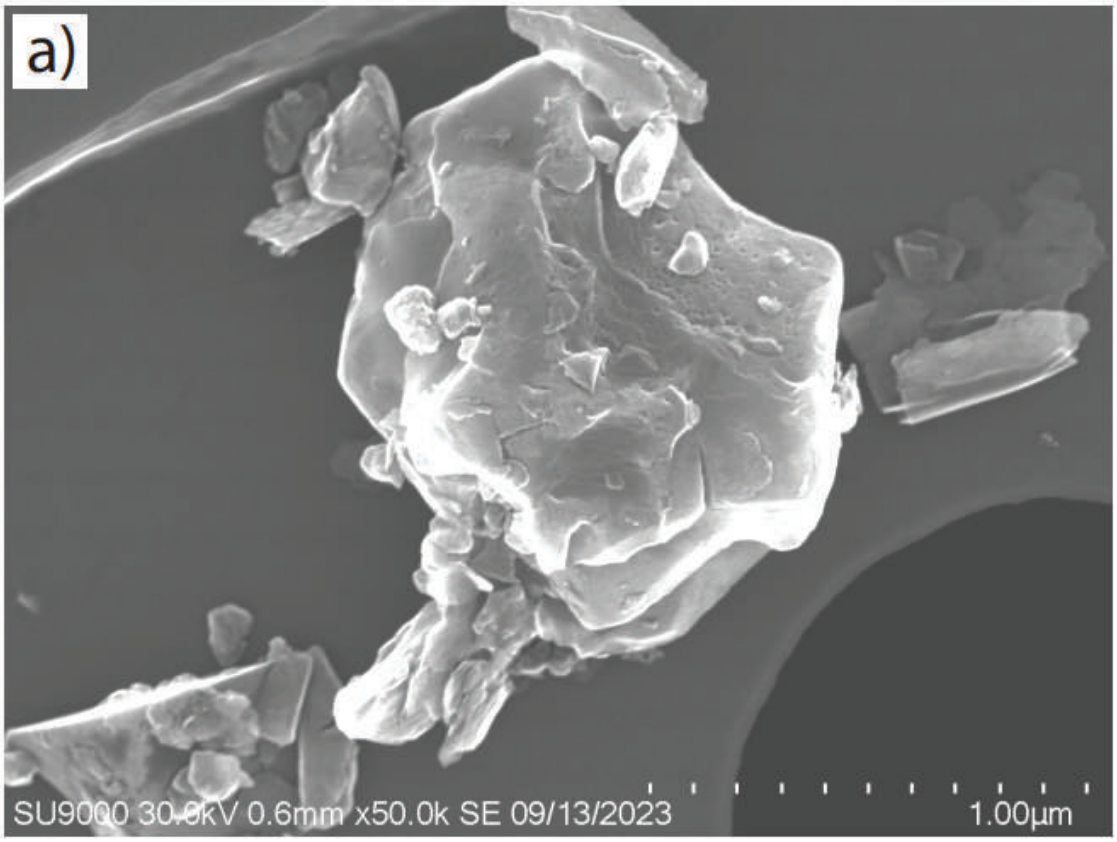

~1 Minute After 1000 °C Reached (75 minutes in 900 °C)

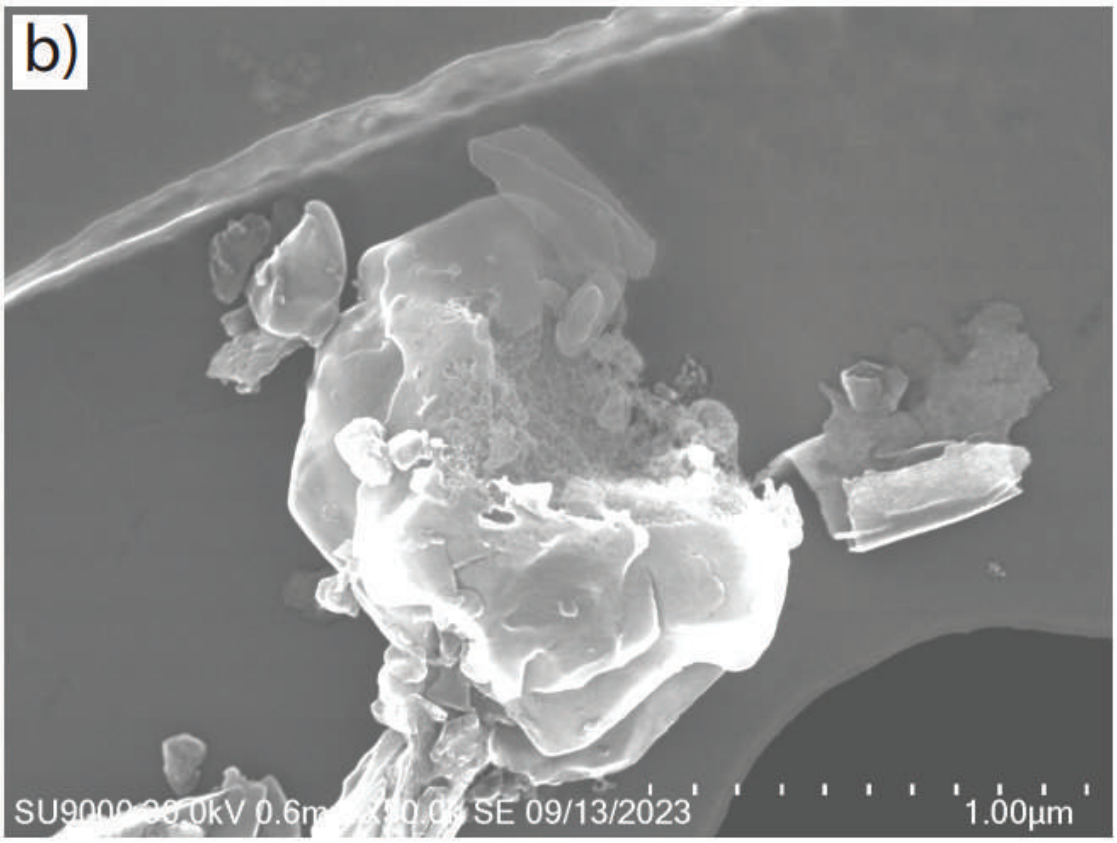

Figure 30. STEM-based SE images of glassy powder from area 3. (a) Entire powder grain with windows indicating c and d. (b) 5 minutes after reaching 900 °C, where separated grain was first seen attached to the rest of the area. (c) 19 minutes after reaching 1000 °C, with nano-sized bubbles, vesicles, and plagioclase nucleating and growing. (d) Melted powder grain 60 minutes after reaching 1000 °C, conjoined with the rest of the area.

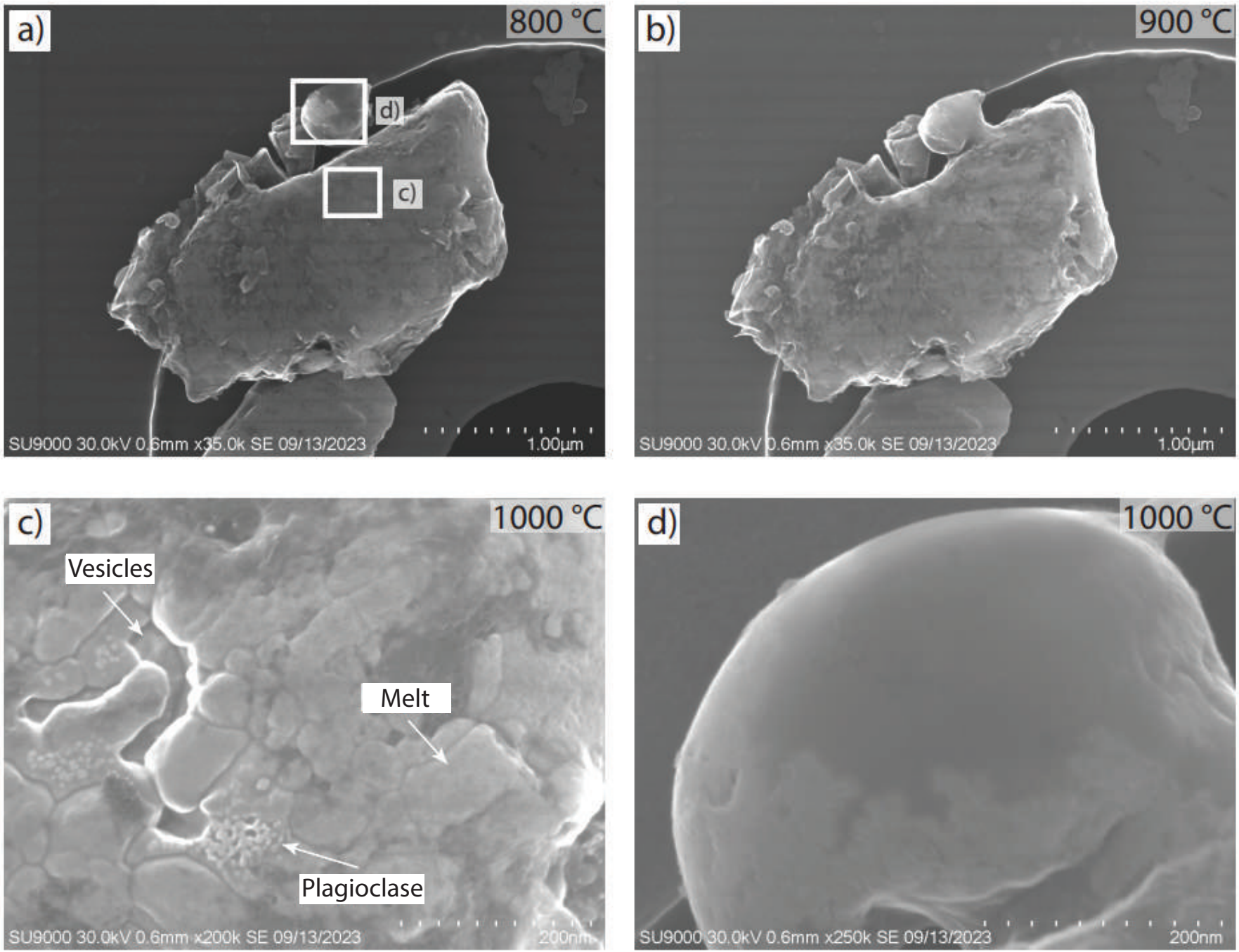
a)
800 °C
d)
c)
SU9000 30.0kV 0.6mm x35.0k SE 09/13/2023
1.00µm
b)
900 °C
SU9000 30.0kV 0.6mm x35.0k SE 09/13/2023
1.00µm
c)
1000 °C
Vesicles
Melt
Plagioclase
SU9000 30.0kV 0.6mm x200k SE 09/13/2023
200nm
d)
1000 °C
SU9000 30.0kV 0.6mm x250k SE 09/13/2023
200nm

Figure 31. STEM-based SE images of spherulite bearing powder from area 3. (a) Entire grain of the area at 500 ℃. (b) Vesicle forming at 700 ℃.

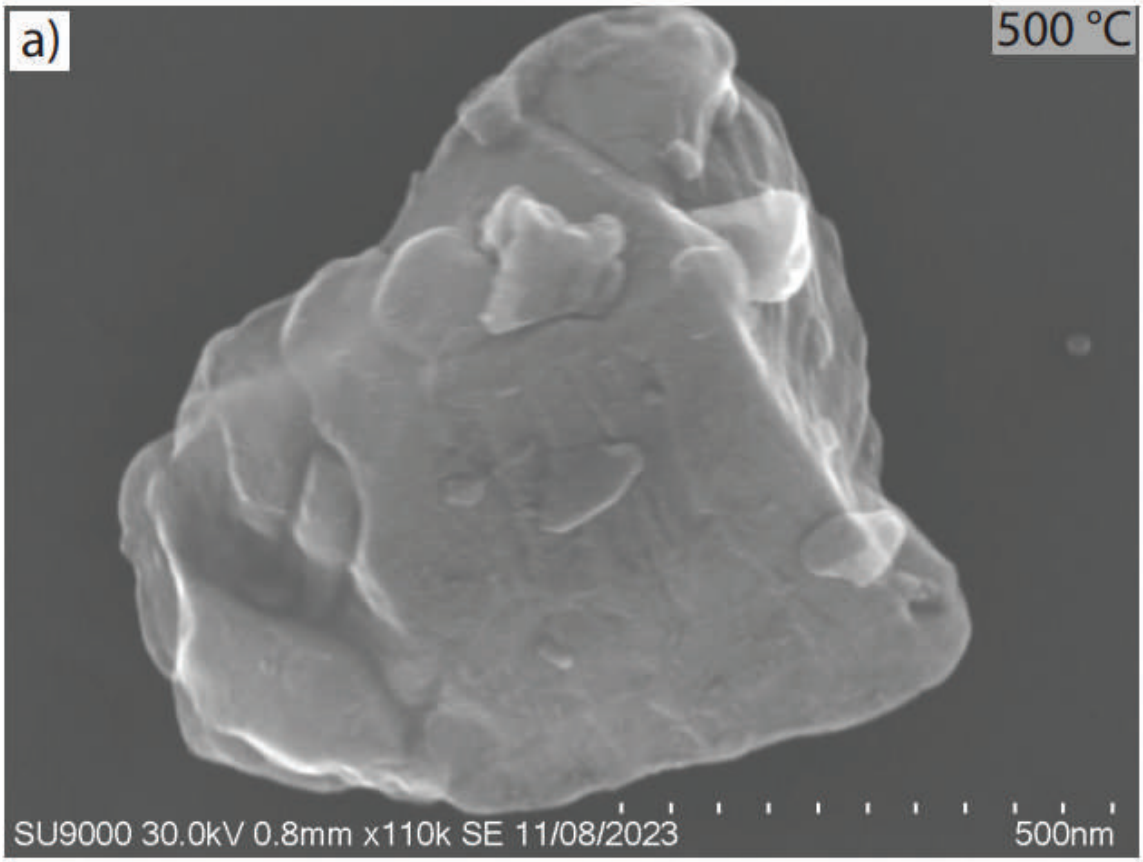
a)
500 °C
SU9000 30.0kV 0.8mm x110k SE 11/08/2023
500nm

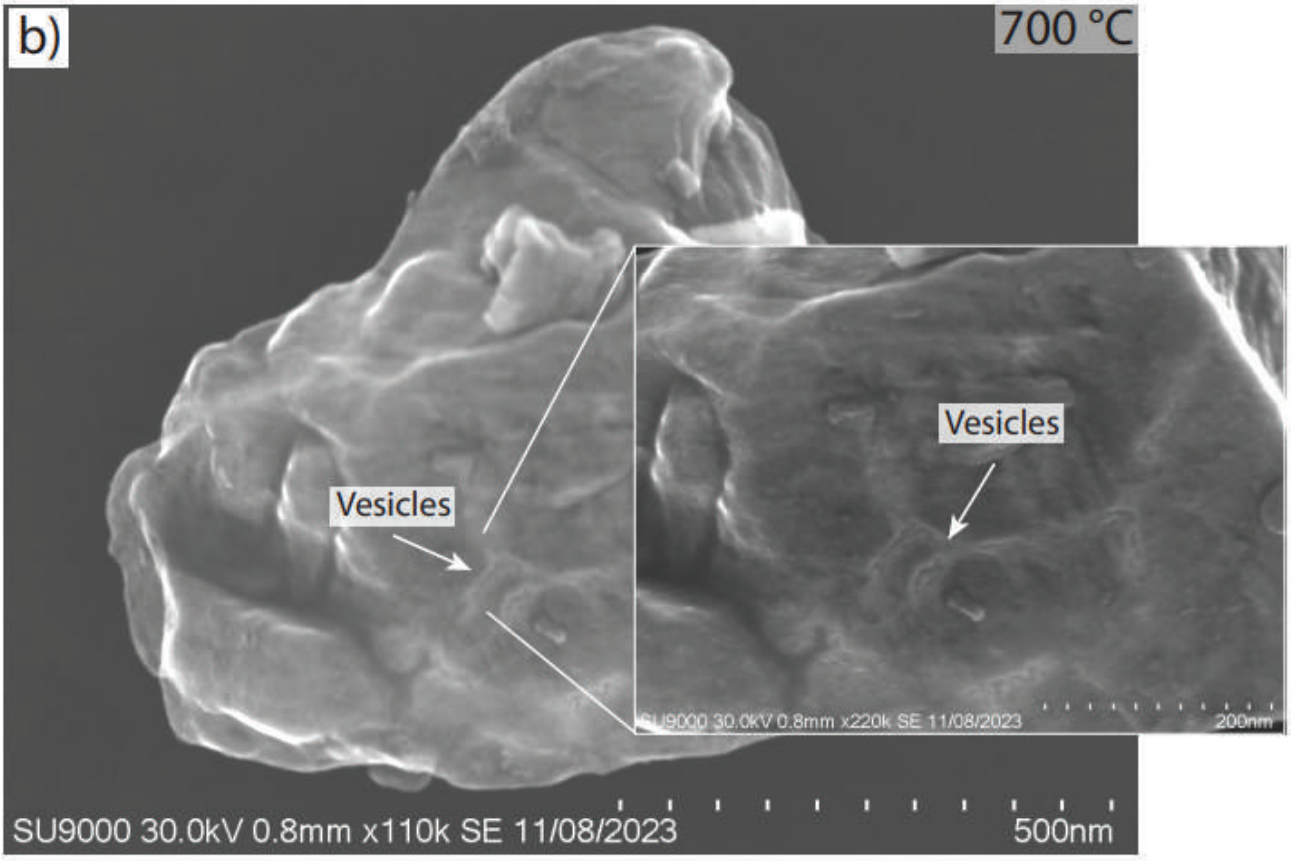
b)
700 °C
Vesicles
Vesicles
SU9000 30.0kV 0.8mm x220k SE 11/08/2023
200nm
SU9000 30.0kV 0.8mm x110k SE 11/08/2023
500nm

Figure 32. STEM-based SE images of spherulite bearing area powders at 1000 °C shown in (a) Area 1,(b) Area 2, (c) Area 3, and (d) Area 4.

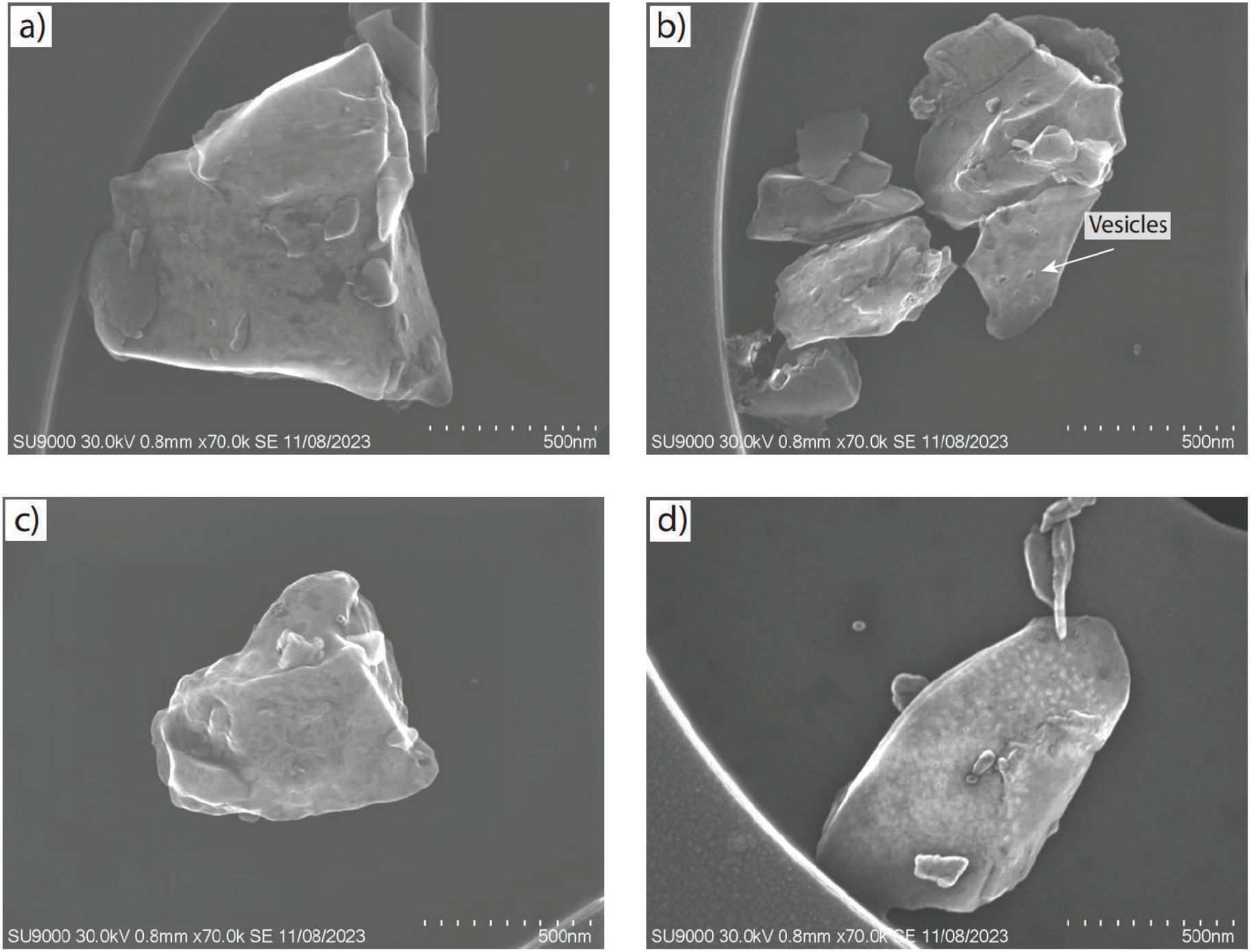
a)
SU9000 30.0kV 0.8mm x70.0k SE 11/08/2023
500nm
b)
Vesicles
SU9000 30.0kV 0.8mm x70.0k SE 11/08/2023
500nm
c)
SU9000 30.0kV 0.8mm x70.0k SE 11/08/2023
500nm
d)
SU9000 30.0kV 0.8mm x70.0k SE 11/08/2023
500nm

Figure 33. Photograph of the center cut of sample RRG-01.Figure 33. Photograph of the center cut of sample RRG-01.

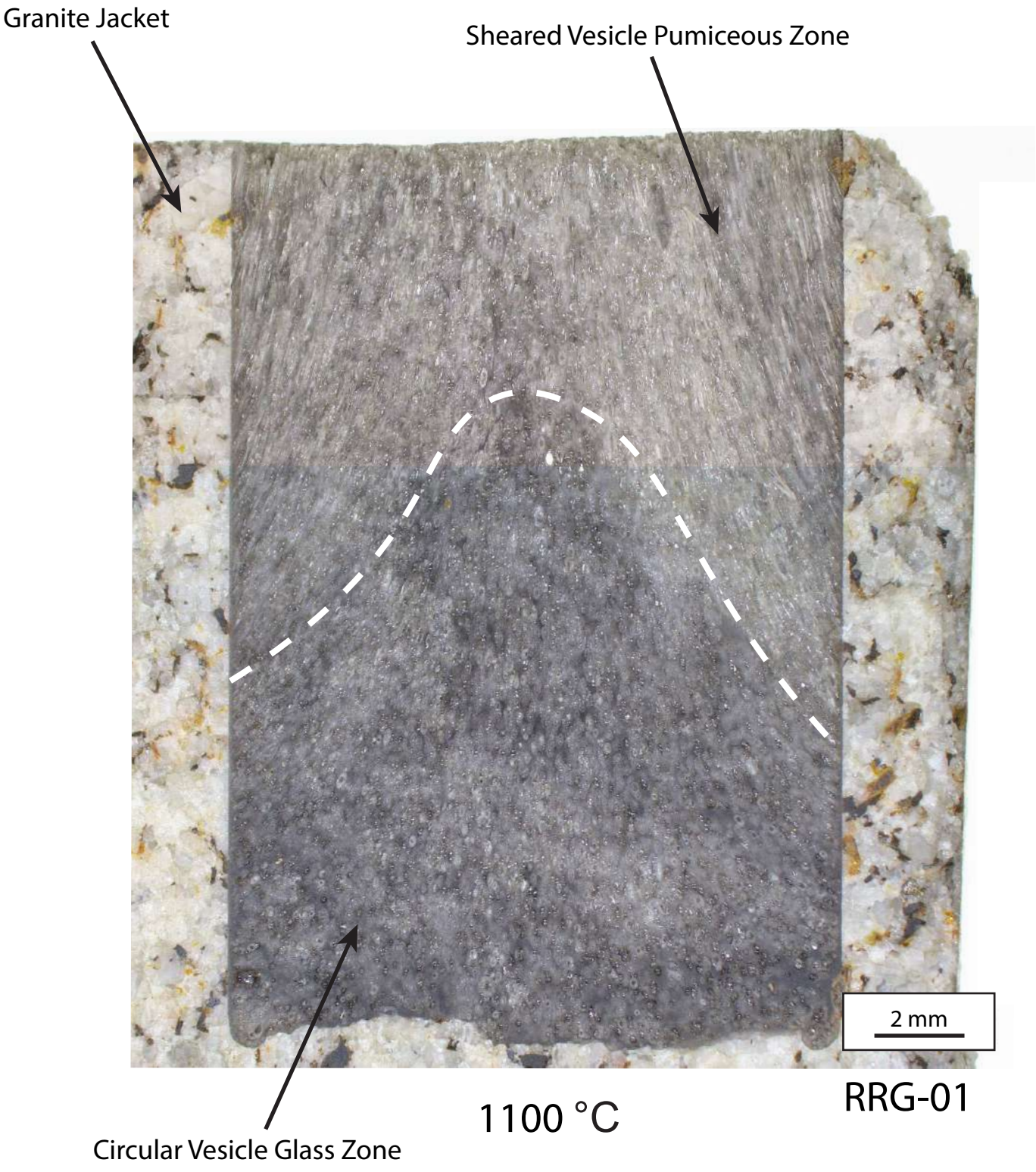
Granite Jacket
Sheared Vesicle Pumiceous Zone
2 mm
1100 °C
RRG-01
Circular Vesicle Glass Zone

Figure 34. Photograph of extruded portion of sample RRG-01 before being sectioned for analytical investigation.

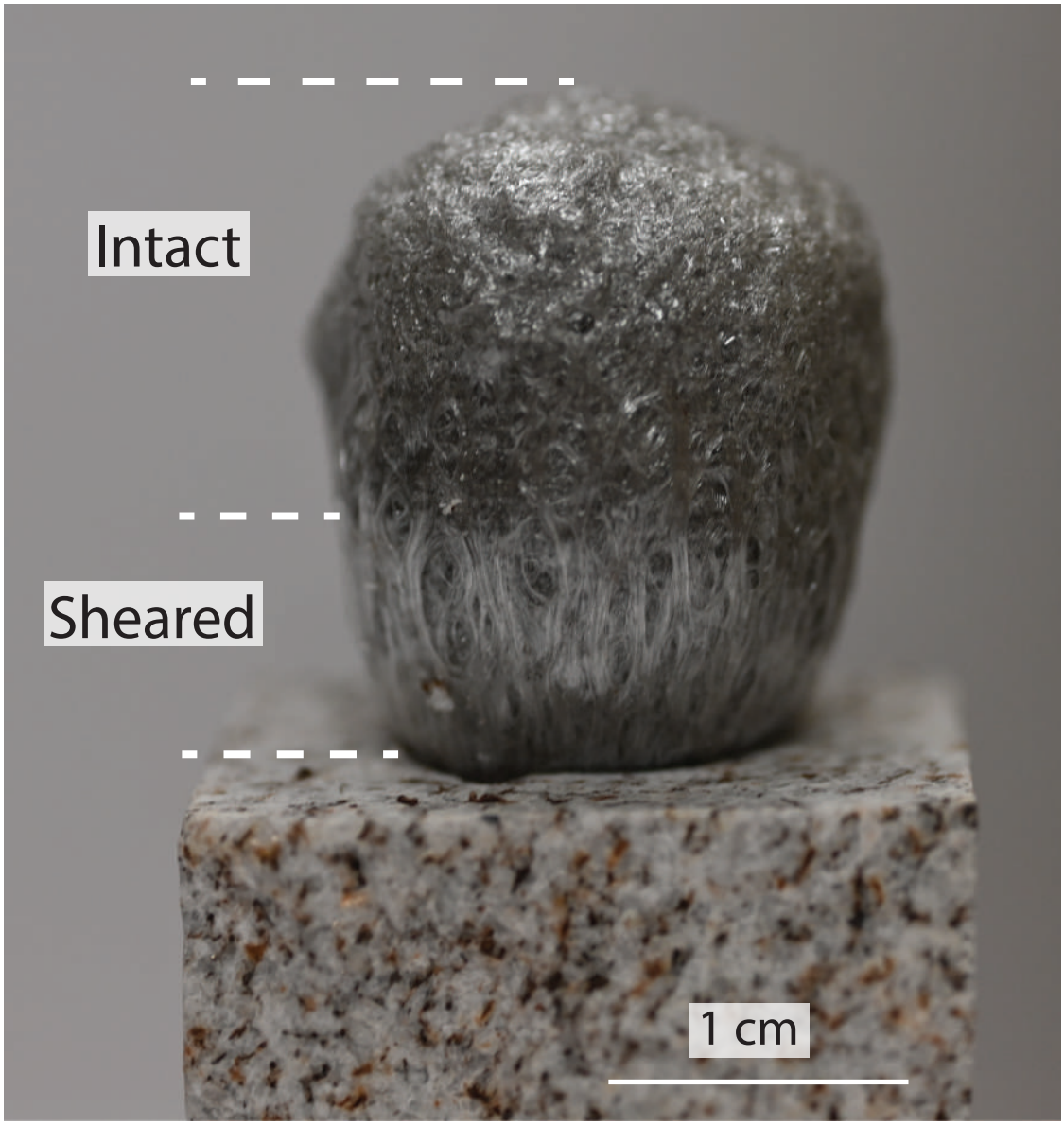
Intact
Sheared
1 cm

Figure 35. Photograph of the margin cut of sample RRG-01.

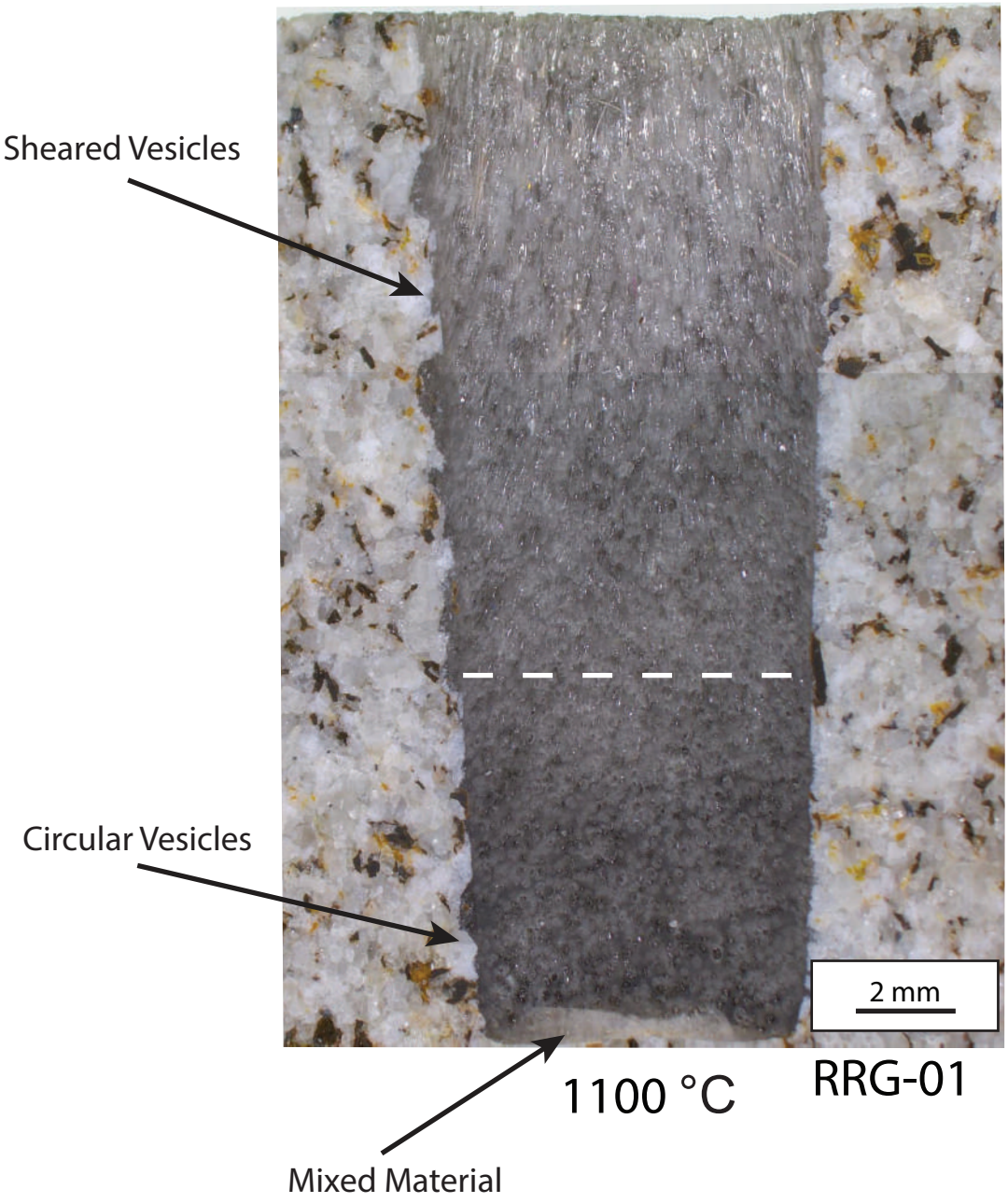
Sheared Vesicles
Circular Vesicles
2 mm
1100 °C
RRG-01
Mixed Material

Figure 36. Photograph of the top cut of sample RRG-01.

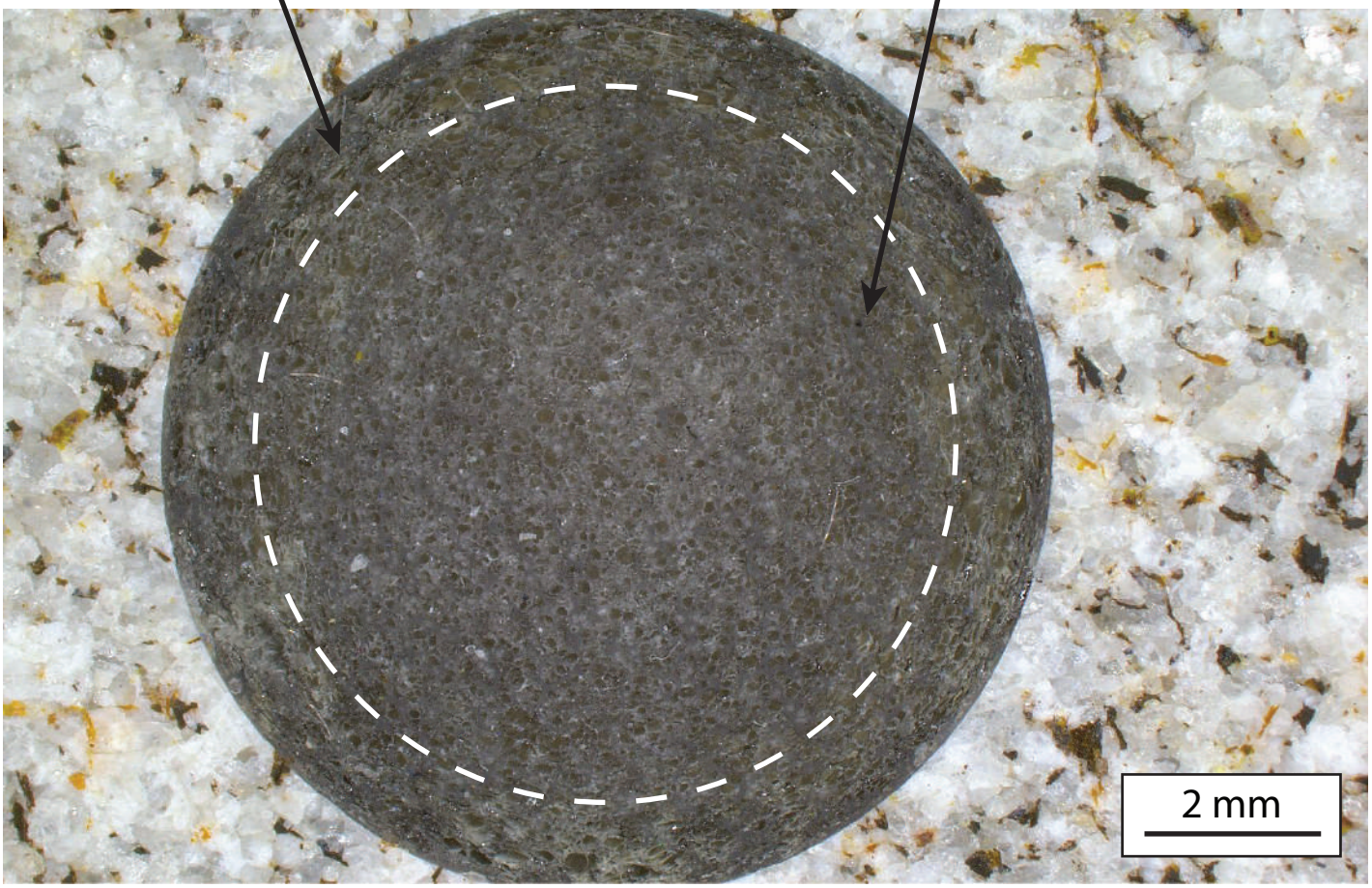

1100 °C

RRG-01

Figure 37. Photograph of the center cut of sample RRS-01.

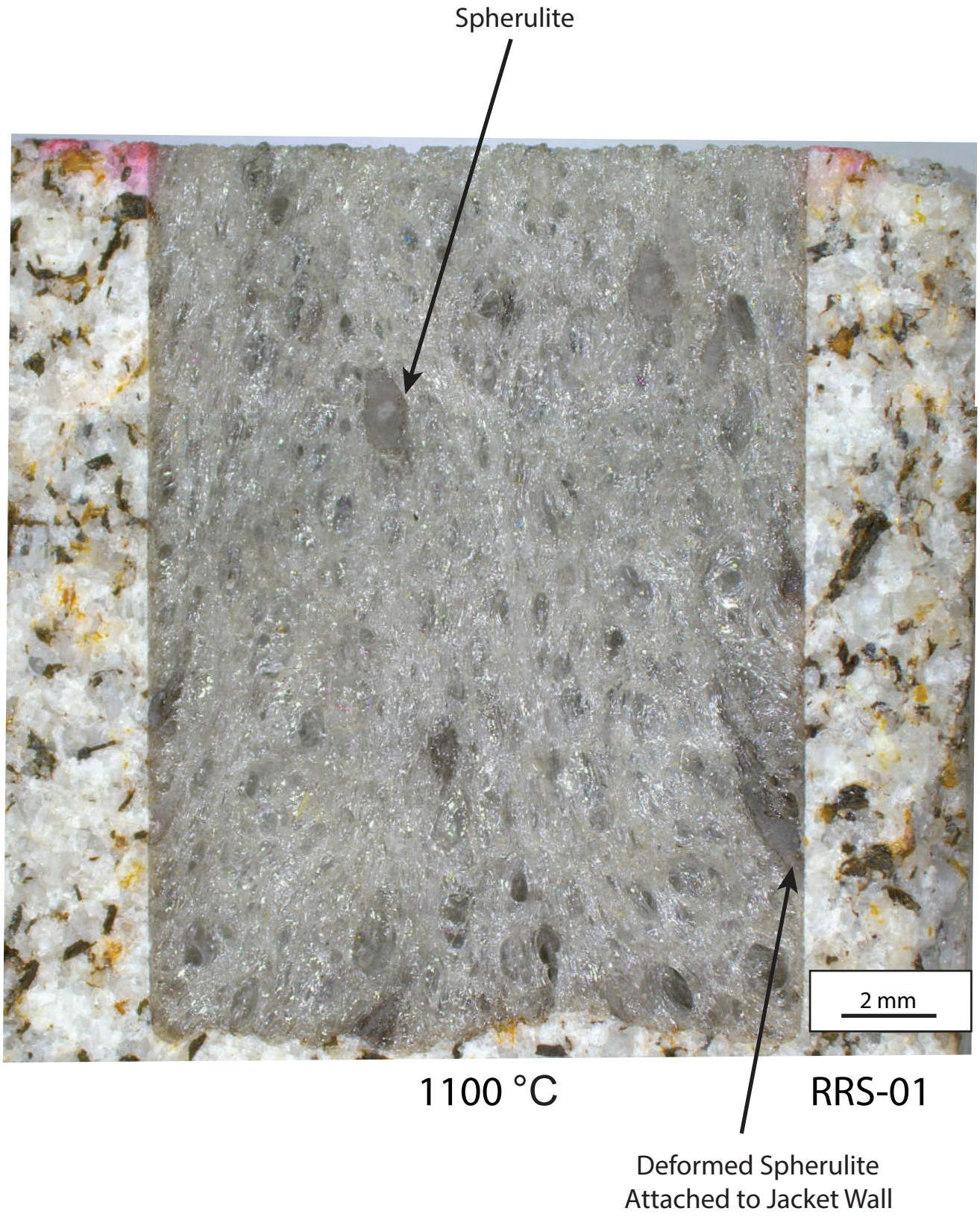
Spherulite
2 mm
1100 °C
RRS-01
Deformed Spherulite
Attached to Jacket Wall

Figure 38. Photograph of the margin cut of sample RRS-01.

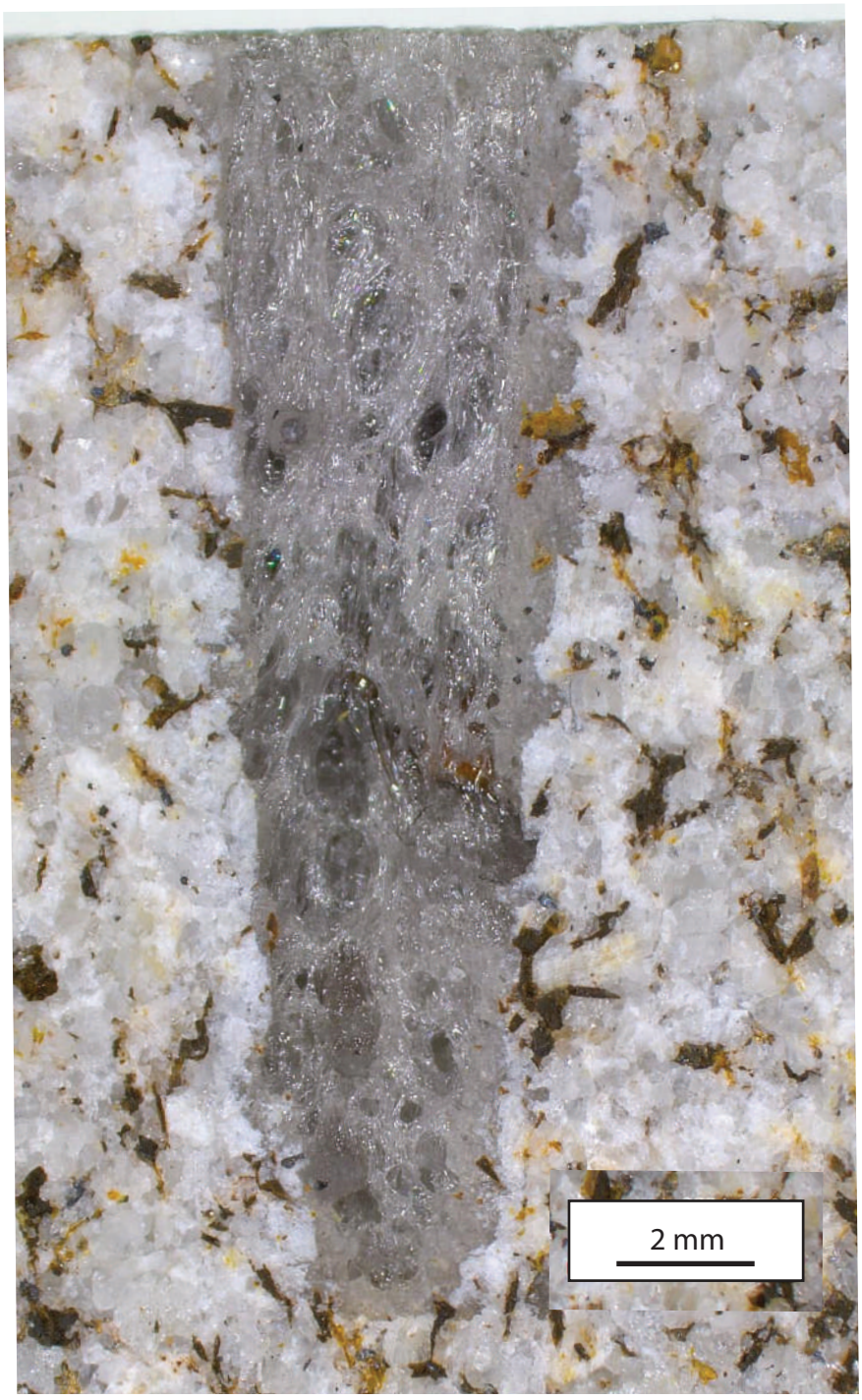

1100 °C RRS-01

Figure 39. Photograph of the top cut of sample RRS-01.

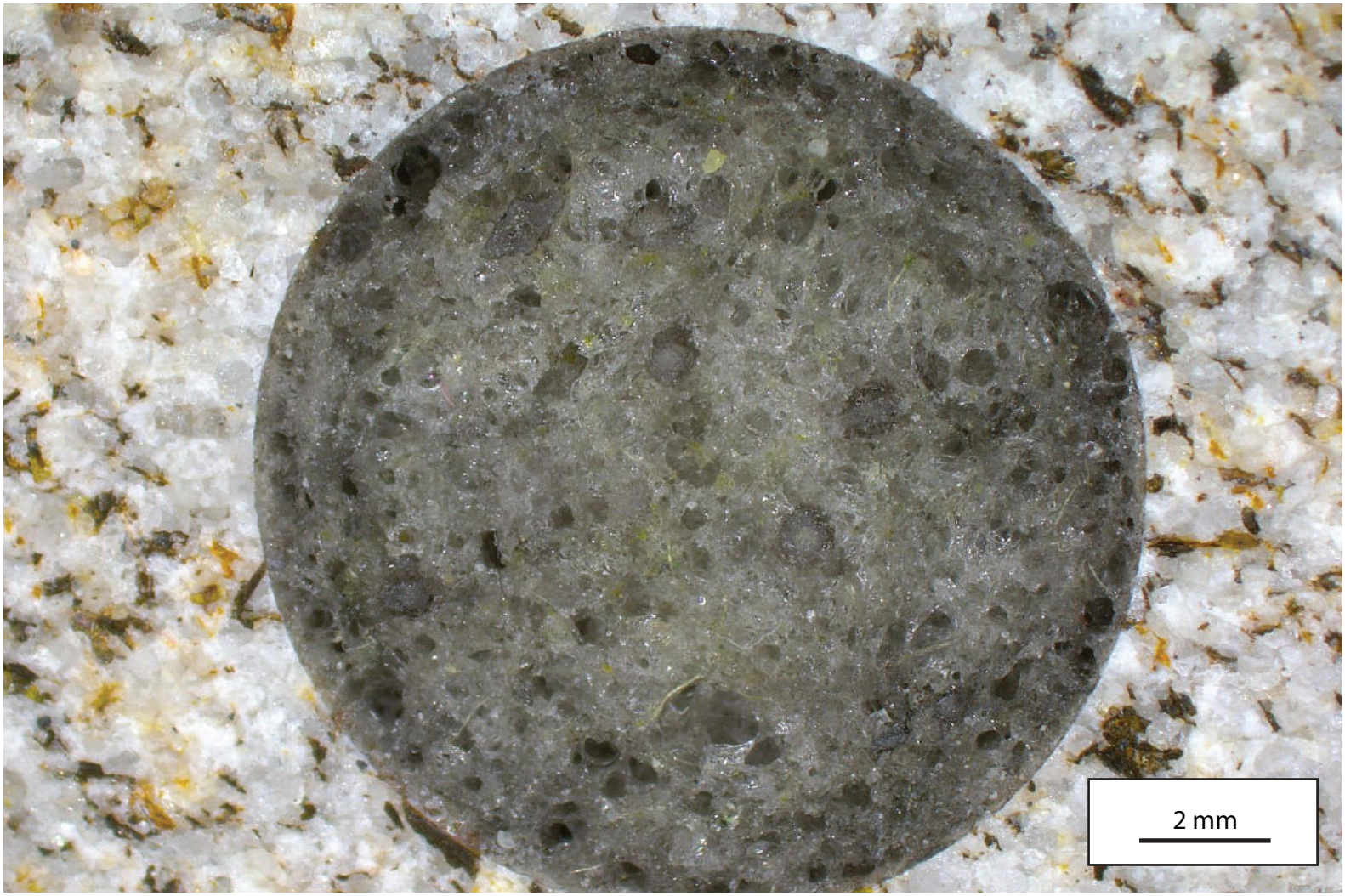

1100 °C RRS-01

Figure 40. SEM-based BSE image of sample RRG-01 showing oriented vesicles stretching towards the top of the granite conduit (towards the top of the image). For reference, grains of the granite jacket are observable on the bottom left side of the image.

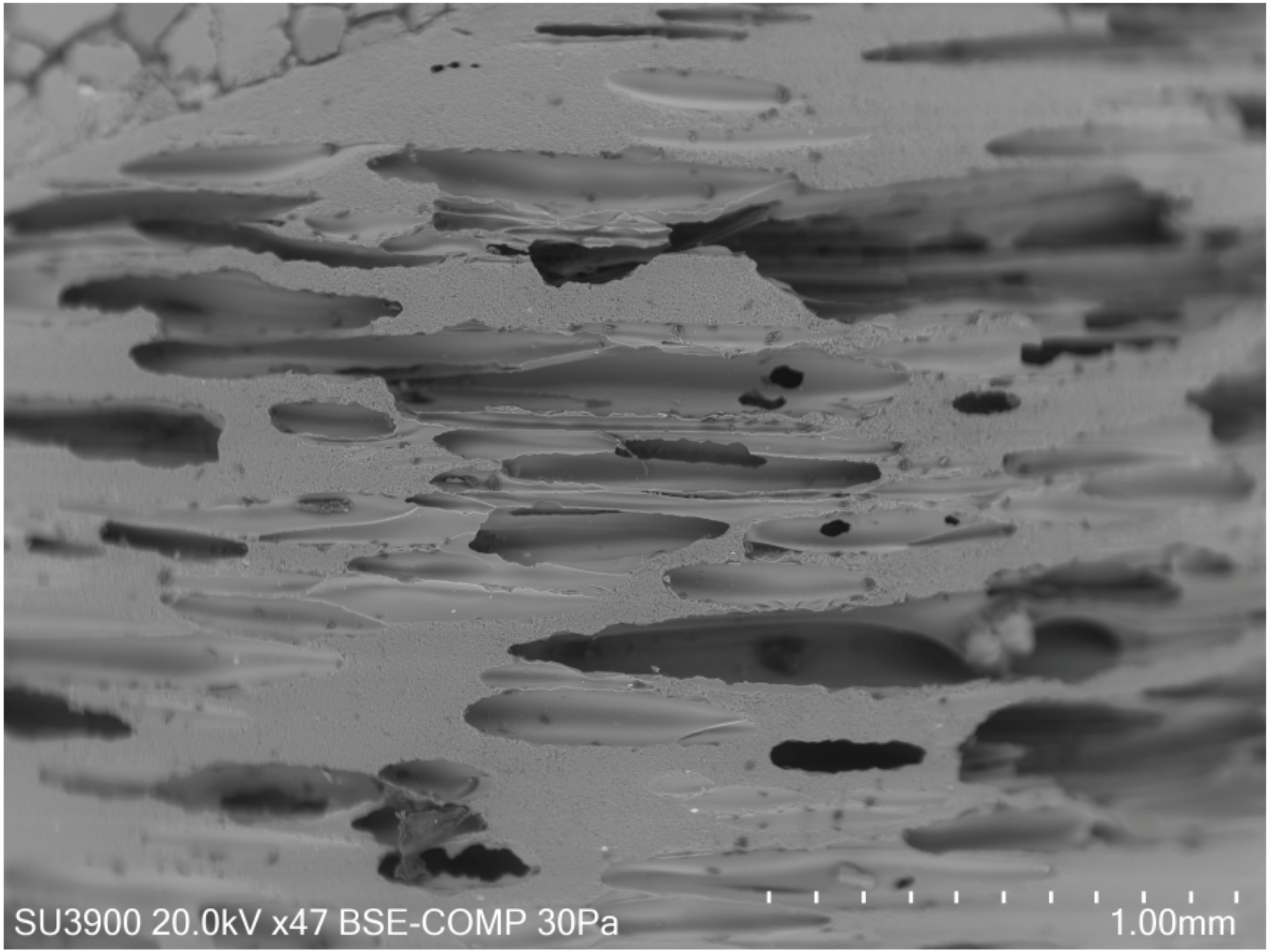
SU3900 20.0kV x47 BSE-COMP 30Pa
1.00mm

Figure 41. SEM-based BSE image of sample RRS-01 showing oriented vesicles stretching towards the top of the granite conduit (towards the top of the image). For reference, grains of the granite jacket are observable on the top left side of the image.

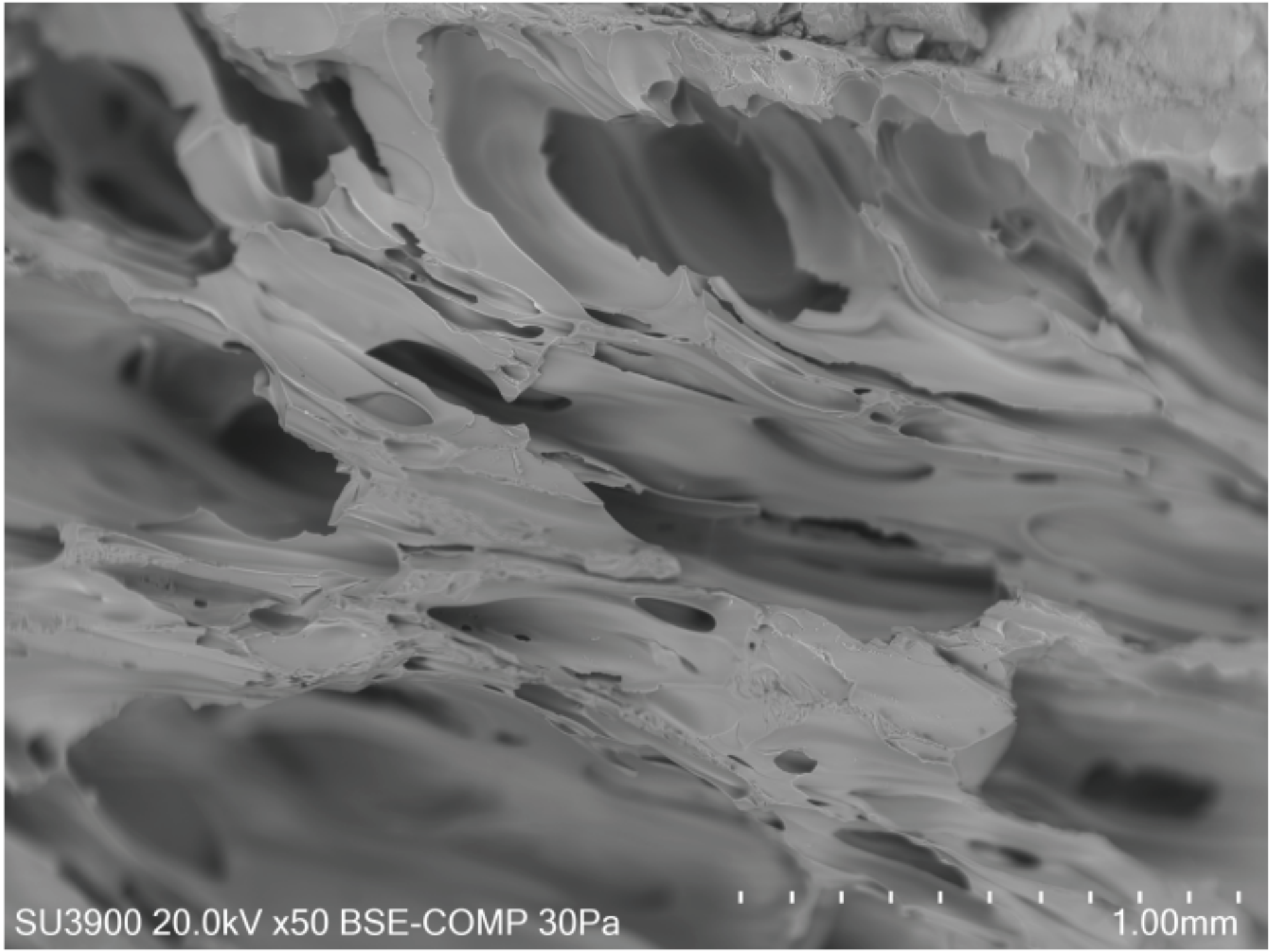
SU3900 20.0kV x50 BSE-COMP 30Pa
1.00mm

Figure 42. Top view of unextruded sample RRG-02 within the granite conduit.

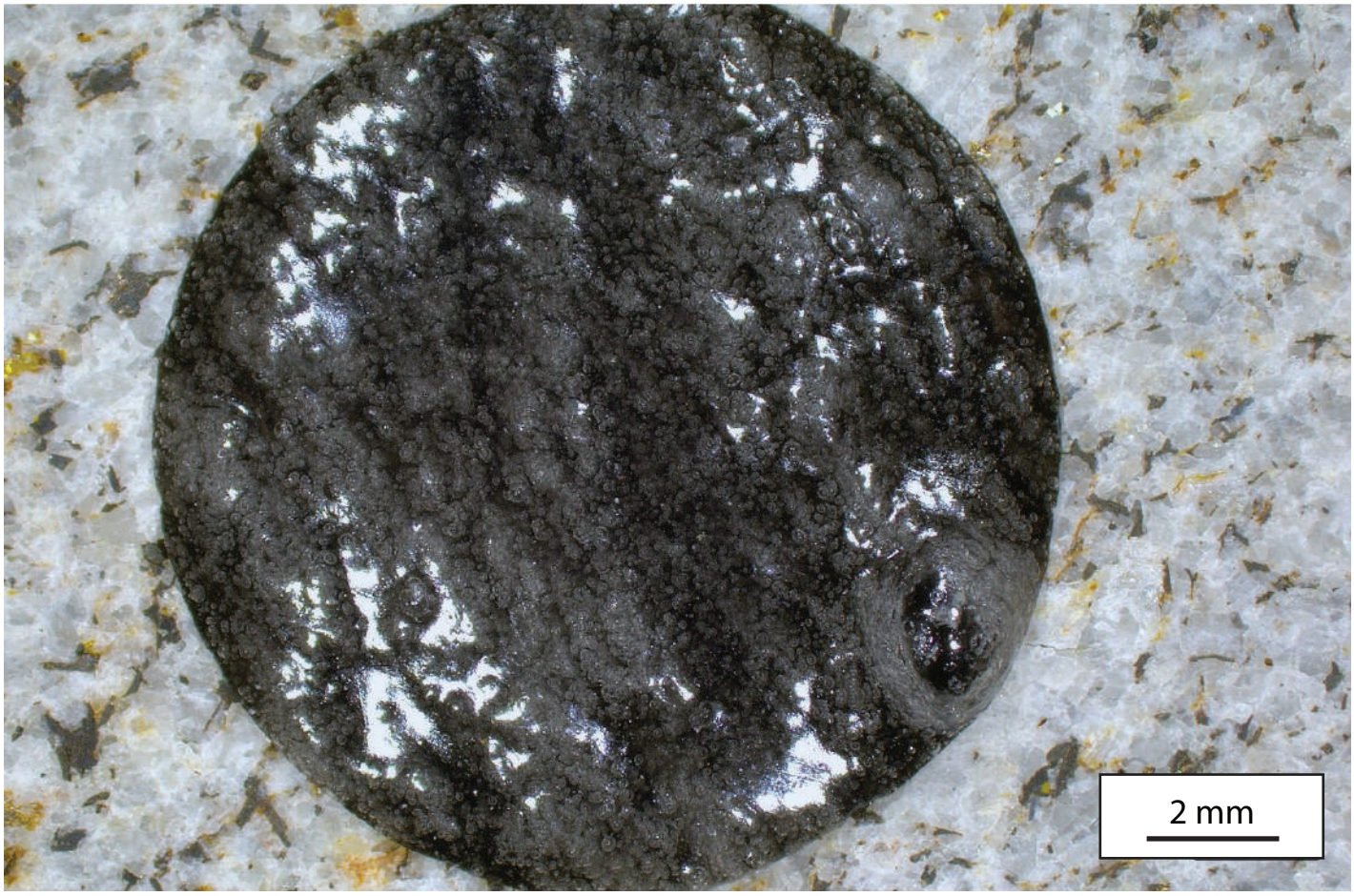

1050 °C RRG-02

Figure 43. Photograph of the center cut of sample RRS-02.

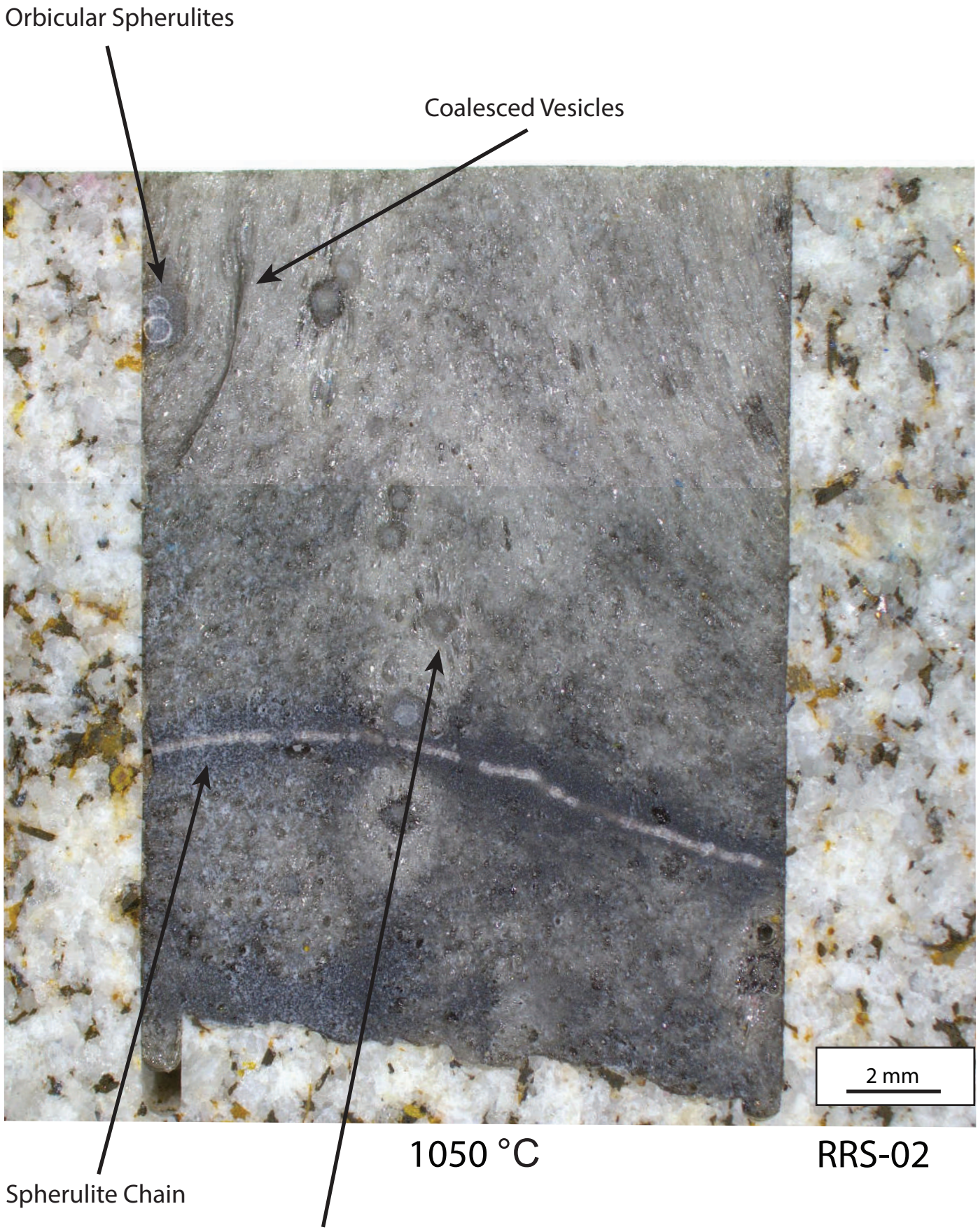
Orbicular Spherulites
Coalesced Vesicles
2 mm
1050 °C
RRS-02
Spherulite Chain
Vesicles Attached To Spherulite

Figure 44. Photograph of the margin cut of sample RRS-02.

1050 °C RRS-02

Figure 45. Photograph of the top cut of sample RRS-02.

1050 °C RRS-02

Figure 46. Photograph of the center cut of sample RRS-03.

1000 °C

RRS-03

Figure 47. Photograph of the margin cut of sample RRS-03.


Pumice Vesicles
2 mm
1000 °C
RRS-03

Figure 48. SamplesRRG-04 and RRS-04. (a) Sample RRG-04 not welded to the jacket wall after heating. (b) Top half of sample RRS-04.

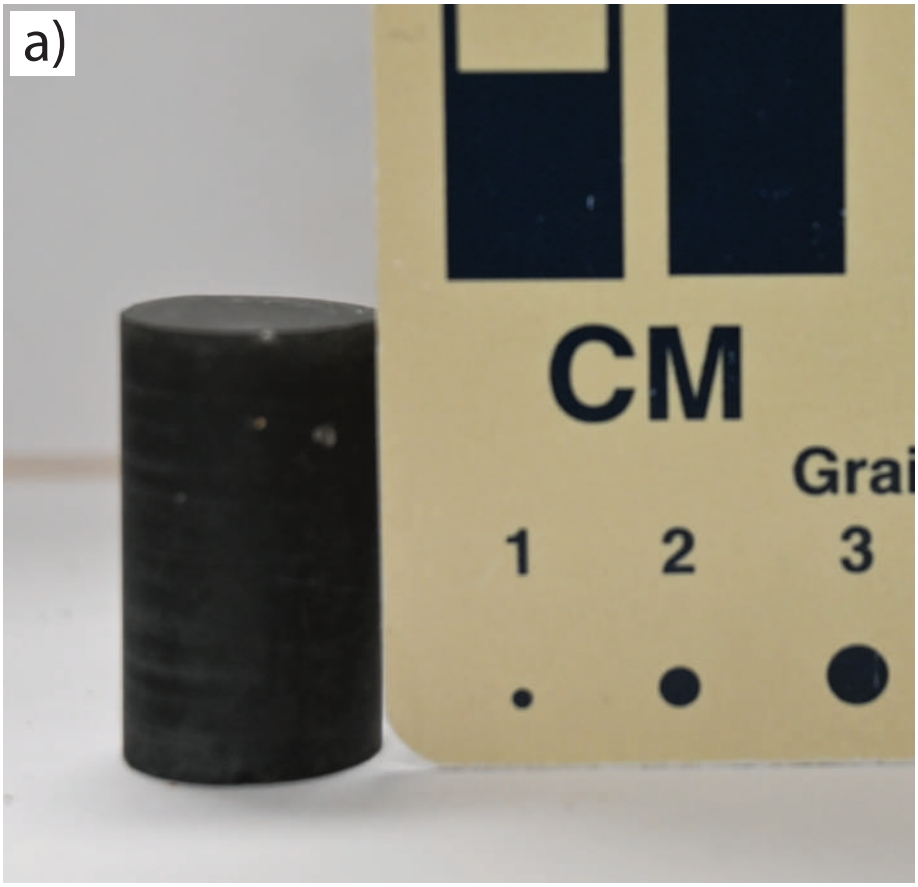
a)
CM
Grai
1
2
3

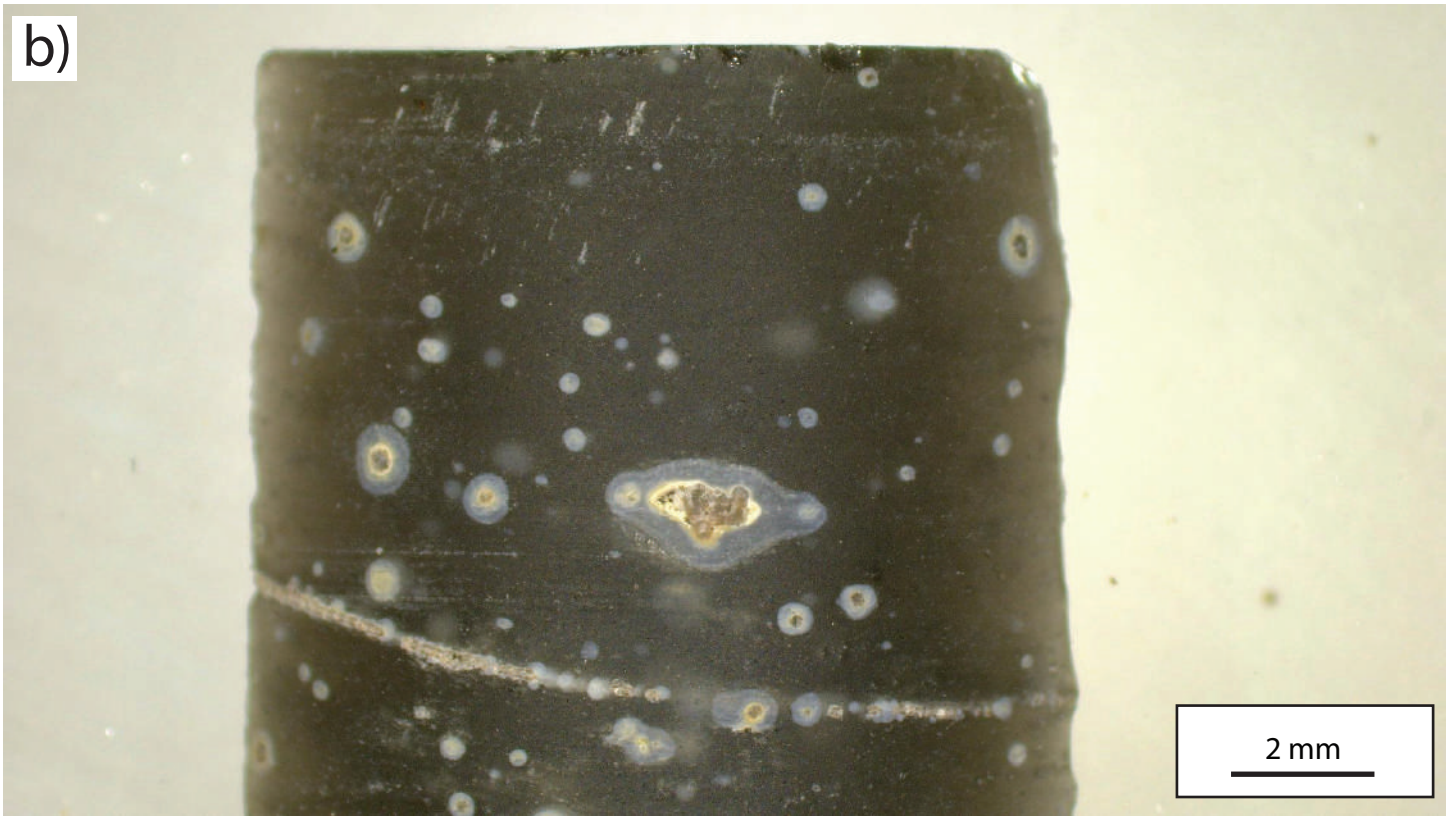
b)
2 mm

Figure 49. Photograph of the center cut of sample RRG-05.

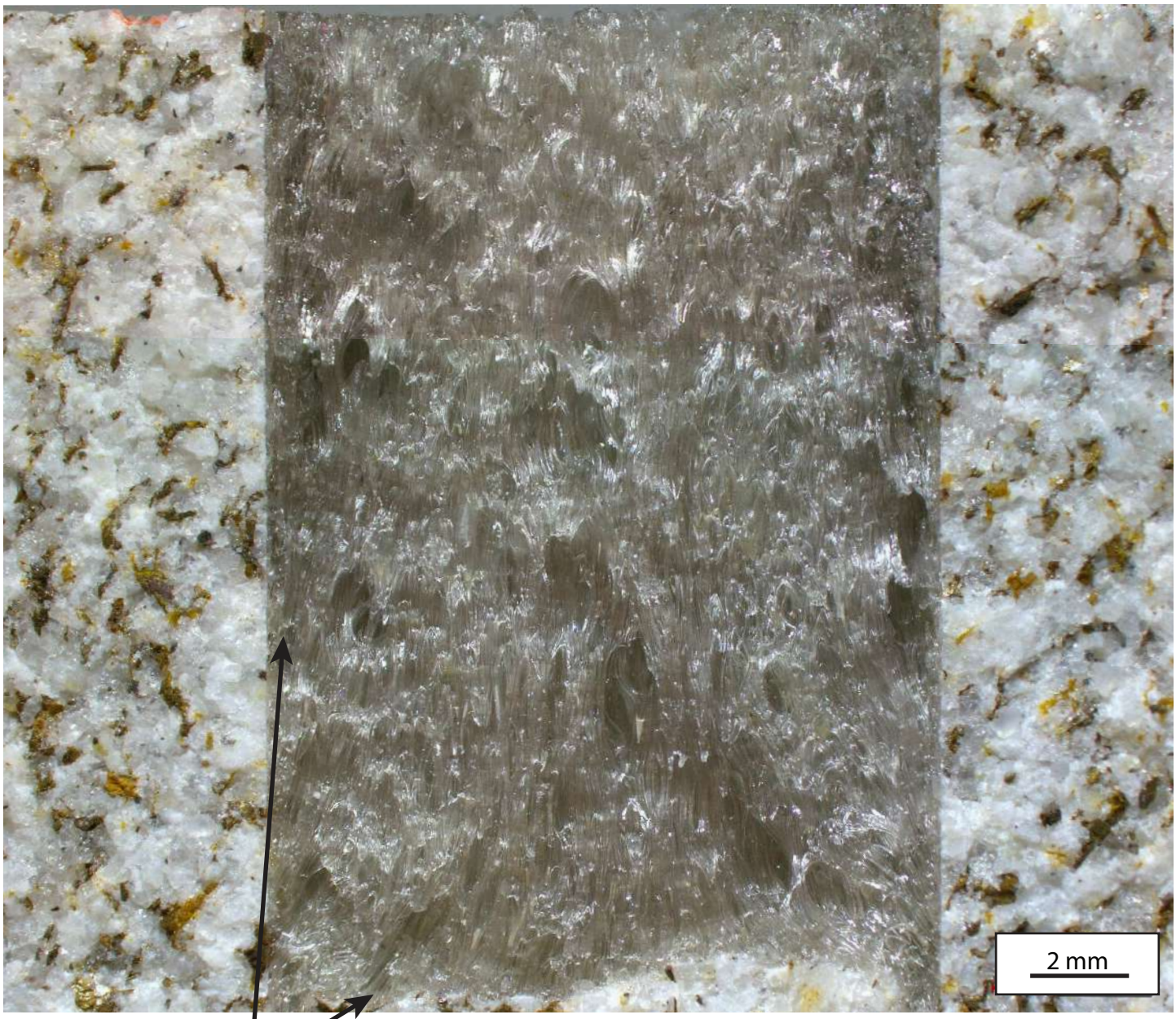
2 mm
1150 °C
RRG-05
Vesicles Attached
To Jacket Wall/Floor

Figure 50. Photograph of the margin cut of sample RRG-05.

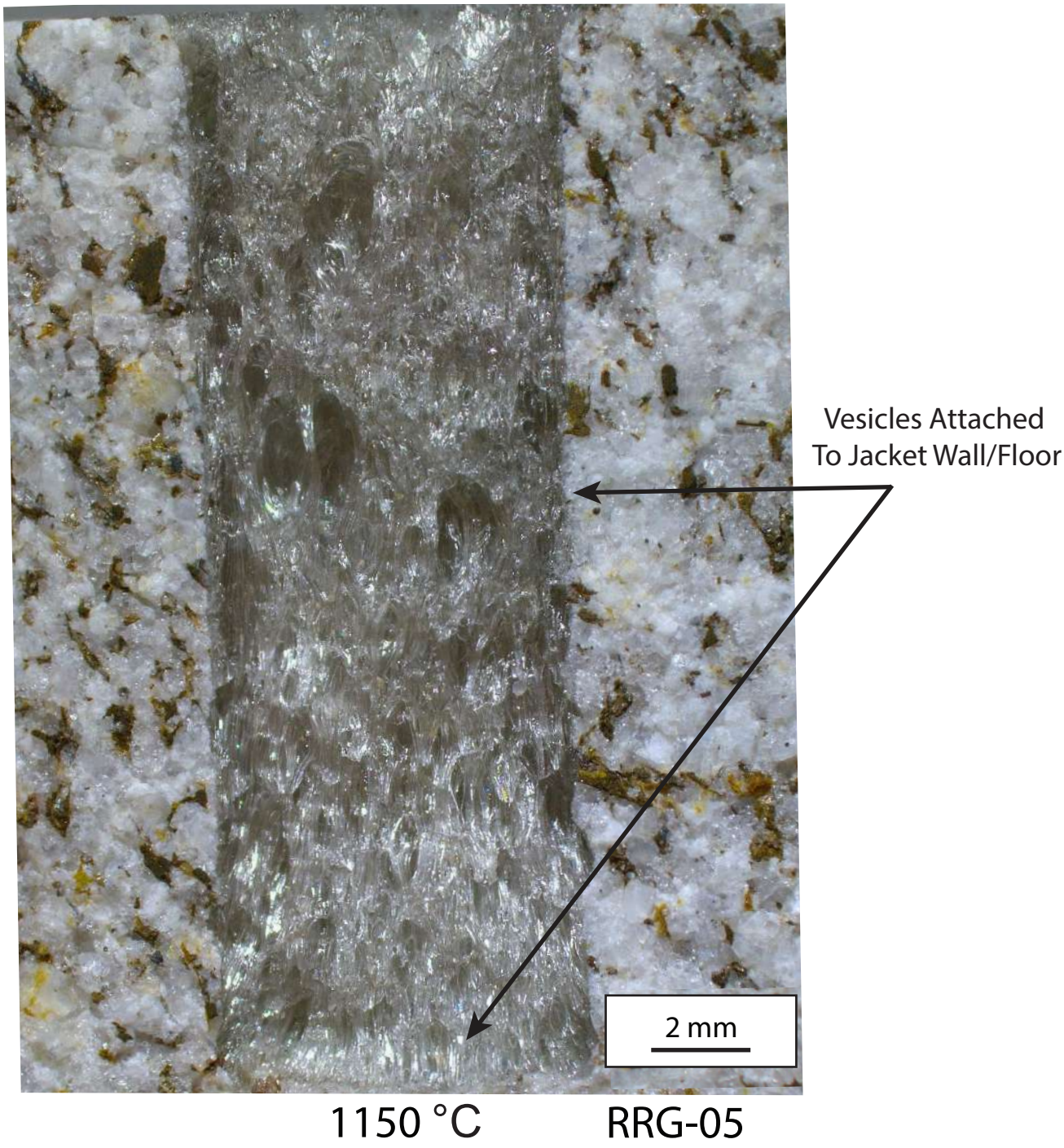
Vesicles Attached
To Jacket Wall/Floor
2 mm
1150 °C
RRG-05

Figure 51. Photograph of the top cut of sample RRG-05.

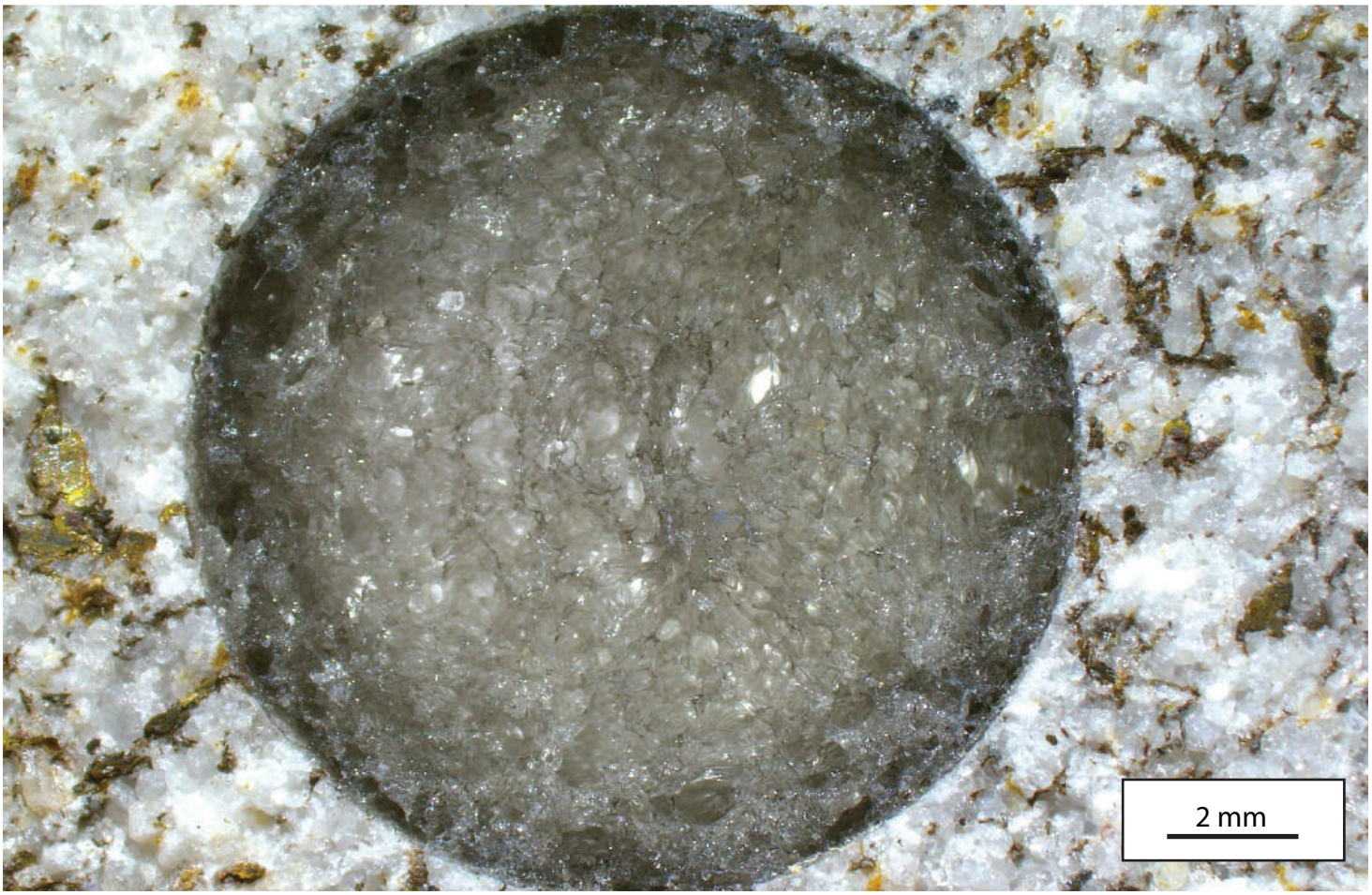

1150 °C RRG-05

Figure 52. Photograph of the center cut of sample RRS-05.

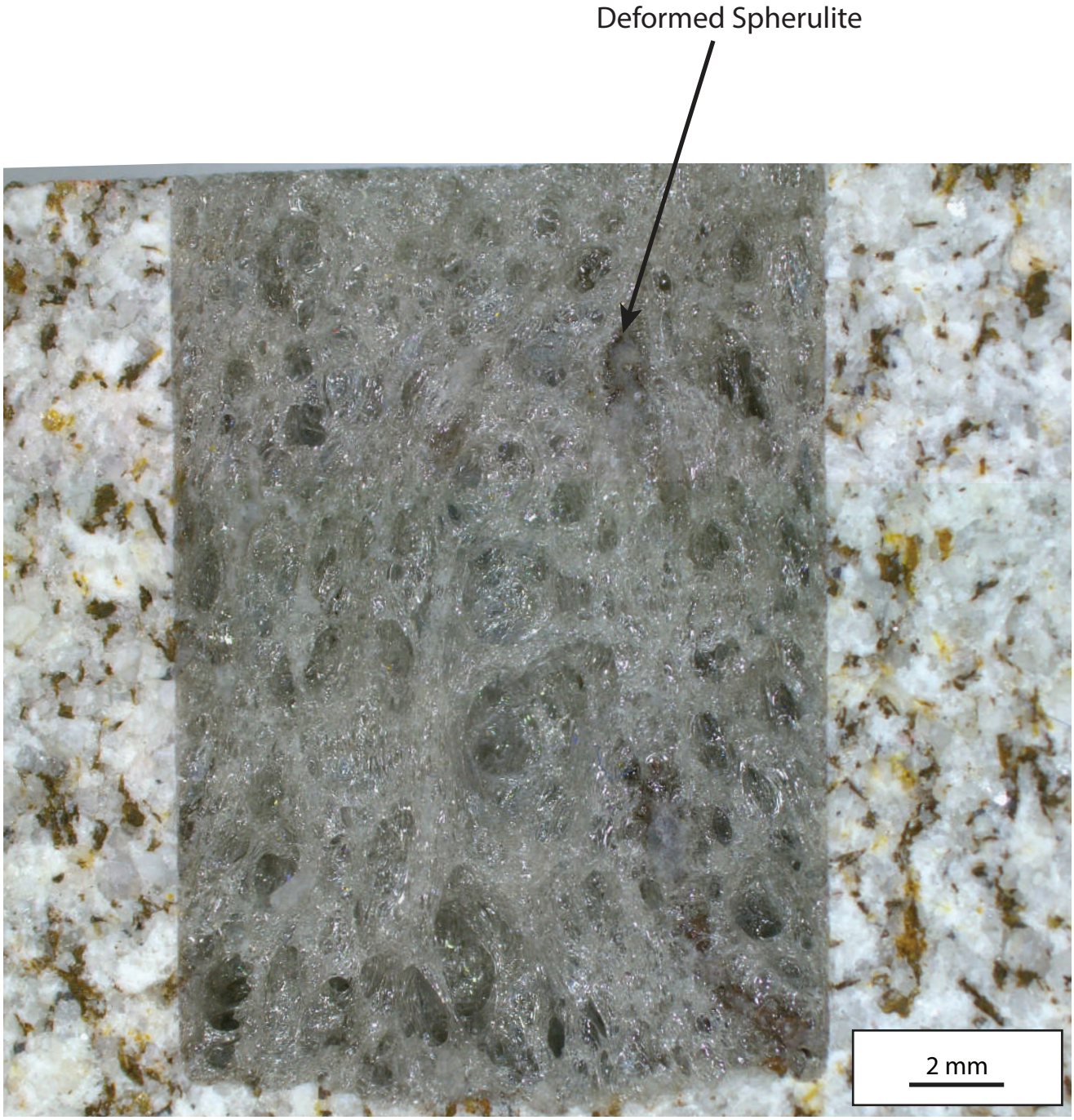

1150 °C RRS-05

Figure 53. Photograph of the margin cut of sample RRS-05.

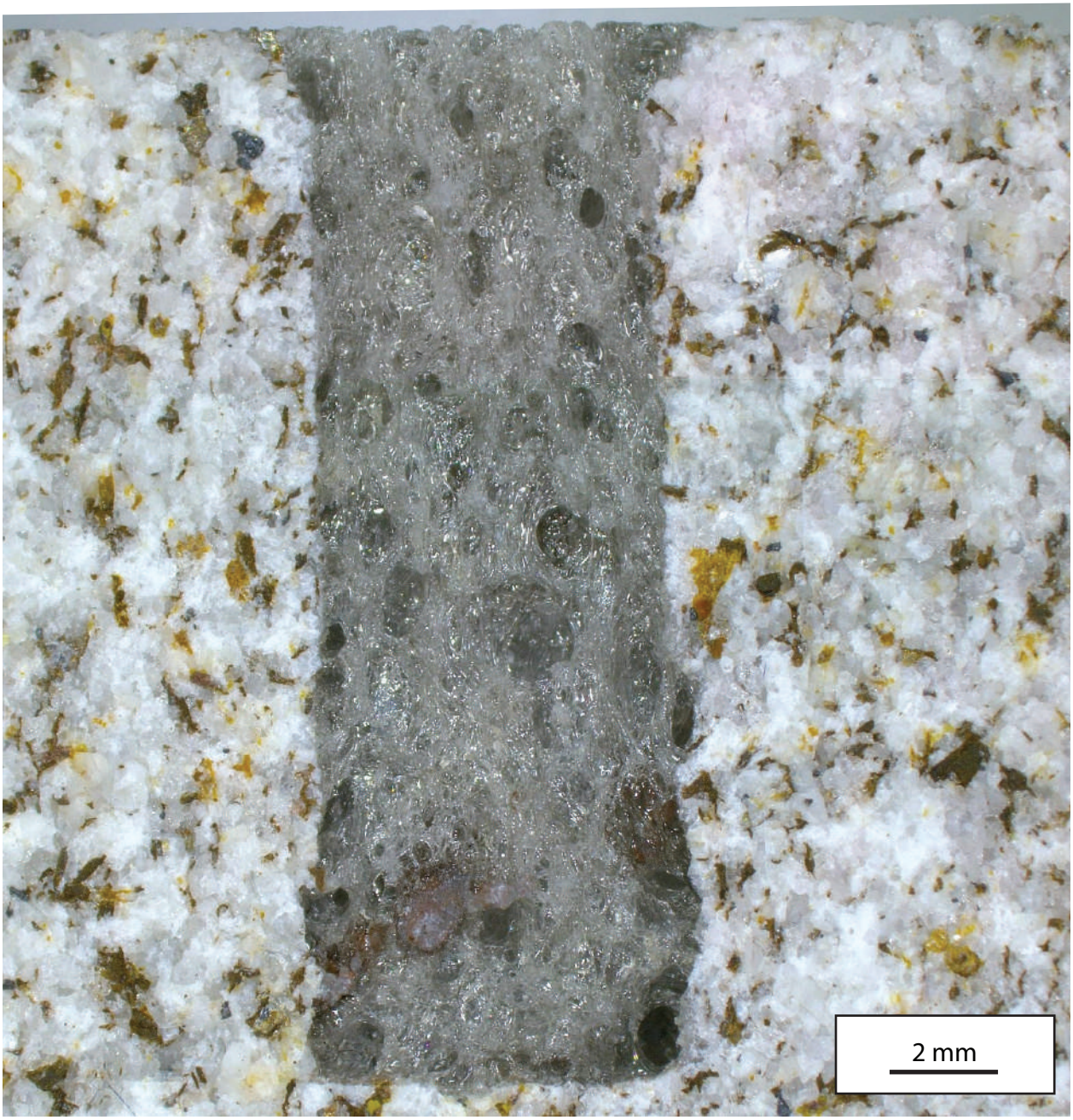

1150 °C RRS-05

Figure 54. Photograph of the top cut of sample RRS-05.

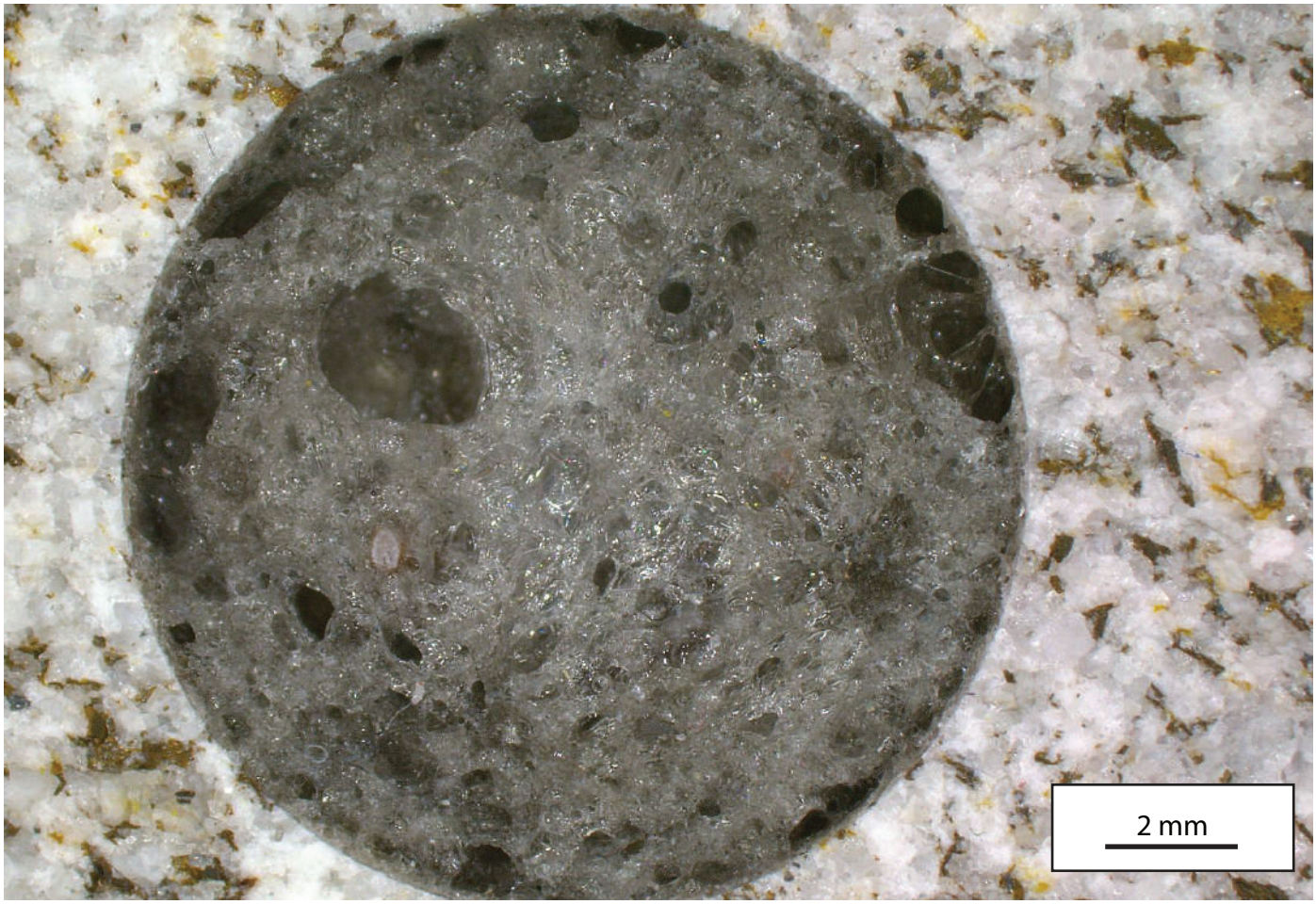

1150 °C RRS-05

Figure 55. Photograph of sample RRG-06 heated without granite jacket.

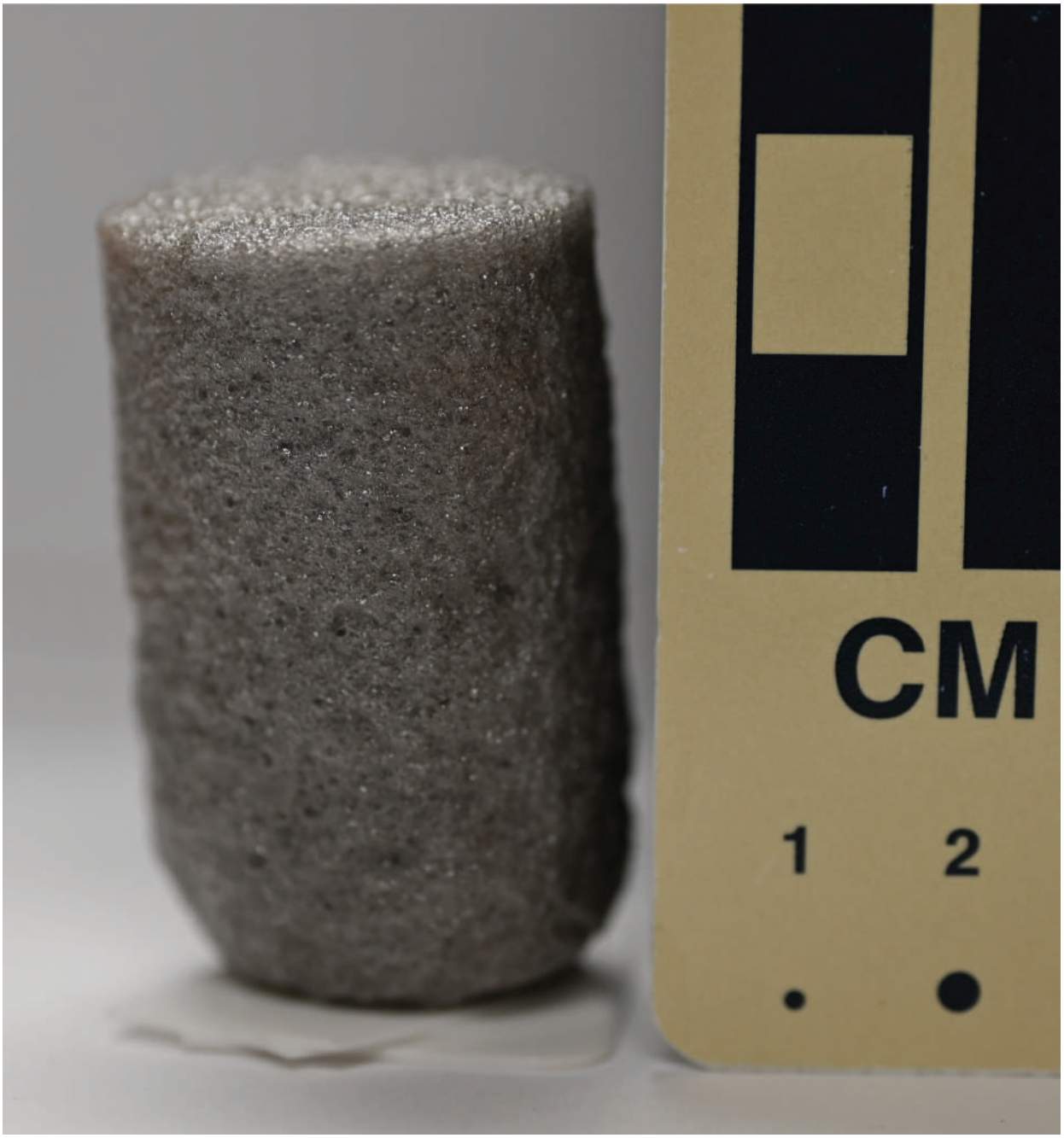

1150 °C RRG-06

Figure 56. Photograph of sample RRS-06 heated without granite jacket.

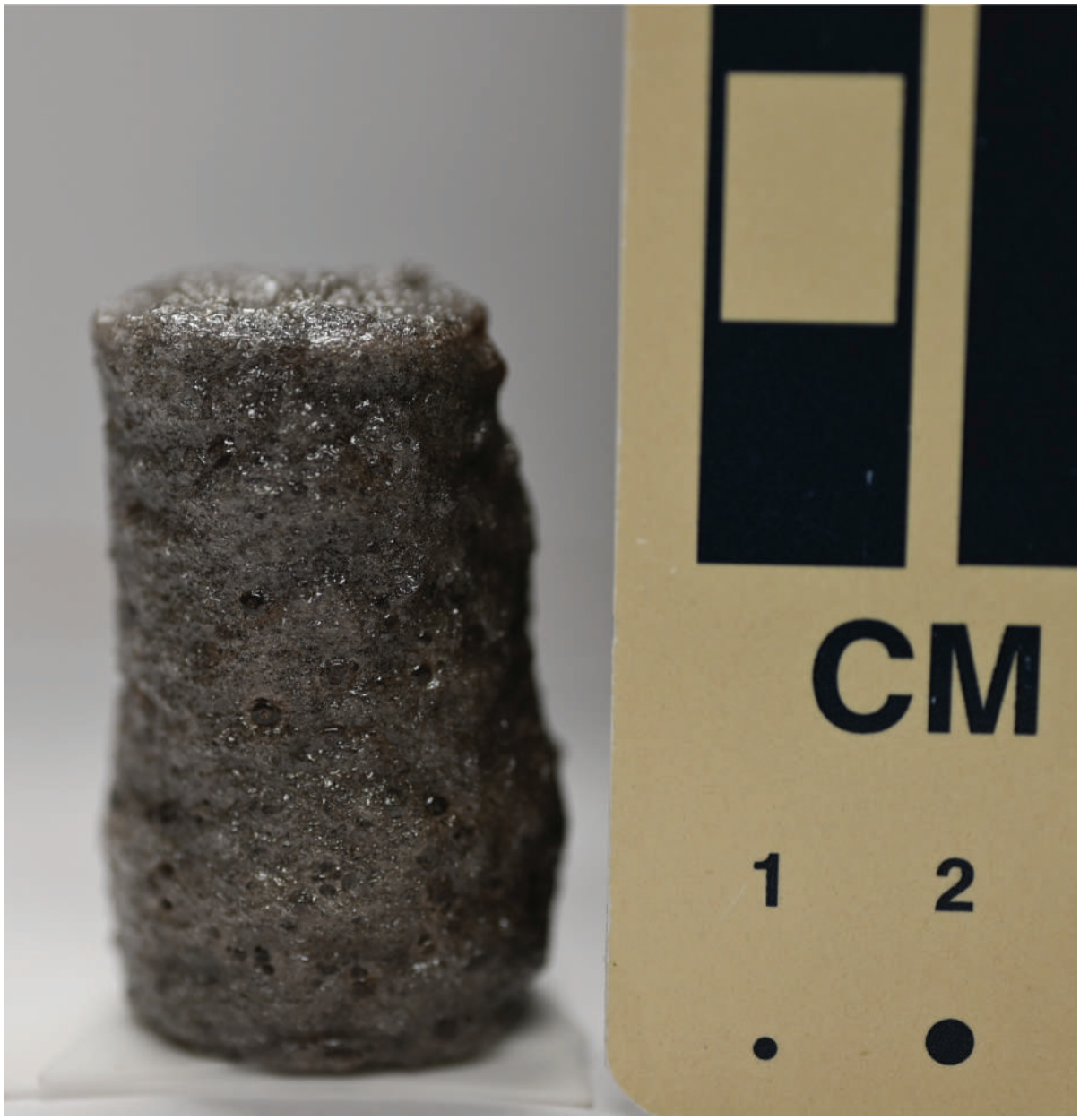
CM
1
2

Figure 57. Schematic of strain profile (indicated with the black solid line) proposed for the foaming obsidian cores in the heating experiments.

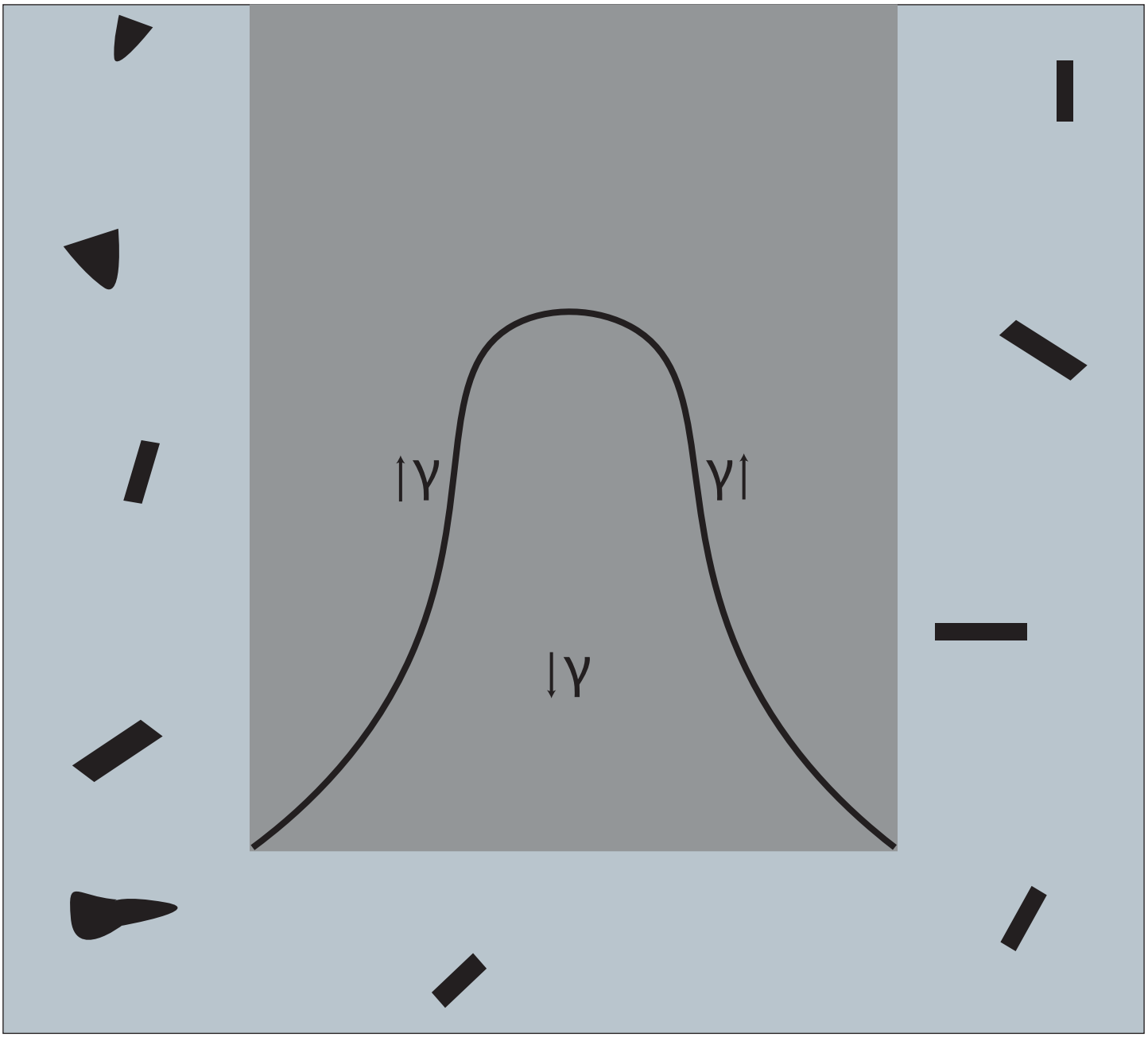
٢↑
٢↑
٢↓

Figure 58. Bubble deformation in a magma flowing in a conduit. Simple shear occurs along conduit margins, and pure shear occurs in the central portion of the magma near the fragmentation zone. Visually represented by blue-to-yellow color gradation (from Ohashi et al., 2021).

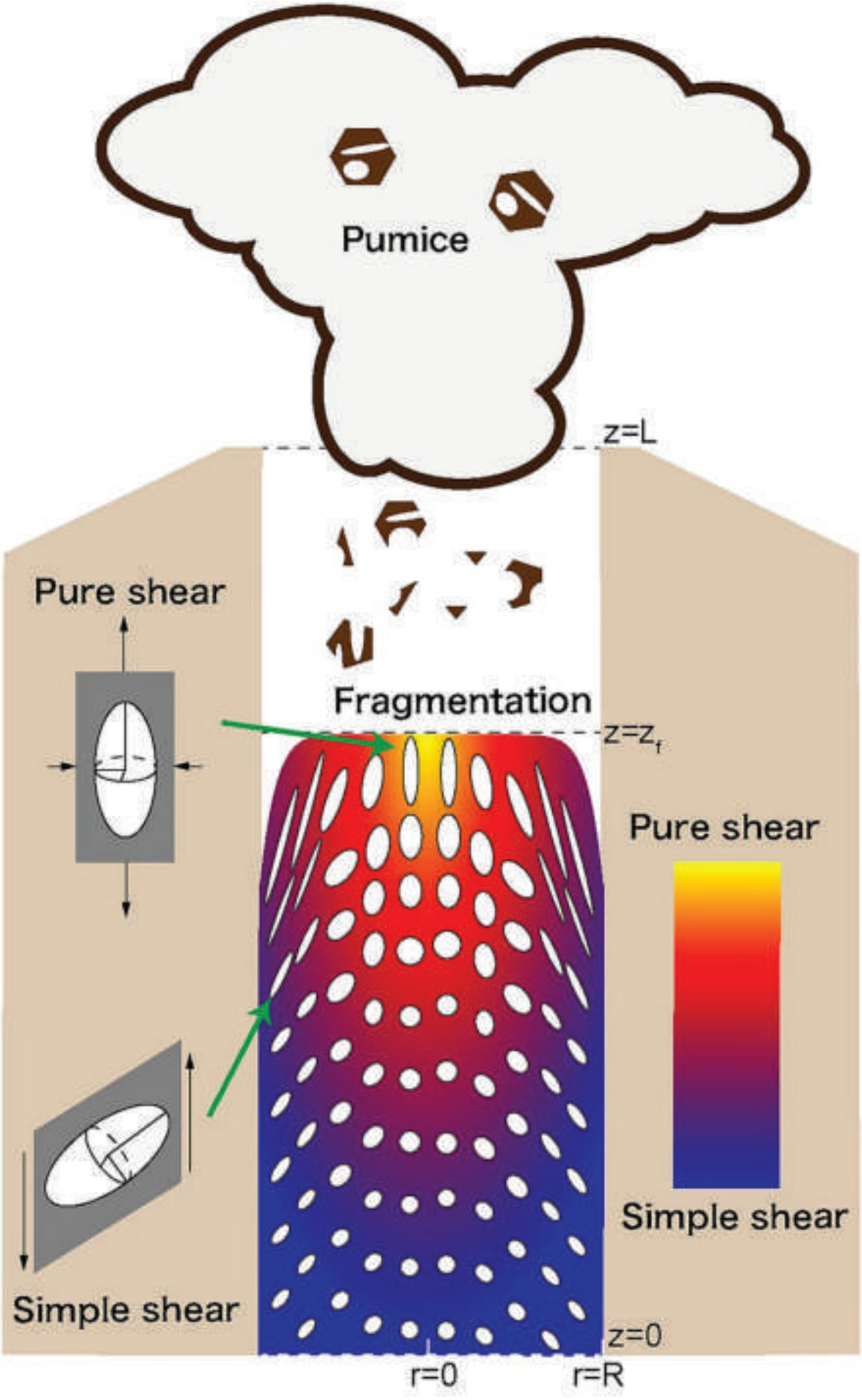
Pumice
z=L
Pure shear
Fragmentation
z=z_f
Pure shear
Simple shear
Simple shear
z=0
r=0
r=R

Figure 59. (a) Velocity flow profiles related to different rheological magma behaviors. (b) Example of extrusion of aloe vera gel representing a parabolic velocity profile. (c) Example of extrusion of toothpaste representing a plug flow velocity profile (from Philpotts and Ague 2022).

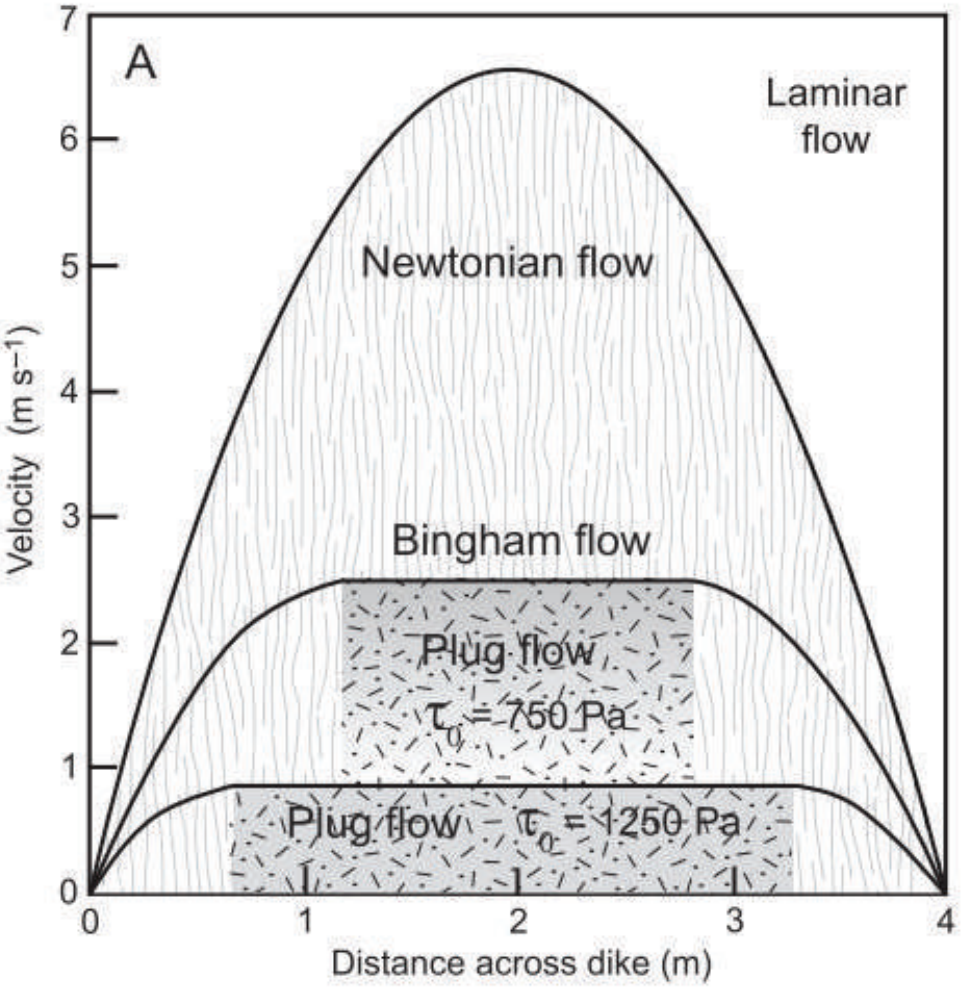
A
Laminar flow
Newtonian flow
Bingham flow
Plug flow
τ_0 = 750 Pa
Plug flow – τ_0 = 1250 Pa
Velocity (m s^{-1})
Distance across dike (m)
0
1
2
3
4
5
6
7

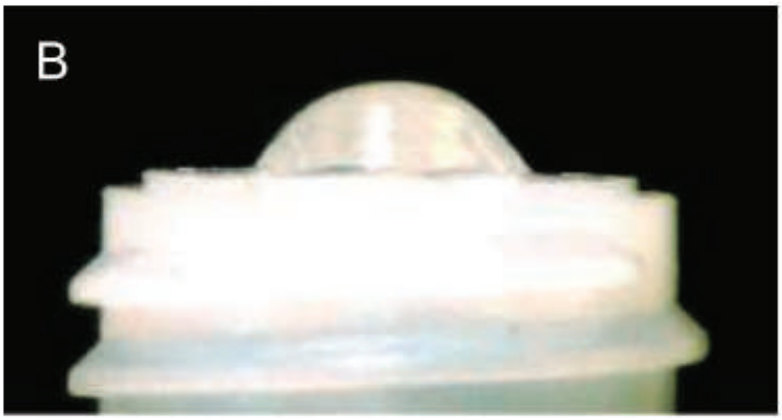
B


C

Figure 60. Extruded portions of foamed glassy run products from heating experiments before sample cutting for analytical investigation. The samples (a) RRG-04, (b) RRG-03, (c) RRG-02, (d) RRG-01, (e) RRG-05, and (f) RRG-06 are displayed from the lowest to the highest temperature.

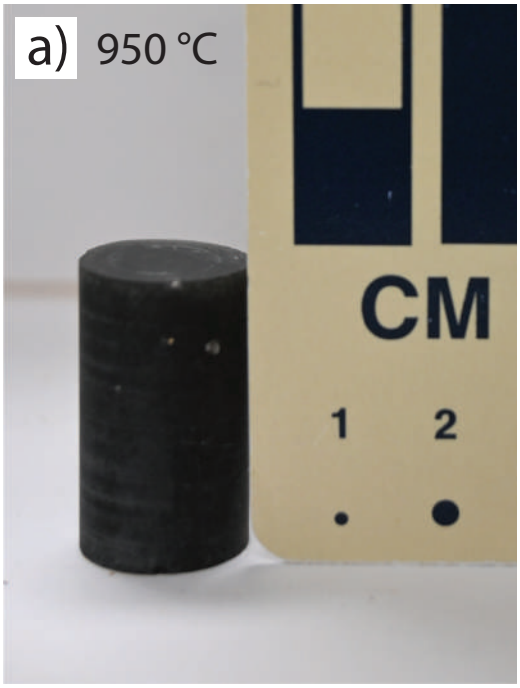
a) 950 °C
CM
1 2

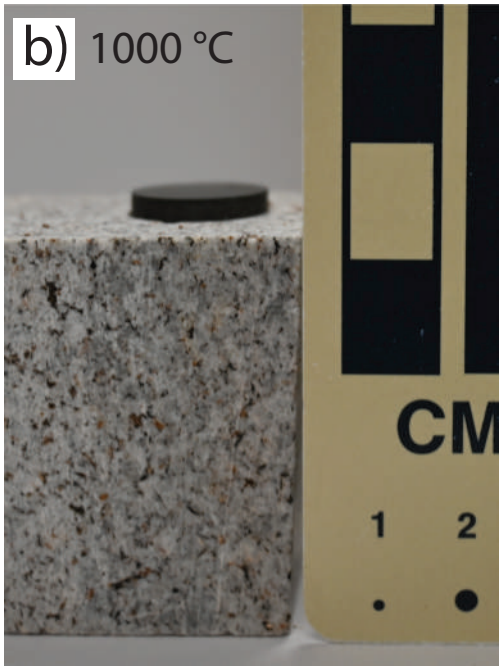
b) 1000 °C
CM
1 2

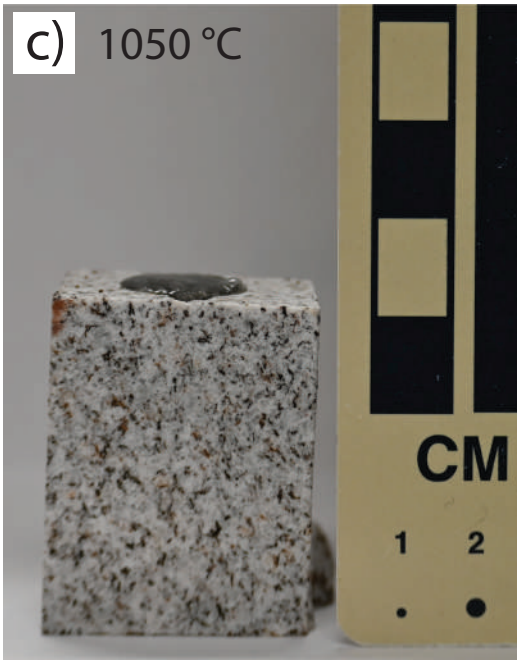
c) 1050 °C
CM
1 2

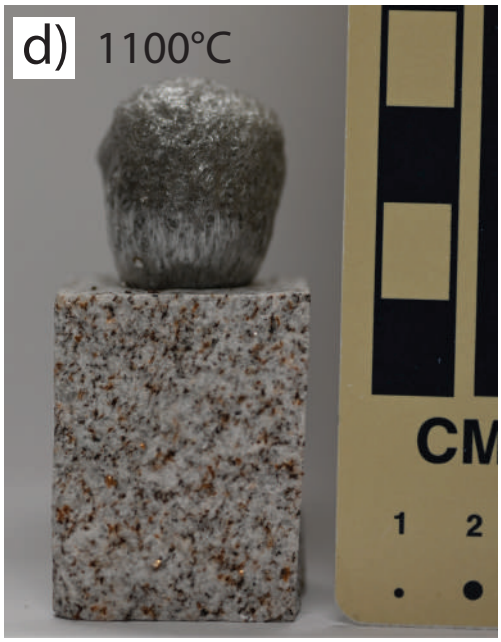
d) 1100°C
CM
1 2

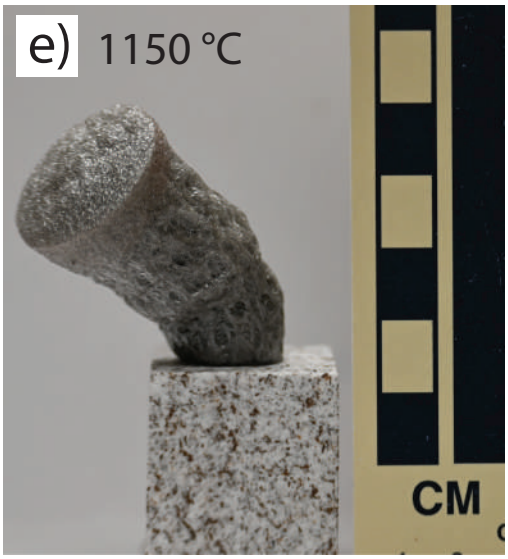
e) 1150 °C
CM

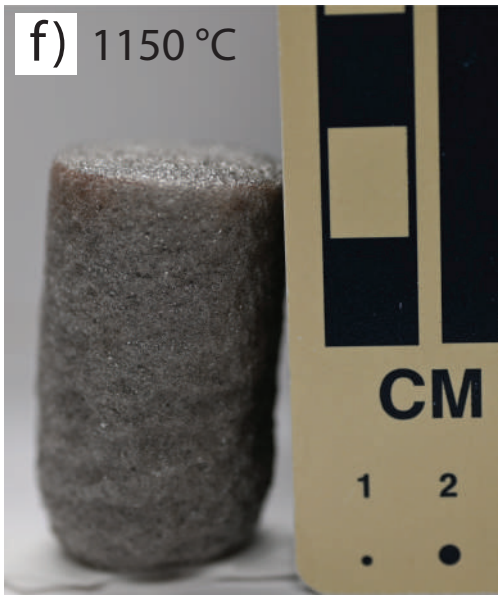
f) 1150 °C
CM
1 2

Figure 61. Extruded portions of foamed spherulite bearing run products from heating experiments before sample cutting for analytical investigation. The samples (a) RRS-04, (b) RRS-03, (c) RRS-02, (d) RRS-01, (e) RRS-05, and (f) RRS-06 are displayed from the lowest to the highest temperature.

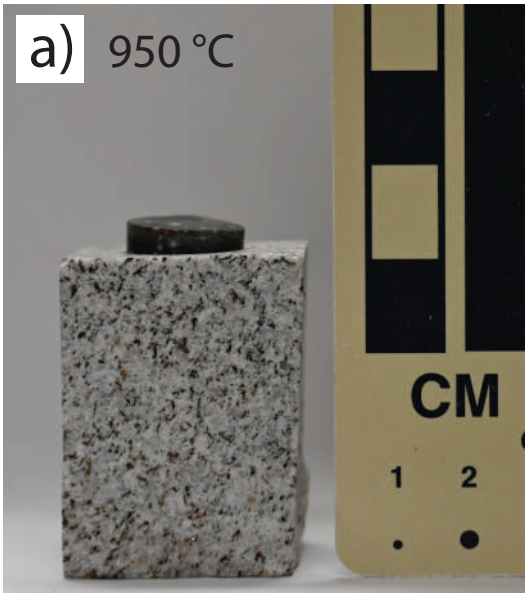
a)
950 °C
CM
1 2

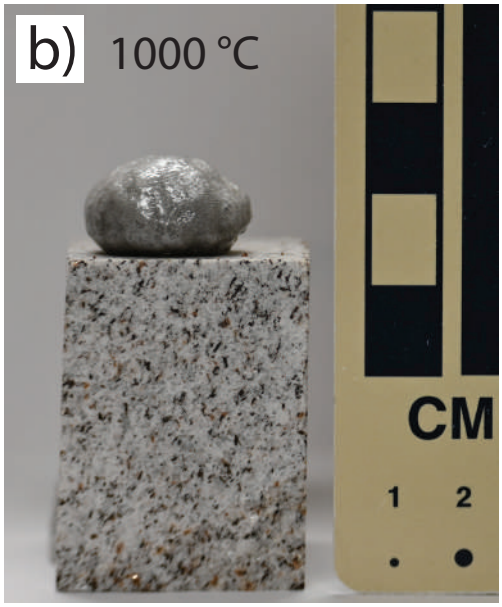
b)
1000 °C
CM
1 2

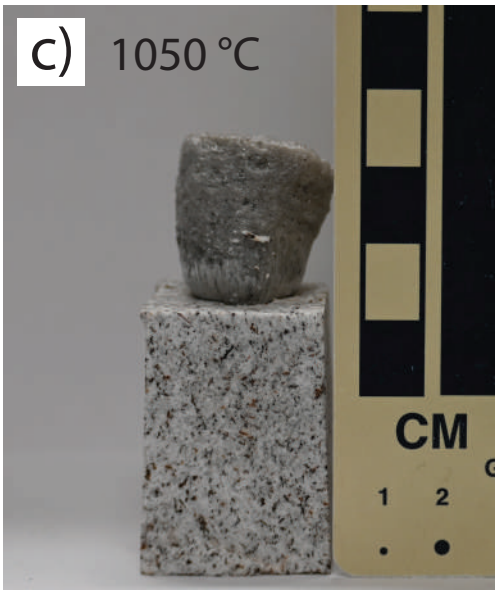
c)
1050 °C
CM
1 2

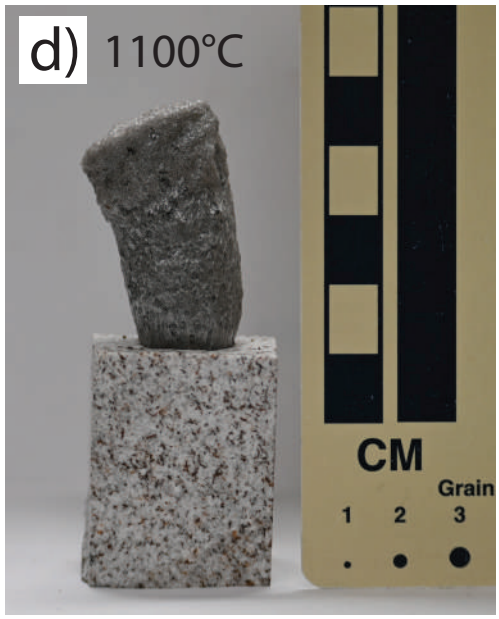
d)
1100°C
CM
Grain
1 2 3


e)
1150 °C
CM
1 2

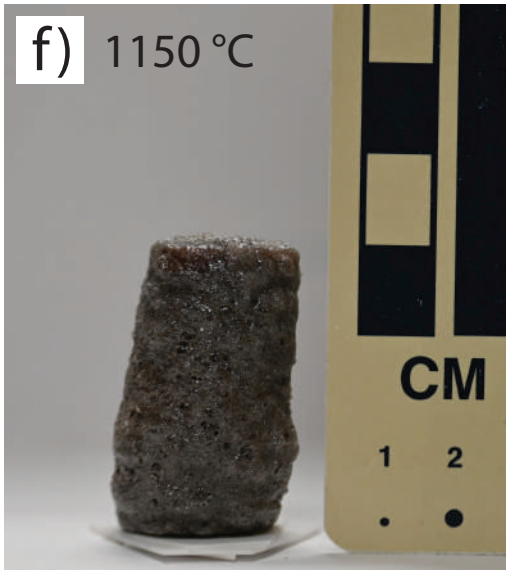
f)
1150 °C
CM
1 2

Figure 62. Obsidian cores and granite jackets inside the MTI Corporation KSL-1200X furnace (University of Texas in San Antonio) before heating. In each photo, glass cores are on the left and spherulite-bearing cores are on the right. The samples here displayed are(a)RRG-04 and RRS-04, (b) RRG-03 and RRS-03, (c) RRG-03 and RRS-02 (d) RRG-01 and RRS-01, (e) RRG-05/06 and RRS-05/06, including the granite core in the center of the photo, and two unconfined samples RRG-06 on the left and on the right.

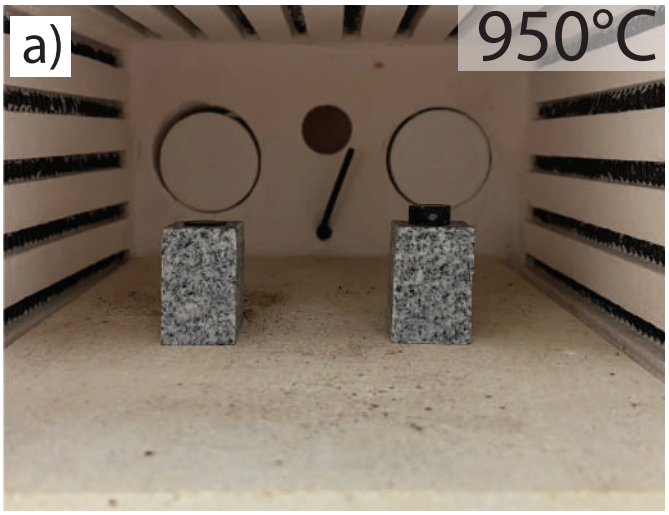
a)
950°C

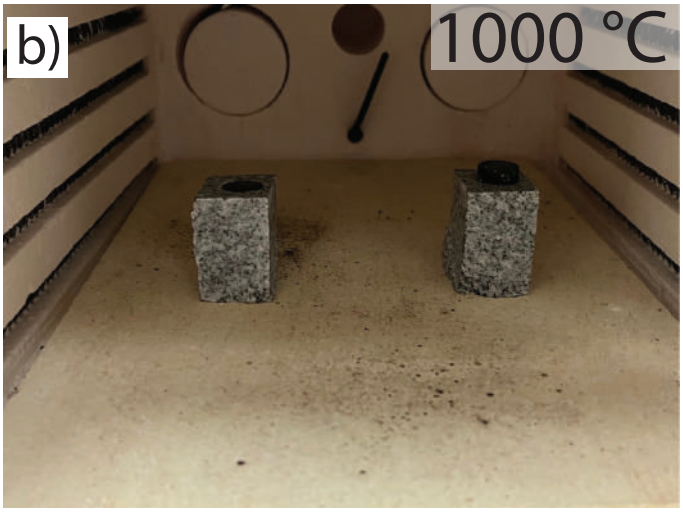
b)
1000 °C

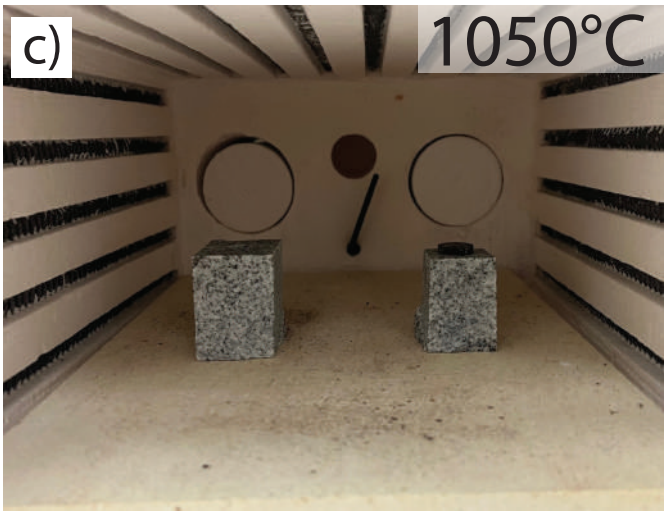
c)
1050°C

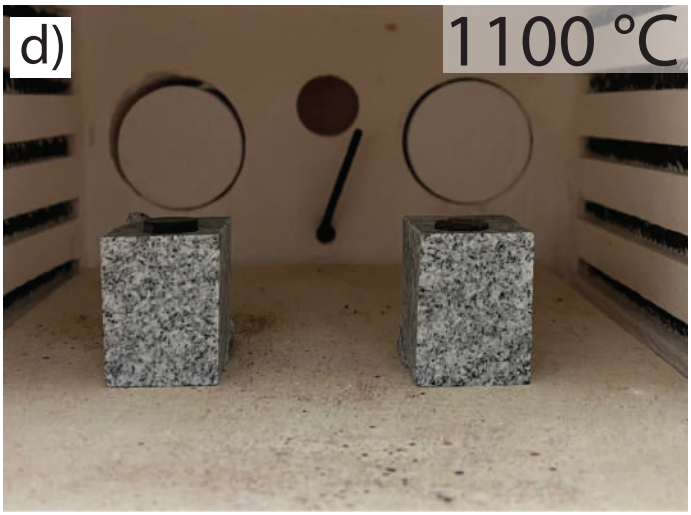
d)
1100 °C

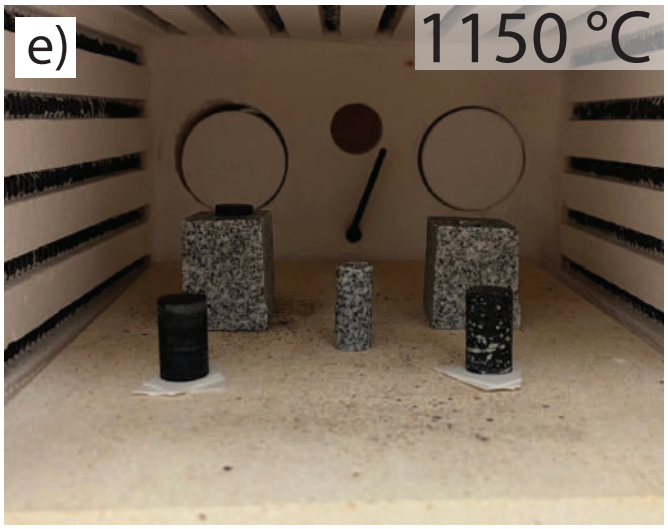
e)
1150 °C

Figure 63. Deborah number (De) as a function of crystallinity and the definition of the viscous to brittle transition (from Pistone et al., 2015). High crystal volume fractions lower De and increase the level of brittle response of a magma at equivalent stress. De required for brittle failure of Lipari Island obsidian is 4.0e-3 (see red star).

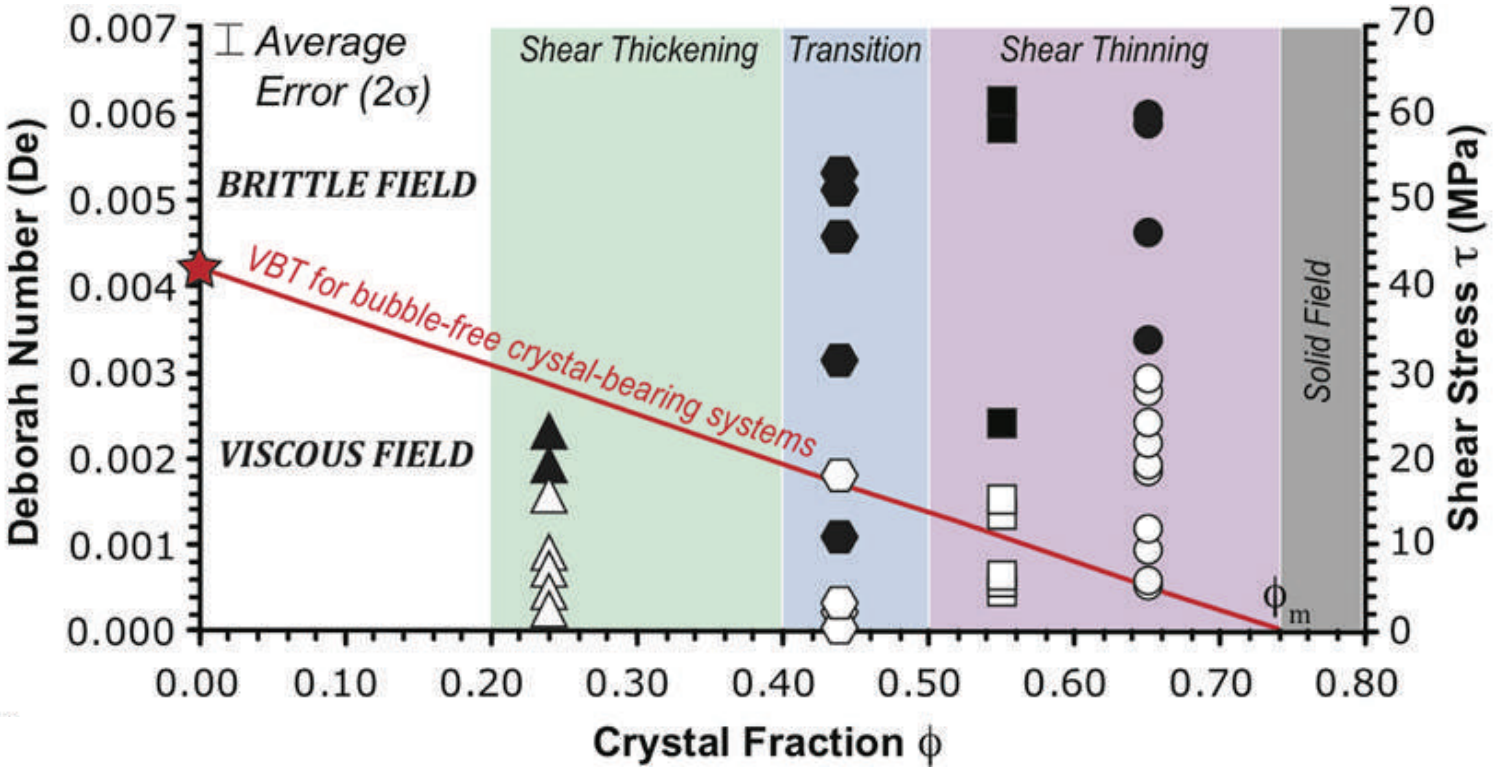
Average Error (2σ)
Shear Thickening
Transition
Shear Thinning
Solid Field
BRITTLE FIELD
VISCOUS FIELD
VBT for bubble-free crystal-bearing systems
ϕ_m
Deborah Number (De)
Shear Stress τ (MPa)
Crystal Fraction ϕ
0.000
0.001
0.002
0.003
0.004
0.005
0.006
0.007
0
10
20
30
40
50
60
70
0.00
0.10
0.20
0.30
0.40
0.50
0.60
0.70
0.80

Figure 64. Viscosity (y-axis) and crystal volume fraction (x-axis) plot from Takeuchi (2011).

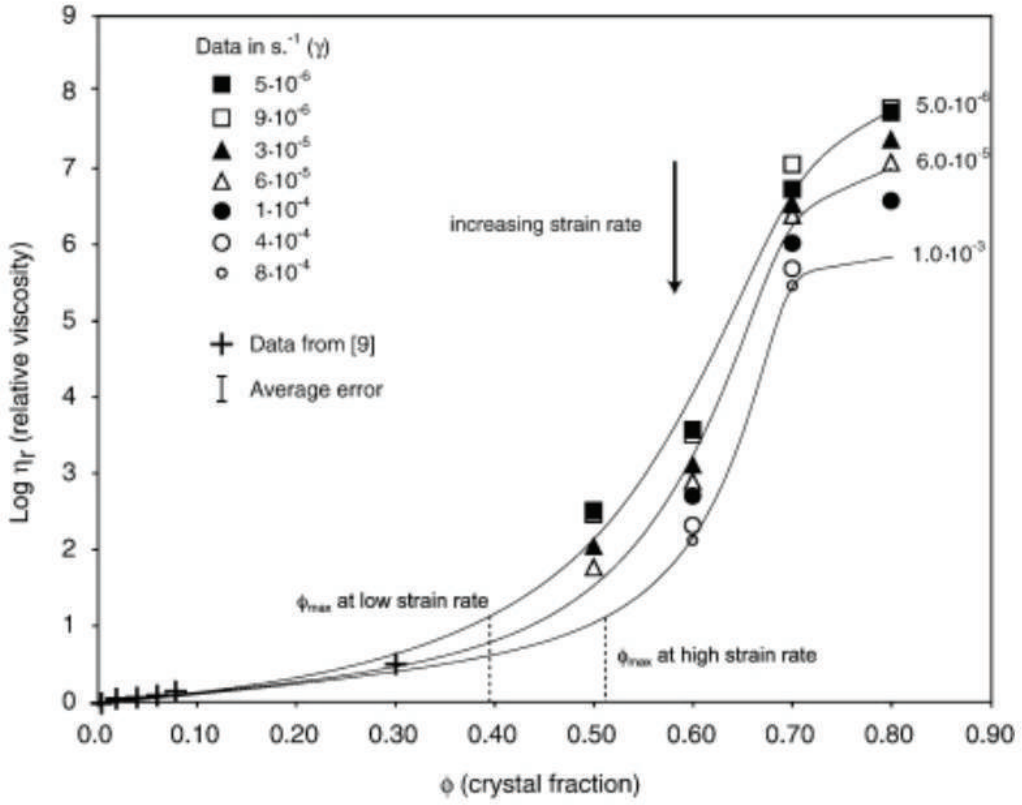
Data in s.-1 (γ)
5·10-6
9·10-6
3·10-5
6·10-5
1·10-4
4·10-4
8·10-4
Data from [9]
Average error
increasing strain rate
5.0·10-6
6.0·10-5
1.0·10-3
ϕmax at low strain rate
ϕmax at high strain rate
Log ηr (relative viscosity)
ϕ (crystal fraction)
0
1
2
3
4
5
6
7
8
9
0.0
0.10
0.20
0.30
0.40
0.50
0.60
0.70
0.80
0.90

Figure 65. ImageJ segmentation of spherulites and microcrystalline silica particles in the obsidian glass. (a) Greyscale image of sample RRS-03 with spherulites highlighted in black. (b) Image separation of spherulites in sample RRS-03. (c) Greyscale image of RRS-02 with spherulites highlighted in black. (d) Image separation of spherulites in sample RRS-02.

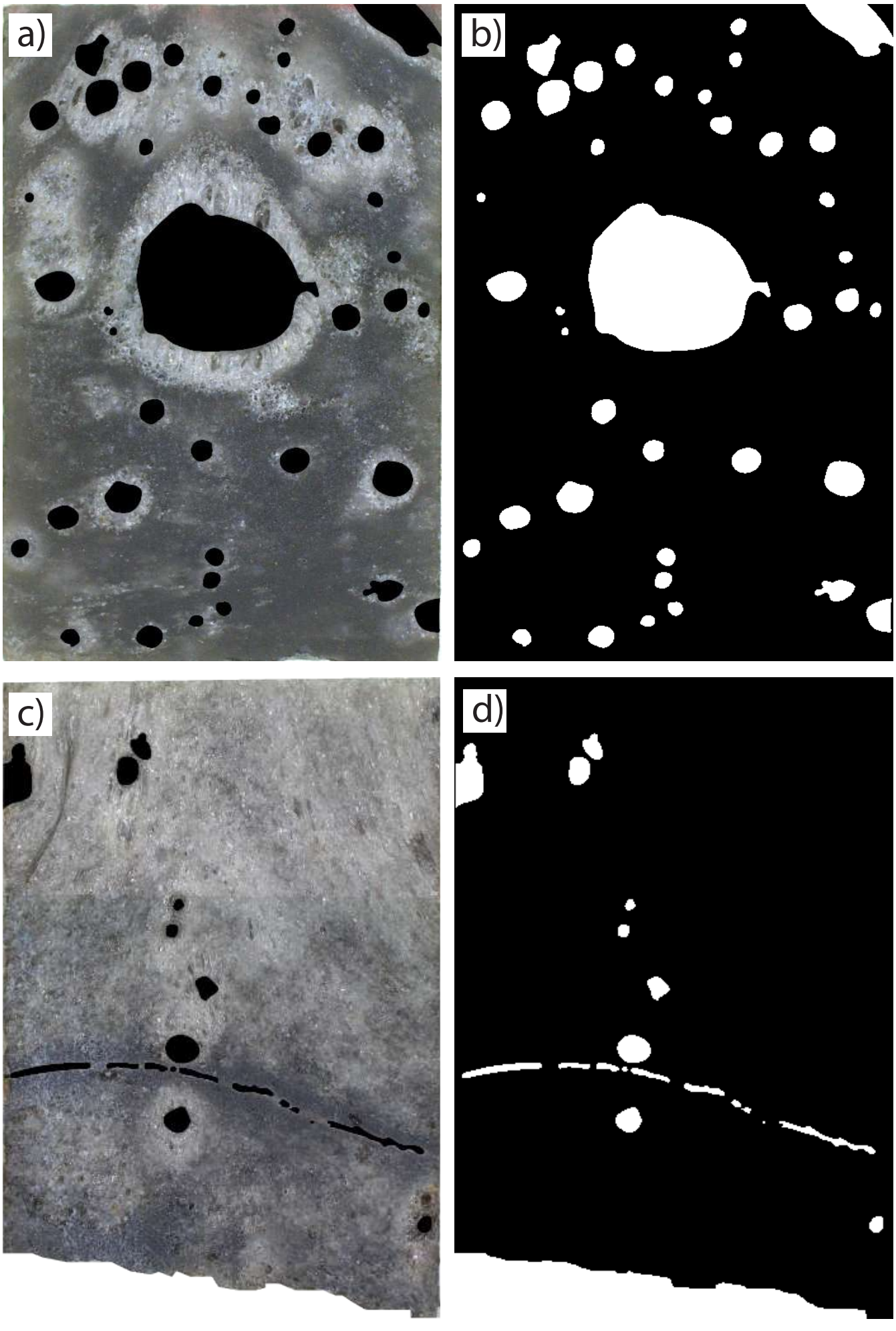
a)
b)
c)
d)

Figure 66. Relationship between H2O concentration in silicic melt (wt.%) and viscosity for different temperatures (K) (from Hess and Dingwell, 1996).

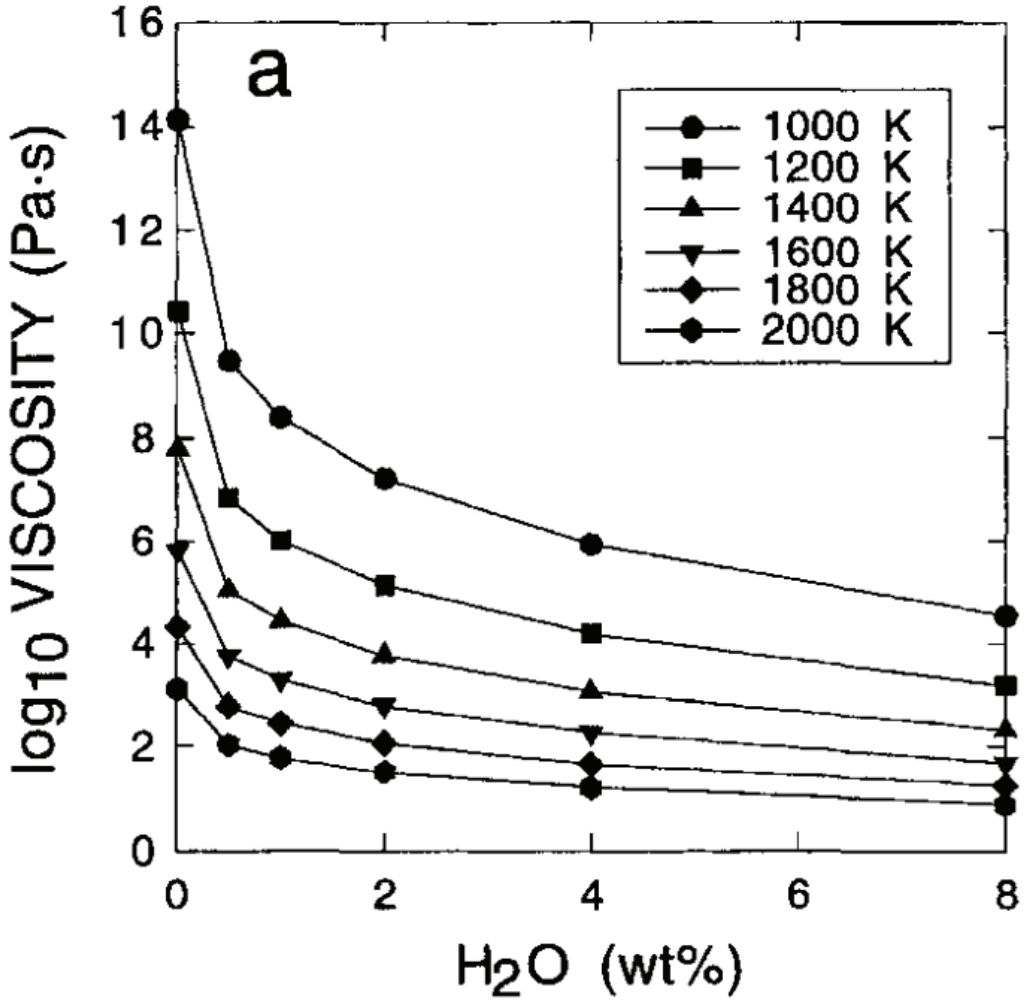
a
1000 K
1200 K
1400 K
1600 K
1800 K
2000 K
log10 VISCOSITY (Pa·s)
H2O (wt%)
0
2
4
6
8
10
12
14
16